RESEARCH ACTIVITIES IN OPTOELECTRONICS AND ELECTRONICS MANUFACTURING 2001

PUBLISHER

VTT Electronics, Kaitoväylä 1, P.O.Box 1100, FIN-90571 OULU, FINLAND
Tel. +358 8 551 2111, Fax +358 8 551 2320
Electronic mail: ele.info@vtt.fi

VTT ELECTRONICS, OULU 2002

PREFACE

VTT Electronics is one of the six operative units of VTT, the Technical Research Centre of Finland, an independent, multi-field contract research organisation. The main task of VTT Electronics is to work as a strategic R&D partner of the electronics industry, thus for its part ensuring the prospected growth in this sector. At VTT Electronics, 72 of its 300 staff members are experts in optics and optoelectronics.

The main goal of Optoelectronics research area is to assist companies in utilizing advanced optical, photonic and optoelectronic technologies in their future products. Our core competence focus is in the advanced technologies and integration methods of optoelectronic modules and instruments. This focus includes challenging research and development aims in modeling, simulation and design, new advanced materials, cost-effective fabrication, manufacturing and packaging applied for multi-technological solutions in optics, optical communication, optical measurements as well as sensors and instrumentation.

In this report, you will find extended abstracts concerning some of the research work carried out in 2001. The abstracts of the examination theses completed by our personnel and a list of publications are also included.

Oulu, February 25, 2002

Harri Kopola
Head of Optoelectronics Research
Harri.Kopola@vtt.fi

Further information: www.vtt.fi/ele

TABLE OF CONTENTS

OPTICAL MODELING AND DESIGN

IPSE - Image Processing Simulation Environment

Janne Aikio, Kari Kataja, Kari Tukkiniemi, Mikko Karppinen, Jukka-Tapani Mäkinen, Veli-Pekka Putila, Kimmo Keränen, Kai Ojala*, Pentti Karioja, Timo Kolehmainen*
(*Nokia Mobile Phones, Oulu, Finland)

We have developed an image processing simulation environment (IPSE) for modeling electronic imaging systems. This environment consists of simulators for an imaging lens and a CMOS (or similar) matrix detector, and image processing and compression modules. In addition, the performance of the lens can be analyzed by using a figure-of-merit known as the subjective quality factor (SQF). The flow chart of the IPSE simulator is shown in Figure 1.

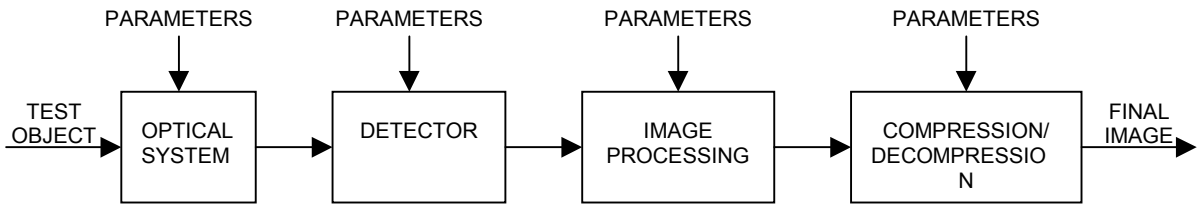

Figure 1. Flow chart for the IPSE simulator environment.

The lens simulator takes very realistically into account the lens aberrations and the diffraction. In the simulator, a Zemax (Focus Software inc.) kernel has been used for ray tracing. SQF is calculated via MTF (modulation transfer function) analysis. The human visual system (HVS) and the detector properties are included in the SQF model. The detector simulation takes (e.g.) the detector responsivity, the properties of the color filter array (CFA), and the noise characteristics into account. The image processing block may contain enhancement for contrast and sharpness, and compensate for distortion. We can, also analyze the effects of image compression, for example JPEG. A simulated example is shown in Figure 2.

Figure 2. Simulation example. a - original image, b - image shown through a lens; values of the subjective quality factor are shown as contours on top of the image, c - image shown through a lens and detected with a CMOS detector.

Backlight illumination

Jukka-Tapani Mäkinen, Pasi Vahimaa*, Ilkka Kallioniemi*
(*Heptagon Oy)

INTRODUCTION

A project funded by Polar Electro, Suunto and TEKES ended in the summer of 2001. The two active parties involved were Heptagon, which acted as the project co-ordinator, and VTT Electronics, which had a role as a sub-contractor. The purpose of the project was to design an LCD backlighting prototype that would distribute the light emitted by LEDs evenly over the display area.

SPECIFICATIONS

The target was that the LEDs should provide an even illumination for the LCD with a brightness comparable to an EL-backlight element. Naturally, the light-guiding component should also have to be mass-producible. Furthermore, the application itself placed some size restrictionson the optical components.

OPTICAL DESIGN

Work was started by compiling a properties list of commercially available surface mountable LEDs. Two different components with similar size and light distribution characteristics were chosen as possible sources. The first was an older generation AlInGaP LED and the second a considerably brighter InGaN type LED.

In the next phase, the in-coupling structures of the light-guide were optimized. The optimization was performed at VTT with ASAP (Advanced Systems Analysis Program), which is a very efficient optical simulation program that uses the Monte Carlo ray tracing method. In this case, the far-field distribution of the LED, usually given in the component's data-sheet, was not enough. The in-coupling structure is located very close to the source and therefore also the near-field behavior needed to be considered in the simulations. This was achieved by building the whole mechanical structure of the LED (e.g. semiconductor chip, bonding pad & wire, epoxy shell) in ASAP. The accurate LED model was verified by measuring the component's far-field irradiance distribution and comparing it to the simulated results. Simulations showed that the optimized in-coupling structure (see Figure 1) was able to couple 50 % of the light emitted by the LED into the thin light-guide plate when the sides of the structure had reflective coatings. With bare polished surfaces only 32 % of the light was propagated into the light-guide.

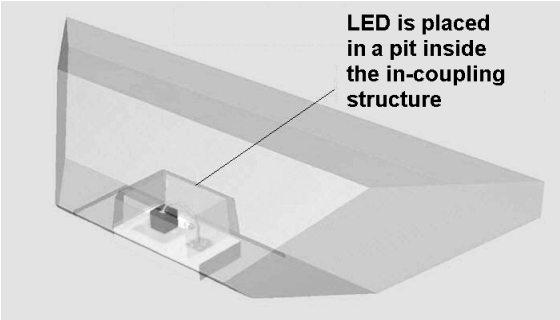

Figure 1. Designed in-coupling structure

The out-coupling structure of the light-guide was designed by Heptagon. The structure consisted of several thousand miniature-sized scattering features that were placed at the bottom of the light-guide. The geometrical form of the small scattering object was optimized analytically to provide the best out-coupling light distribution. The size and shape of the features remained the same throughout the light-guide. Even backlight distribution was achieved, by placing the scatterers in a specific pattern. The pattern was optimized iteratively by using analytical methods to make the designs (Heptagon) and verifying these with ASAP simulations (VTT). The simulated light distribution of the LED & in-coupling structure combination was used as a starting data in the pattern calculations.

OPTOMECHANICAL DESIGN

The optomechanics of the light-guide was designed in such a way that the in-coupling structures and the out-coupling light-guide could be manufactured in a single piece by injection molding. The backlight element was designed to fit into the plastic frame that holds the display (see Figure 2). This whole module can be placed directly on top of the PCB where the surface mountable LEDs are positioned.

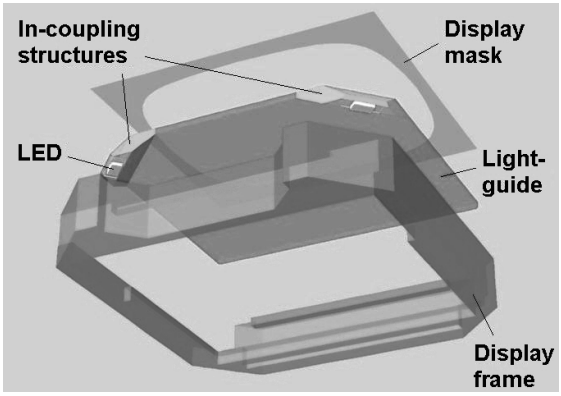

Figure 2. Placement of the light-guide.

PROTOTYPE MANUFACTURING

The light-guide prototype (see Figure 3) was manufactured as two separate parts. The in-coupling structures were machined from acrylic with a 5-axis machine tool, polished and partly coated with a thin aluminium layer at VTT Electronics Oulu. The light-guide with the out-coupling pattern was manufactured at Heptagon's facilities in Zurich. In this process, a thin glass substrate was coated with a layer of plastic material. The original out-coupling pattern was first made on the plastic layer with a direct laser beam writer and then replicated with UV casting. One functional prototype was formed when two incoupling structures were glued to the corner facets of the light-guide plate.

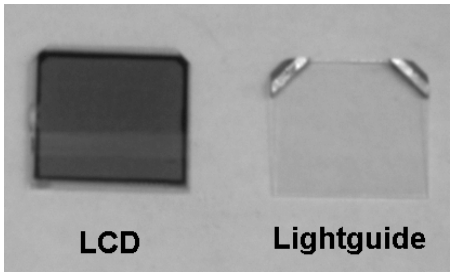

Figure 3. The light-guide prototype.

CHARACTERIZATION

Characterization of the prototype was performed with a laboratory set-up, in which the two LEDs were attached to xyz-translation stages in order to be able to study the positioning tolerances of the components. The light-guide was placed between a thin white diffuser surface and the LCD, which also had a diffusing semi-transparent surface at the bottom. An opaque mask was placed on top of the LCD to block out the edges, which are usually hidden by the cover of the application. The simulated (ASAP) and measured light distributions of the prototype are shown in Figure 4. The brightness of the prototype backlight exceeded that of the EL backlight.

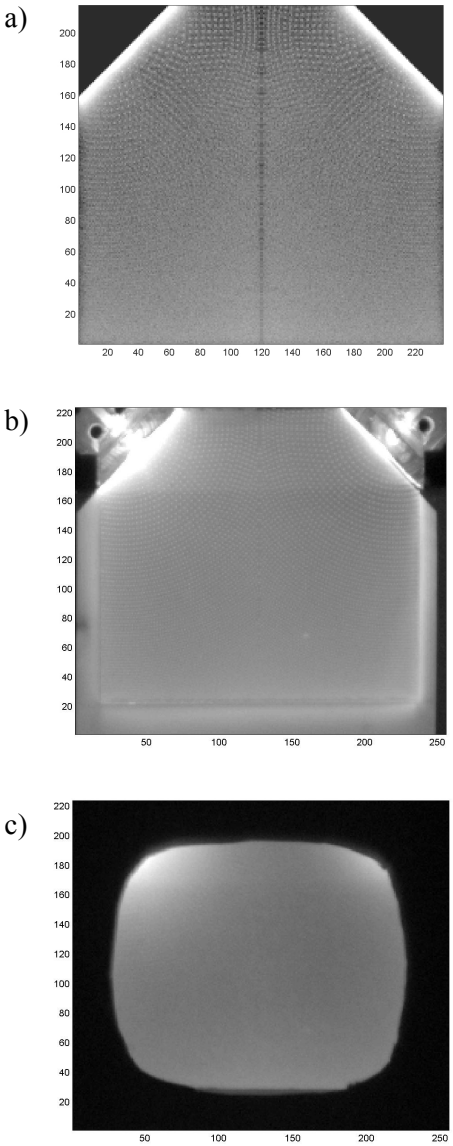

Figure 4. a) Simulated and b) measured light distribution of the prototype light-guide without the display. c) Distribution of light with the display and mask.

Numerical study of near field writing on a Phase Change optical disc

Kari Kataja, Janne Aikio and Dennis G. Howe*
*University of Arizona, Optical Sciences Center, 1630 E. University Blvd, Tucson, Arizona 85721, USA

INTRODUCTION

In this work we study phase change (PC) optical disc structures suitable for near field recording[1] arrangements that we call *direct semiconductor laser read/write* systems. In this system a laser diode, is brought very close to the optical disc's data surface (an airgap between laser diode and the recording structure is less than laser's wavelength). The airgap and thin layers of the optical disc forms an extremely short external cavity (ESEC) at the front facet of the semiconductor laser. In the external cavity, part of the light emitted by the laser is reflected from the disc and coupled back into the laser cavity. This coupled light forms an *optical feedback* loop that affects the laser's operating wavelength, optical output power and forward bias voltage. These laser properties further affects the magnitude and spatial distribution of light absorbed by the disc's PC layer. The main goal of this work is to determine how the optical design of the disc structure (as well as the thickness of the airgap) influences the absorption of light in the PC layer.

We have earlier developed a tool to simulate ESEC laser diodes[2]. This tool comprises of a phenomenological laser model that utilizes the *effective reflectance* concept to take into account the influence of the ESEC. The details of the optical field within the ESEC structures have been calculated by using Finite Difference Time Domain (FDTD)[3,4] simulations. The modeling is done in three steps. First, in the FDTD simulation a normalized beam is launched from the laser into the ESEC to predict the proportional absorption in the PC layer and the effective reflectance of the ESEC. Second, the effective reflectance data is inserted into the phenomenological ESEC laser model to predict the operating wavelength and optical output power of the laser. Third, the absolute absorption rate in the PC layer is calculated by scaling the proportional (normalized) absorption to correspond with the laser's calculated output power.

SIMULATION MODEL

In the 2-dimensional FDTD simulations, the laser was modeled as a bulk 3-layer structure. The optical disc was modeled as a stack of thin layers. A narrow airgap was left between the laser's front facet and the optical disc.
The energy flow (Poynting-Vector) is calculated from electric and magnetic field values. Energy flow is used to calculate absorption in the various layers of the system. The total absorption in the PC layer is obtained by integrating over the area occupied by that layer.
In order to calculate the effective reflectance (i.e., the complex amplitude of light coupled from the ESEC back into the laser waveguide), we developed a method to extract the reflectance information from the FDTD analyses. Once the effective reflectance is obtained, the phenomenological laser model is used to predict laser performance under ESEC feedback[2,5].

NUMERICAL RESULTS

We have studied the effect of the few parameters to the spatial absorption profile and the total absorption in the PC layer. Here we show as an example the variation of the airgap, which was changed between 40…500 nm and the cover layer, which was scanned between 40…200 nm. In Fig. 1 we show the transverse absorption profile in the PC layer as a function of the airgap thickness. There are two interesting features in the profile behavior. First, there is an absorption maximum at airgap thickness of 80 nm. Second, the spatial absorption profile becomes wider when the airgap thickness is increased. The latter effect is most likely due to diffraction of the laser beam. The former effect is related both to the change in the laser output power (even though the laser drive current is held constant) and the resonance effects in the external cavity structures.

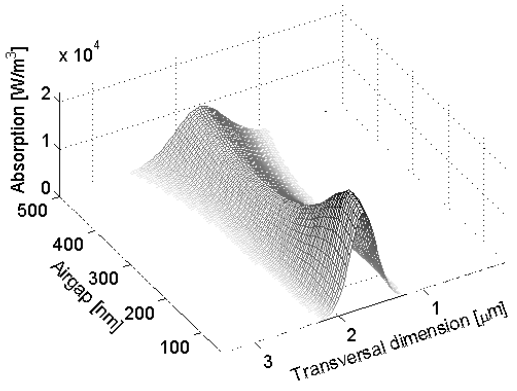

Figure 1. Transversal absorption profile in the phase change layer as a function of airgap thickness.

Fig. 2 shows the total power, total absorption, output power from the back facet and scattered power in the ESEC when the airgap thickness is scanned. Total power $P_{Total} = P_1 + P_2$, where P_1 is output power from the back facet of the laser and P_2 is output power from the front facet of the laser. It should be noted that P_2 is that power which is launched into the ESEC structure and that (because of the metallic mirror) there is no power radiating through the substrate.

When the cover layer, PC layer and insulating layer thicknesses are 100, 20 and 20 nm respectively, the total absorption in the PC layer has a maximum when the airgap is 80 nm. This same effect is also seen in Fig. 1 as mentioned above. The total absorption also follows the total laser power curve.

Because of this variation in the absorbed power as a function of airgap thickness, the laser diode should be kept at the constant distance from optical

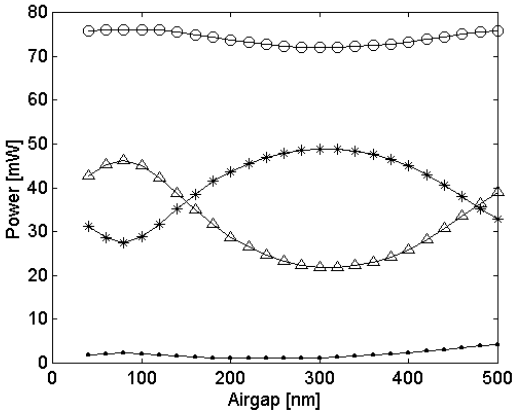

Figure 2. Total laser output power '—○—', total absorption in the PC layer '—△—', output power from the back facet '—✳—' and scattered power in the ESEC '—●—' as a function of the airgap thickness.

disc while writing. Otherwise written mark size might vary, because of the variations in heated spot size and absorbed energy. In addition, power emitted from the back facet of the laser varies and so airgap thickness will affect to the read signal as well, as reported earlier[1,8].

In the second case, the cover layer thickness is varied, as the other parameters are kept constant. In Fig. 3 we show total power, total absorption, output power from the back facet and scattered power in ESEC versus cover layer thickness. At first it seems that cover layer thickness has a similar effect on the absorption as the airgap thickness. The total absorption

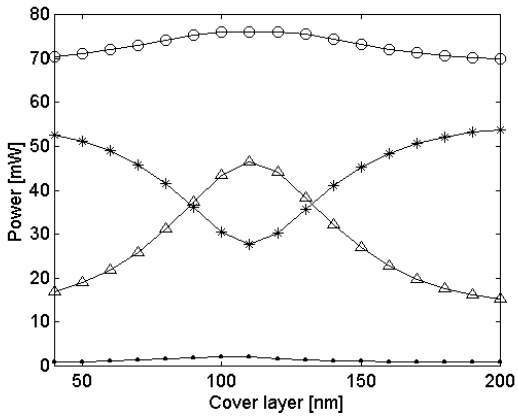

Figure 3. Total laser output power '—○—', total absorption in the PC layer '—△—', output power from the back facet '—✳—' and scattered power in the ESEC '—●—' as a function of the cover layer thickness.

curve in Fig. 3 exhibits a maximum, which is useful when the writing operation is considered. It may be useful to study the influence of the refractive index of the cover layer (and insulating layer), but currently we have restricted our simulations to those materials used in conventional PC disc structures.

DISCUSSION AND CONCLUSION

The influence of the structure of a PC disc on the absorption of light in the PC layer was studied using two dimensional simulations of a direct semiconductor laser write/read system. Mark formation was not modeled; we assumed that the writing performance is related to the absorbed optical power density in the phase change layer. In this work the laser and material parameters were fixed - only the geometry of the recording structure of the disc and the thickness of the airgap was varied. The study indicates that the disc structure does indeed affect the

power density of light absorbed in the PC layer. In addition, it may be even possible to adaptively optimize the ESEC structure for writing or erasing during the operation by altering the thickness of the airgap by, for example, changing the fly height of the laser diode above the disc's data surface. On the other hand the airgap thickness should be kept fairly constant in order to minimize fluctuations in absorbed power when writing and reading data marks.

The influence of several parameters have not been studied all, e.g., the laser wavelength, and the index of the constituent disc recording structure materials. Further, the overall design of the recording structure itself has not been altered from that used in conventional PC discs that are meant to be recorded and read through the disc substrate by a laser that is optically isolated from the disc. It should also be remembered that simulations were performed in steady state, no dynamic effects (pulsed laser, change in the PC layer material properties due to heating) were studied and that the effective reflectance approach does not even apply in that case. Finally, it should be mentioned that three dimensional simulations are required to fully model the real systems.

REFERENCES

1. H. Ukita, Y. Katagiri and S. Fujimoro, Appl. Opt. **28**, 4360-4365 (1989).
2. J. Aikio and D. Howe, Proc. SPIE **4090**, 56-65 (2000).
3. Taflove and S.C. Hagness, *Computational Electrodynamics: The Finite-Difference Time-Domain Method* (Artech House, Boston, 2000).
4. J.B. Judkins, C.W. Haggans and R.W. Ziolkowski, Appl. Opt. **35**, 2477-2487 (1996).
5. L.A. Coldren and S.W. Corzine, *Diode Lasers and Photonic Integrated Circuits* (John Wiley & Sons, New York, 1995).
6. M. Levinshtein, S. Rumyantsev and M. Shur, *Handbook Series on Semiconductor Parameters Volume2: Ternary and Quaternary A_3B_5 Semiconductors* (World Scientific, Singapore, 1999).
7. M. Okoniewski, M. Mrozowski and M.A. Stuchly, IEEE Microwave and Guided Wave Lett. **7**, 121-123 (1997).
8. J.-Y. Kim and H.C. Hsieh, J. Lightwave Tech. **10**, 439-447 (1992).

OPTICAL AND OPTOELECTRONIC MATERIALS AND COMPONENTS

Hybrid glasses for micro-optics applications

Ari H. O. Kärkkäinen, Juha T. Rantala[a] and Michael R. Descour[b]
[a]GuideOptics Oy, P.O. Box 114, FIN-90570 Finland
[b]Optical Sciences Center, The University of Arizona, Tucson, AZ 85721 USA

INTRODUCTION

Various application fields such as telecommunications, data storage, information displays, sensing and imaging systems are moving towards integrated electronic and photonic systems. This trend has created growing demands for miniaturization of conventional optical systems as well as for development of novel materials and manufacturing technologies to fabricate and integrate micro-optical systems as part of electronic devices. Several processing and manufacturing techniques as well as material categories have been introduced for micro-optics fabrication. Conventionally, the fabrication of micro-optical structures is performed by a multi-step process. This process includes patterning of a deposited photoresist film using "mask lithography" (UV or X-ray) or "scanning lithography" (electron-beam or laser-beam scanning).[1] In "mask lithography", binary and/or grayscale photomasks are used to produce the desired images in photoresist films. Reflow techniques can be applied to further modify the shape of the photoresist structures. The resulting patterned resist surfaces can be then etched directly into the underlying substrate by using wet or dry etch transfer or used to produce tools suitable for replication.[1-3] The LIGA and diamond-turning techniques have also been applied in replication tool fabrication.[4-6] More recently, non-lithographic techniques such as ink-jet printing of optical structures using polymers and sol-gel derived materials have been investigated.[7-9]

Our approach to fabrication of micro-optical and opto-mechanical structures is based on the hybrid sol-gel method.[10,11] Two different methods are introduced. The first one is referred as photolithographic patterning and the other as photolithographic deforming of hybrid glass materials. When using photolithographic patterning of hybrid glasses no etching transfer of patterned hybrid glass structures is required. The elimination of the etching transfer step potentially improves the surface quality of the finished micro-optical elements and speeds up the fabrication process even when very thick structures are fabricated. We have recently demonstrated the fabrication of optical structures by applying photolithographic deforming of hybrid glasses.[12] In this method even the structure development step can be excluded from the fabrication and high quality optical surfaces can be obtained.

Photolithographic patterning of lenslet arrays with lens sags up to 100 microns and opto-mechanical structures with thickness up to 118 microns is demonstrated, using negative tone hybrid glass materials and grayscale and binary photomasks. Direct photolithographic deforming of hybrid glasses is applied in fabrication of lenslets, lens arrays and sinusoidal gratings[12]. Deformation heights up to 24 microns are demonstrated by applying mercury UV-lamp and UV-laser exposure of hybrid glass films.

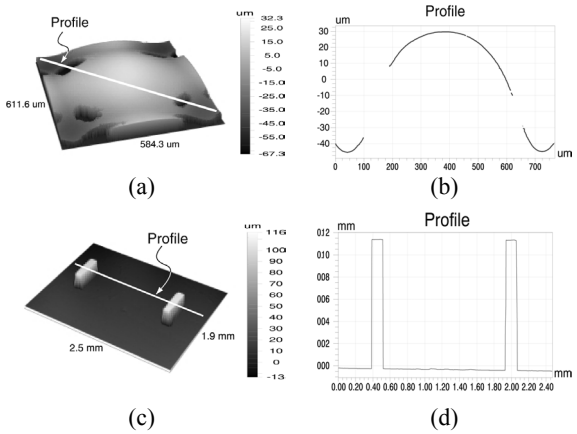

Figure 1. Part (a) shows a segment of a lenslet array patterned lithographically in hybrid glass using a grayscale photomask. Each lenslet aperture is a square measuring 480 μm on a side. Part (b) shows a diagonal profile of the surface. Lens sag was measured to be 75 μm. Missing data occur due to regions of high slope on the patterned surface. Parts (c) shows lithographically patterned opto-mechanical features in hybrid glass using a binary photomask to an average height of 118 μm. Part (d) shows height data along the profile indicated in Part (c). Images taken with NT3300 optical profiler, courtesy Veeco Metrology Group.

EXPERIMENTAL

The hybrid glass materials used in the both fabrication methods contain an inorganic base matrix, which is prepared by hydrolysis and condensation of alkoxysilanes. The inorganic base matrix is provided with side chains containing terminal carbon double bonds that provide the material with photopolymerizability. In addition, acrylate monomers can be added to the material to increase the crosslinking density of the prepolymer solution. The viscosity of the prepolymer solution should be high to result in structures with of large thicknesses. Also the material adhesion to the substrate has to be high. The liquid phase deposition of the films is executed by a phased single step spin-coating procedure. The exposures were performed using mercury UV-lamp exposure with binary or grayscale photomasks, or using UV-laser irradiation.

RESULTS AND DISCUSSION

By careful design and control of the hybrid glass material's synthesis, we demonstrated the fabrication of optical structures with large thicknesses by using the both methods (see Figure 1 and Figure 2).

Figure 1(a) shows a surface-topography measurement of a lenslet patterned using a grayscale photomask and a 2-sec mercury UV-lamp exposure (UV dose of 21.2 mJ/cm^2). Figure 1(b) shows a profile of the same lenslet. The achieved patterned depth in this case was 75 μm. Figure 1(c) shows two lithographically patterned opto-mechanical features patterned in hybrid glass using a binary photomask and a 2-sec mercury UV lamp. These positioning features were patterned to an average height of 118 microns. The *rms* surface roughness of the fabricated structures was measured to be in the range of 10 nm to 45 nm. The achieved patterned thickness of 75 μm can be interpreted in terms of a refractive micro-optical element. With a 480 μm clear aperture, a refractive lenslet can be patterned with f_e = 0.8 and a numerical aperture of NA = 0.29.

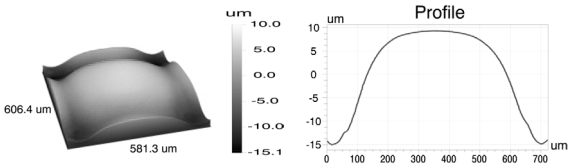

(a) (b)

Figure 2. Part (a) shows a segment of a lenslet array fabricated by direct photolithographic deforming of a deposited hybrid glass film using a grayscale photomask. Part (b) shows a diagonal profile of the surface. Lens sag was measured to be 24 microns. Image taken with NT3300 optical profiler, courtesy Veeco Metrology Group.

Figure 2(a) shows a surface-topography measurement of a lenslet fabricated by direct photolithographic deforming using a grayscale photomask and a 2-sec mercury UV-lamp exposure. Figure 2(b) shows a profile of the same lenslet. The achieved deformation height in this case was 24 μm. No development step was used in the fabrication. The *rms* surface roughness of the fabricated structures was measured to be in the range of 1-10 nm. The observed deformation phenomenon is caused by the diffusion reactions and physical expansion and/or reorientations of the monomer and oligomer constituents in the hybrid glass film.

CONCLUSIONS

By using the negative tone hybrid glass materials and grayscale lithography, photolithographic patterning of various optical structures, such as gratings, waveguides, lens arrays (Figure 1), and individual lenslets is possible. In addition to optical structures, alignment-aiding opto-mechanical structures can be patterned simultaneously in the hybrid glass to fabricate micro-optical elements. Such elements can be used in, e.g., micro-optical table (MOT) systems. Grayscale lithography using photomasks or an UV laser permits the controlled patterning of nearly arbitrary, high-quality optical surfaces, e.g., conics and aspheric surfaces.

The photolithographic deforming of hybrid glasses can be also applied to fabricate variety of micro-optical structures. The fabrication of, e.g., single lenses, lens arrays (Figure 2) and sinusoidal gratings can be performed.

REFERENCES

[1] S. Sinzinger, J. Jahns, *Microoptics*, Wiley-VHC, Weinheim **1999**, Ch. 1-5.
[2] M. Eisner and J. Schwider, *Opt. Eng.* **1996**, 10, 2979.
[3] G. M. Morris, *Proc. SPIE - Int. Soc. Opt. Eng.* **1998**, 3573, 370.
[4] J. Mohr, *Sens. Mater*. **1998**, 10, 363.
[5] R. K. Kupka, F. Bouamrane, C. Cremers, S. Megtert, *Appl. Surf. Sci.* **2000**, 164, 97.
[6] M. J. Riedl, *Photonics Spectra* **2001**, 35, 130.
[7] W. R. Cox, T. Chen and D. J. Hayes, *Optics & Photonics News* **2001**, 12, 32.
[8] Keyworth B. P. et al., *US Patent 5 534 101*, **1998** and Keyworth B. P. et al., *US Patent 5 723 176*, **1998**.
[9] B. E. Yoldas, *J. Sol-gel Sci. Tech.* **1998**, 13, 147.
[10] P. Äyräs, J. T. Rantala, R. Levy, M. R. Descour, S. Honkanen and N. Peyghambarian, *Thin Solid Films* **1999**, 352, 9.
[11] J.T. Rantala, R. Levy, L. Kivimäki, and M.R. Descour, *Electron. Lett.* **2000**, 16, 530.
[12] J. T. Rantala, A. H. O. Kärkkäinen, J. Hiltunen, M. Keränen, T. Kololuoma and M. R. Descour, *Opt. Express* **2001**, 8, 682.

Advanced Material Techniques for NIR-laser Protection

Mikko Keränen and Terho Kololuoma

INTRODUCTION

We have previously reported on the fabrication of mechanically stable NIR-absorbing organic dye molecule doped sol-gel coatings on a polycarbonate visors [1]. These coatings have optical density of over 4 at 1064 nm, while their optical transmission at visible wavelengths is at a satisfactory level, being ~70 % at 590 nm. However, these coatings are still lacking chemical stability, which diminishes their usefulness in battlefield conditions. The most alarming results were obtained during the water stability test, which diminishes the optical density of the coating at 1064 from 4 to 2. Transmission at visible wavelengths was also reduced during the water test; the coatings became strongly absorbent at blue wavelengths.

In order to increase the water tolerance of the coatings, a couple of methods were investigated. The first method involves the introduction of fluorine to the coatings via fluoroalkyl substituted silane alkoxide precursors, or as an individual hydrophobic layer on top of the absorbing layer. Additionally, the stabilities of different dye molecules were also investigated. In the other method NIR-absorbing organic dye molecules are doped in the sol-gel derived material that can be used as a glue material during the lamination process of the laminated polycarbonate visors. When NIR-absorbing dye molecules are placed between two polycarbonate laminate sheets, only the surrounding temperature, from environmental stresses, is capable of degrading the molecule.

IMPROVED COATINGS

The fluoridation of the coatings, using 3,3,3-trifluoropropyltrimethoxysilane as an additional fluorinated sol-gel precursor (20 mol.-% vs. the amount of other alkoxide precursors [1]) during the material synthesis, did not increase the water stability of the coatings. Similar results were obtained, as when the individual, commercially available hydrophobic coating was used (Gelest aquaphobe CF). Obviously, used dye molecule (SDB6592 acquired from H.W.Sands) is too sensitive against water. Because of this, a new kind of absorption molecule was purchased (SDA7684, H.W.Sands).

The sol-gel material capable of forming mechanically stable coatings was synthesized as described before [1]. The coating solution was fabricated by mixing equal volumes of fabricated sol-gel solution and 10 mM SDA7684 solution in methanol. Additionally, 10 µl of Byk-306 / 2 ml of coating solution was added as a levelling agent to coating solution. After 24 hours of ageing at room temperature, the coatings were fabricated by spray-coating method. Coatings were finally cured at 80°C for 30 minutes.

In order to investigate the water stability of this new absorbing molecule, a water test was carried out according to the US mil 810D standard. In figures 1a and 1b, the optical properties of the coatings before and after the water test are shown. As can be seen, the water test causes only minor changes to the optical properties of the SDA7684 doped sol-gel coatings. Optical density at the laser-threat wavelength (1064 nm) is decreased from 4.8 to 4.5, being still at the required level (OD > 4). Furthermore, the transmission maximum at visible wavelengths is 10 % higher when compared to the same type of sol-gel coatings doped with SDB6592.

LAMINATED VISORS

Most inorganic-organic sol-gels have adhesive-like properties and excellent adhesion to several different kind of substrate material, e.g. glass, plastics and metals. The excellent optical properties of the sol-gel based adhesives offer many applications in optics. Sol-gel derived adhesives, in comparison to commercial polymer based adhesives, have high resistance against temperature and high mechanical durability [2]. However, during the sol-gel adhesive fabrication, many rapid reactions take place. These rapid reactions, e.g. epoxy glues react rapidly with amine-based hardener [3] and isocyanato based materials with water [4], impede the fabrication process of laminated visors. We offer a route

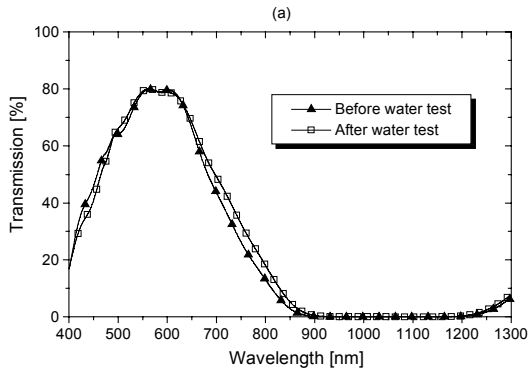

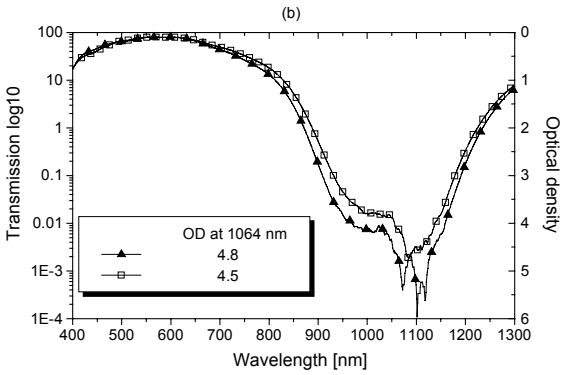

Figure 1a and 1b. Optical properties of the water tolerant NIR-absorbing coating on a polycarbonate substrate: (—▲—) before water test, (—□—) after water test.

to control these rapid reactions, and therefore make these adhesives suitable for use with different coating methods, e.g. spin- and spray-coating. One application in optics is laminated structures for lenses and visors with improved ballistic properties e.g. in military technology. The adhesive properties of this new material are based on the reactions between 3-aminopropyltrimethoxysilane (APTES) and 3-glycidyloxypropyltrimethoxysilane (GPMS). Material has very good adhesion on polycarbonate substrate and moreover excellent peel off -properties (25-30 kg/cm^2). The temperature needed for isostatic (hot-pressing) lamination was also low, only +70^{o}C.

Alkoxide precursor solutions, GPMS, APTES and MAMPS (methacryloxypropyltrimethoxy-silane), were weighted into the flask and the solution was stirred for 15 minutes. Then 0,1 M HCl was added to the solution (7,5 wt-% in isopropylalcohol, IPA) and the solution was stirred for four hours, to produce final sol-gel coating solution. Molar-ratios for the precursors were GPMS:MAMPS:APTES:H_2O 6:2:1,5:9,5, respectively. Before coating, the solution was filtered through a 0,45 µm PVDF-membrane filter. Coatings were prepared by the spray-coating method on PC-substrate and another PC-substrate was set onto sol-gel-coated PC. The structure was laminated using isostatic laminator for 30 minutes at 2000 psi and +70^{o}C. The optical properties of the laminated structure can be seen in figure 2.

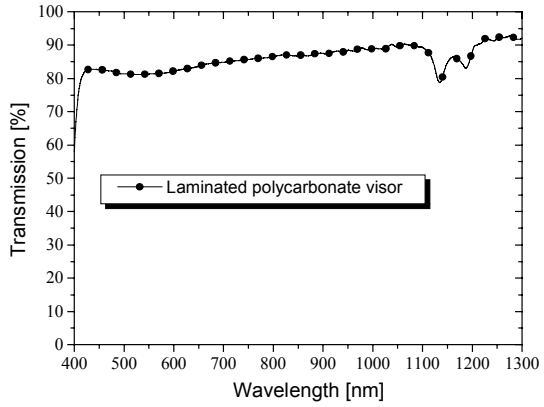

Figure 2. Optical properties of the laminated structure.

In order to obtain the required laser protection at 1064 nm, the glue material was doped with NIR-absorbing organic dye molecules. Unfortunately not all investigated dye molecules were compatible with glue material and hence the glue material has to be modified. However, the absorbing dye molecule compatible modified glue material had poor peel off properties (2-3 kg/cm^2) and it is not suitable to be used in military protective eyewear.

REFERENCES

1. T. Kololuoma, J. A. I. Oksanen, P. Raerinne and J. T. Rantala, 16 (2001), 2186-2188.
2. T. Nakagawa, M. Soga, J. of Non-Crystalline Solids, 260 (1999) 167-174.
3. J. Comyn: *Epoxide Adhesives* in the book *Handbook of Adhesion* Edited by D.E. Packham, Longman Scientific & Technical, (1992), 154.
4. H.Ni, D.J. Aaserud, W.J, Simonsick Jr., M.D. Soucek, Polymer, 41 (2000) 57-71.

Novel Synthesis Route to Conductive Antimony Doped Tin Dioxide and Micro-Fabrication Method

Terho Kololuoma, Ari. H.O. Kärkkäinen and Juha T. Rantala*
(*GuideOptics Oy, P.O.Box 114, FIN-90571 Oulu, Finland)

INTRODUCTION

Among the conductive sol-gel derived materials antimony doped tin dioxides have gained much attention, mostly because of their suitability for use as transparent anodes in different kind of display devices [1], solar cells and also due to their capability for gas sensing applications [2]. Typically, these applications require the patterning of conductive tin dioxide films. Conventional methods, such as dry and wet etching, have been applied in the thin film patterning. Wet etching has been reported to be relatively difficult because of the high chemical stability of tin dioxide [3]. Although dry etching patterning methods have been successfully demonstrated, they are usually time-consuming, expensive and special equipment is needed. Photopatternable materials derived directly from sol-gel have shown their potential with other types of materials but only a few articles concerning the direct photopatterning of semiconductive oxides exist [3-6]. Furthermore, in these previous publications, high UV-doses, even pulsed UV-lasers, at wavelengths typically below 300 nm were applied to pattern the material. In addition, all of those publications were only concerned with the production of directly photopatternable pure tin dioxide.

In this study, a novel method for the production of directly photopatternable pure and antimony doped organo tin polymers via free-radical polymerization of methacrylic acid ligands is presented. The initiation of radical polymerization can be achieved by using mercury I-line UV-lamp exposure. Polymerized organo tin films are decomposed by thermal annealing to crystalline, conductive pure or antimony doped tin dioxide films.

EXPERIMENTAL

The directly photopatternable pure and antimony doped tin dioxide materials were synthesized by reacting methacrylic acid with tin and antimony alkoxide solutions in 2-isopropoxyethanol. As a first step, the tin(IV) isopropoxide and antimony(III)isopropoxide were dissolved separately in dry 2-isopropoxyethanol. The concentrations of tin and antimony alkoxide solutions were 0.5 M, except in the case of the undoped samples, where tin(IV)isopropoxide concentration was 1 M. In order to obtain the desired antimony doping level (1-10 mol.-%), a suitable amount of the antimony alkoxide solution was added and mixed well with the tin alkoxide solution. After this the methacrylic acid was added drop by drop to the metal alkoxide solution. The amount of methacrylic acid added, in moles, was twice the amount of tin and antimony alkoxides. The mixtures were left to react overnight. Before film deposition, 2 wt.-% of Irgacure 819 (Ciba) corresponding to the mass of used methacrylic acid was dissolved as a photo initiator into the solutions.

The pure and antimony doped tin dioxide thin films were produced by the spin-coating method and patterned by direct UV-lithography as follows. A suitable amount of pure or antimony-doped solution was filtered through a 0.45 µm PVDF-membrane syringe filter onto the borosilicate glass substrate. Thin films were formed in a two stage spinning process: first the solution was spread on the substrate for 5 seconds at 500 rpm and then spun-on for 30 seconds at 1250 rpm. After spin coating the films were patterned by using a binary photomask and UV-irradiation from a mercury UV-lamp source (10 mW/cm^2 at 365 nm). The suitable UV-dose was found to be between 300 and 400 mJ/cm^2. Alcohols such as methanol and isopropanol were found to be appropriate developers. After the development step the films and structures were first dried at 140°C. After this the organo tin polymer was pyrolytically decomposed onto the crystalline, pure or antimony doped tin dioxide in ambient atmosphere at elevated temperature. The highest temperature during the annealing was 560°C for 20 minutes.

RESULTS AND DISCUSSION

In figure 1 the fabricated thin film structures are shown. Figure 1a shows a scanning electron microscope (SEM, JMS-6400) image of patterned grating structure with 6 µm grating period. Figure

1b shows a cross sectional profile (Wyko NT 2000) of a conductor line with a 25 µm line width. The smallest obtained feature size during the experiments was 3 µm.

(a)

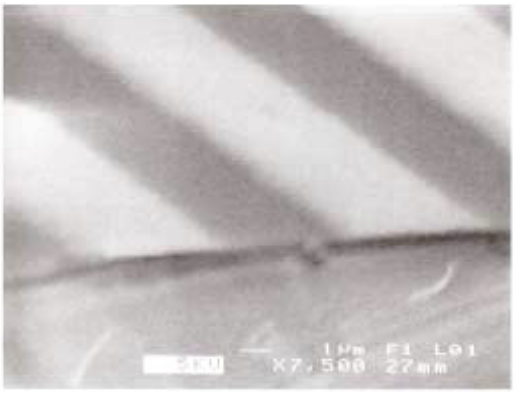

(b)

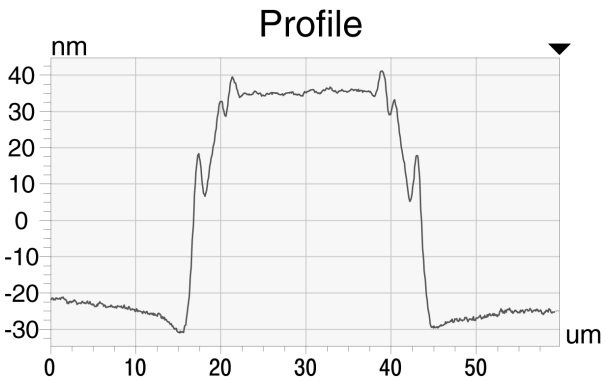

Figures 1a and 1b. Fabricated thin film structures. a) Presents a SEM image of a patterned grating structure with 6 µm period. b) A cross sectional profile (Wyko NT 2000) of a conductor line with 25 µm line width.

Film thicknesses, sheet resistances and resistivities, which are average values from three different samples, are presented in Table 1. The differences in film thicknesses result from the viscosity of the solutions, which is due to the differing concentrations of the undoped (1.0 M) and doped solutions (0.5 M). The experiments revealed that the UV-irradiated (ID) films clearly have better conductivity than the unexposed (UT) films.

CONCLUSIONS

For the first time, directly photopatternable pure and antimony doped tin dioxide thin films were successfully prepared via modification of the tin and antimony alkoxide precursors with methacrylic acid. All the materials were photopatterned to feature sizes as small as 3 µm. The lowest obtained resistivity, 0.08 Ω·cm, for the single layer thin film, was achieved when antimony doping concentration was 5 mol.-%. UV-exposure and development of the fabricated films was noticed to increase the conductivity of the films.

Table 1. Thicknesses, sheet resistances, resistivities and conductivities of fabricated pure and antimony doped tin dioxide thin films.

Sample (c(Sb) mol.-%)	t (nm)	R_s (kΩ/sq.)	Resistivity (Ω·cm)
UT (0)	120	11000	132
ID (0)	110	6100	67
UT (1)	70	119	0.85
ID (1)	55	37	0.21
UT (5)	75	25	0.18
ID (5)	65	11	0.08
UT (10)	72	69	0.5
ID (10)	64	48	0.3

REFERENCES

1. S.–S. Park, J.D. Mackenzie, Thin Solid Films 258 (1995) 268, and references therein.
2. D. Kohl, Sensors and Actuators 18 (1989) 71.
3. T. Tamai, N. Ichinose, S. Kawanishi, M. Nishii, T. Sasuga, I. Hashida, K. Mizuno, Chem. Mater. 9 (1997) 2674.
4. K. Koichi, S. Kiichiro, T. Katsuhiko, H. Shinichi, J. Am. Ceram. Soc. 82 (1999) 2263.
5. K. Tadanaga, T. Owan, J. Morinaga, S. Urbanek, T. Minami, J. Sol-Gel Sci. Tech. 19 (2000) 791.
6. Q. Wei, H. Zheng, Y. Huang, Solar Energy mat. & Solar cells 68 (2001) 383.

LTCC TECHNOLOGY IN MODULE PACKAGING

RF-modelling of integrated passives on LTCC

Antti Vimpari

LTCC-Technology enables the integration of passive components and circuit elements into the substrate. That is useful for cost reduction and miniaturising, especially in the telecommunications industry. The need to reduce prototype design rounds places demands on circuit element modelling to utilise the CAD-tools with good simulation capabilities in electronics design. The consistent need to go higher in frequency also makes the modelling more significant.

THE CIRCUIT ELEMENT CATEGORIES

Passive circuit elements can be divided into a number of categories: transmission lines, inductive, capacitive, and resistive elements. More complex structures like resonators and filters can also be distinguished. They are more application specific cases and the modelling and design of filter and resonator structures is the application engineer's work. However the engineer needs verified design rules and a set of parameters to describe the electrical behaviour of the materials.

Transmission lines are needed to transfer RF-signals, which can also be called RF-power. In transmission line modelling the aim is that an application engineer can define geometries for the transmission line so that the electrical and physical specifications are met. The important performance parameters are reflection attenuation, i.e. the characteristic impedance, insertion loss and usable bandwidth. In some cases, parameters like ripple or even passive distortion can be significant. Transmission lines are often modelled by simulation tools with the equivalent circuits. With equivalent circuits, the modelling capability is commonly limited to below 10 GHz. More thorough analysis needs 3D-electromagnetic simulation softwares that are available nowadays. In fig. 1, a 3D-simulation of a 10 GHz RF-signal propagating through the coplanar wave-guide transmission line with ground plane is presented.

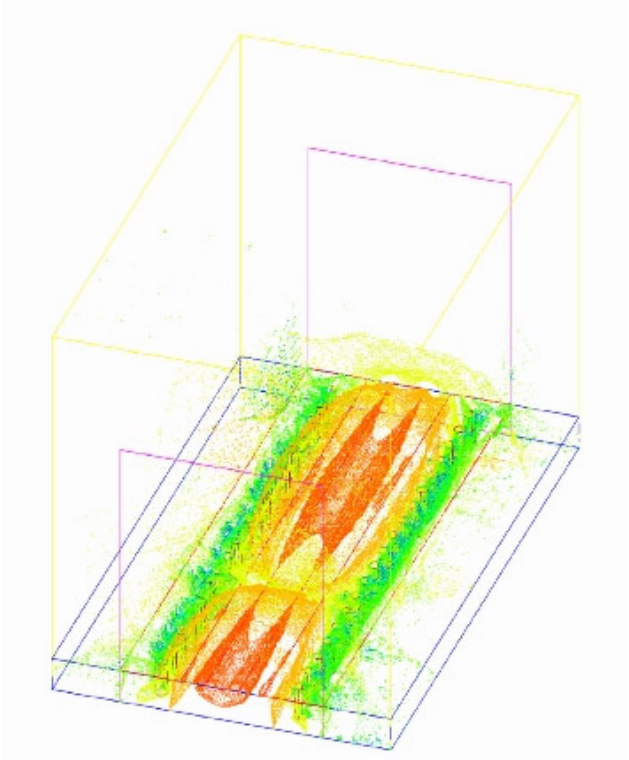

Figure 1. Simulated electromagnetic fields of coplanar wave-guide

.

Inductive circuit elements are needed for inductance realisation in electronics design. A coil is often the first idea when it comes to realising inductance, but in a planar multilayer environment coils are not possible. On the contrary, spiral inductors are generally used to make inductors. To model a spiral inductor, the mutual coupling of the spiral turns must be taken into account. That makes spiral modelling complex. Moreover, the parasitic capacitance to the ground plane and from turn to turn must be modelled as well. Spiral inductors, especially without a ground plane, can have high Q-values (more than 100). That makes the inductor resonate strongly with the turn-to-turn parasitic capacitances. Also some other parasitic resonances take place. The modelling should naturally be able to predict at least the significant resonances and the Q-value properly. So far, the appropriate spiral inductor modelling is only possible with 3D-simulation softwares. Equivalent circuit models can be made but they must be defined separately for each spiral geometry. They do not usually predict all the resonances. Inductances can also be realised with properly designed transmission line elements. This is a very common way to realise low inductances with low loss for narrow band RF-applications. Transmission line elements are much easier to model than spiral inductors.

Capacitive elements can be realised, for example, with multilayer plate structures. Unfortunately they have a relatively high parasitic capacitance to the grounded shielding. Plate capacitors are not useful in microwave applications, but interdigital capacitors are a better choice. In fact they act as coupling co-planar striplines, and good insertion loss properties can easily be achieved at up to 10 GHz of frequency. Interdigital capacitors tend to have series resonance when the overlapping finger length is about quarter of the wave length or its odd multiply and parallel mode resonance when the overlap is about half of the wave length or its odd multiply. Because interdigital capacitors are actually transmission line structures, they are quite simple to model even without 3D-simulation tools. On the contrary, plate capacitors demand 3D-analysis if the plate dimensions are in the range of one tenth of wavelength or more. In fig. 2, a 10 GHz RF-signal propagating through the 3-finger interdigital capacitor is presented. From the figure it can be seen that there is hardly any discontinuity in the electric field on the long side of the fingers but the finger ends cause some discontinuity. Along the long sides there must be strong coupling between the fingers.

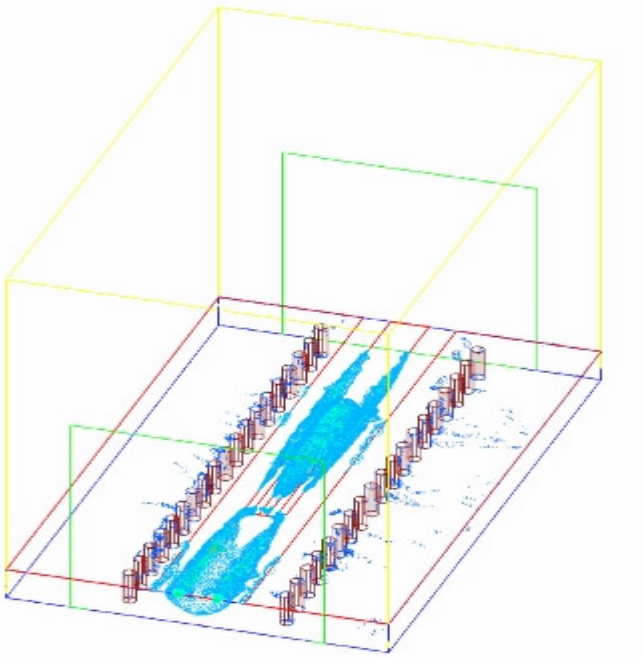

Figure 2. Electromagnetic simulation of 10 GHz RF going through the 3-finger interdigital capacitor.

Millimeter-Wave LTCC Transmission Media Characterization

Joey R. Bray

INTRODUCTION

While the demand for wireless telecommunication services continues to increase, the availability of free spectrum to implement new systems continues to dwindle. This, combined with the demand for high quality broadband services, provides the impetus for the development of millimeter-wave systems.

Recognizing the market potential for their application at microwave and millimeter-wave frequencies, suppliers of LTCC have recently introduced low loss tape systems. Although some suppliers have begun to characterize the performance of these materials in the millimeter-wave band, others have not. LTCC modules have been fabricated at VTT to further the characterization of millimeter-wave transmission media.

The guidance of millimeter-wave signals at the electronic packaging level poses many challenges. As frequencies increase, the tolerances required to maintain the low loss operation of transmission lines become more strict. The skin effect in conductors becomes more pronounced, which causes current to flow in smaller cross-sectional areas and increases the conductor loss. Additionally, radiation, be it launched into the air or into the substrate itself, also becomes an important concern.

MICROSTRIP TRANSMISSION LINES

Due to its simplicity, microstrip is the most popular transmission medium at microwave frequencies. Although the design of microstrip at millimeter-wave frequencies can be problematic, it is nonetheless still feasible. Two different experimental techniques, both using vector network analysis, will be used to gauge the performance of microstrip lines.

The first measurement technique employs the Thru-Reflect-Line (TRL) calibration method. In essence, this technique removes the effects of the lines and transitions leading from the network analyzer to the substrate so that the microwave performance of the microstrip line alone may be ascertained. TRL calibration standards and microstrip lines operating from 2 to 40 GHz have been constructed in LTCC, and a layout is shown on the left hand side of Figure 1.

If the loss of the microstrip line is too small, the accuracy of the TRL measurement will be compromised. Resonators compound the loss at their resonant frequencies and thereby allow low loss lines to be characterized more precisely. Microstrip rings with resonant frequencies ranging from 5 to 40 GHz have been fabricated in LTCC. One such ring is shown on the right hand side of Figure 1.

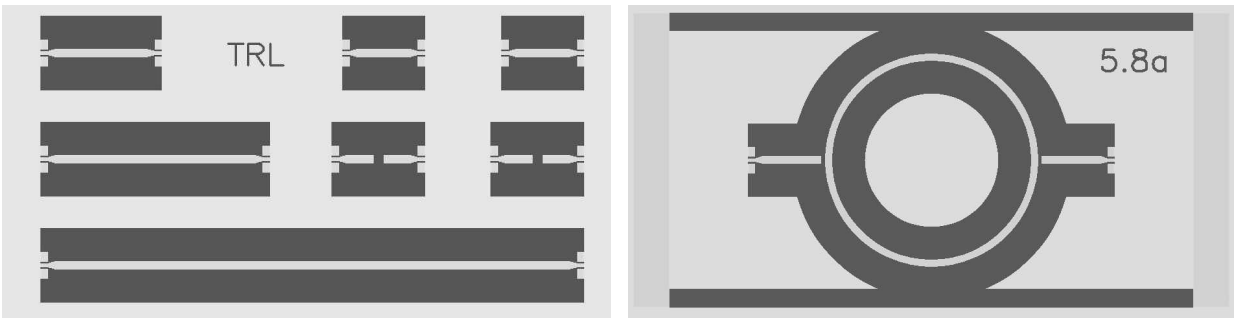

Figure 1. Layouts of microstrip TRL calibration standards (left) and of a ring resonator (right).

VIA WAVEGUIDE IN LTCC

As previously mentioned, the design of microstrip at millimeter-wave frequencies is potentially problematic using LTCC. Specifically, radiation loss into the substrate becomes a problem unless the height of the microstrip substrate is small with respect to the TEM wavelength. For most LTCC materials, this means that only one tape layer may be used as the microstrip substrate. To maintain a 50 Ω line impedance, the required width of the microstrip line is so small that it begins to approach the practical screen printing limit of LTCC. For very thin substrates, the width of the microstrip line becomes so small that it requires more expensive photoimaging. As the width of the line decreases, the roughness along its edges has a more pronounced effect on the conductor loss.

Rectangular waveguides were largely abandoned by the early 1980s in favor of planar transmission media. However, the three dimensional capabilities of LTCC allow for their simple integration if the solid narrow walls of the waveguide are replaced by rows of vias. The via waveguide is shown conceptually on the left hand side of Figure 2. Waveguides have several advantages over planar transmission lines such as microstrip. For instance, the skin effect does not cause current to crowd near any edges, thereby lowering the conductor loss. Also, the fields within the guide are distributed over a greater volume than in microstrip, meaning that much higher power handling capabilities may be realized. Further, due to the confinement of the fields within the guide, radiation leakage and spurious coupling are less likely to occur. Finally, the guide is buried in the lower levels of the module, freeing the top layer so that it may contain more chips, passives, or post-fired components.

Similar to the microstrip methodology, both TRL calibration standards and cavity resonators have been fabricated using via waveguide in the 30 to 40 GHz frequency band. The right hand side of Figure 2 shows a layout of two lengths of via waveguide.

SUMMARY

Measurements are currently being performed to determine the loss characteristics of LTCC at millimeter-wave frequencies. Microstrip loss will be evaluated using TRL calibration and ring resonators. Via waveguide propagation constants will be determined using TRL calibration and cavity resonators.

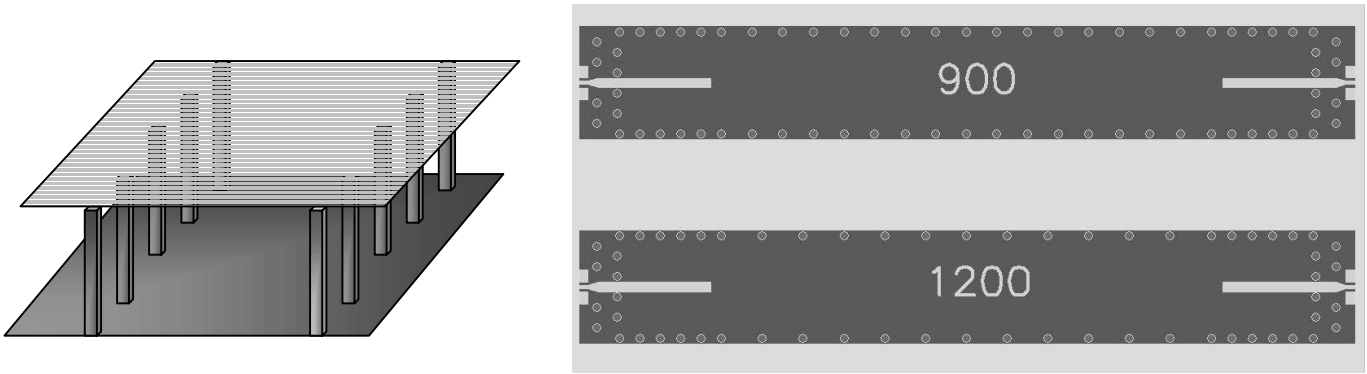

Figure 2. Conceptual via waveguide (left), and layouts of two via waveguide lengths using different via pitches (right)

Etched fine line conductors on LTCC

Markku Lahti

INTRODUCTION

LTCC technology has been adopted by many users in to a great extent during recent years. In addition to the use of multilayers, the ceramic interconnection density can be further increased by using thick-film conductors, which are based on photo-patterning techniques. Photo-processed conductors can be photoimageable or photodefinable. The former use photosensitive thick-film materials, which are printed, dried and photo-patterned before firing. The latter use materials optimized for printing and firing a smooth and dense conductor, which is then etched to give a final pattern.

Nowadays, the minimum line widths and gaps are 100 µm for direct screen-printed conductor lines, 50 µm for photosensitive lines and 20 µm for etched lines. The accuracy of line edge is also considerably better in the case of photopatternable conductors. [1]. The photoimageable conductors can also be realized on inner layers, whereas the etching technique is limited only for surface layer. This study has concentrated on the development of etching technique on LTCC. Processing parameters were optimized and the dependency of conductor line properties on the etching parameters was studied.

EXPERIMENTAL WORK

The principle of the etching process is shown in Fig. 1. Prior to the etching process, the layers of the LTCC substrate are printed, laminated and fired normally. The Ag layer is screen-printed and fired on the surface (1). The resist is spun over the surface (2). Then, the resist is patterned using the UV exposure (3). During development, the pattern is formed in the resist layer (4). After this the unprotected metal layer is etched (5) and finally the remained resist is dissolved (6).

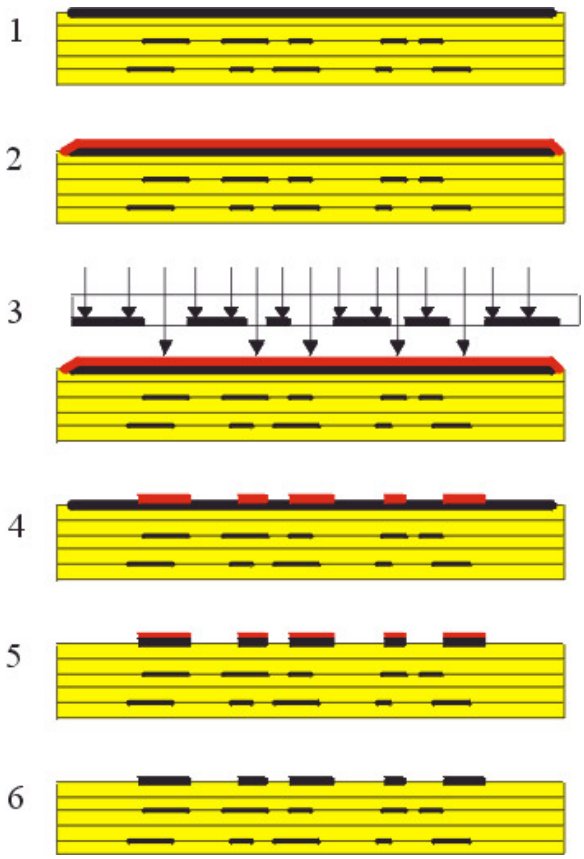

Figure 1. The principle of the etching process.

Silver paste KQ610A (Heraeus) was used for etching. The paste was screen-printed using 325 MESH screen with the emulsion thickness 12 µm. After printing, the pattern was dried and fired. Then the procedure was repeated in order to form a denser metal layer. Heraeus CT2000, Du Pont 951 and Ferro A6-S tapes were used as substrate materials. The thickness of fired conductor lines was about 15 µm, varying slightly in separate printing trials.

Positive photoresist AZ4562 (Clariant) was spun over the LTCC substrate with the deposition profile recommended by the manufacturer. The spinning speed was 3000 rpm that resulted in the resist thickness of 6-7 µm. The exposure was made with a Karl Suss mask aligner, which used a wavelength of 380 nm. During exposure the substrate and the mask were in contact. The intensity of the exposure was 14.0 mW/cm^2. The exposure time was an essential parameter in defining the line width in the resist. Typically it

was 20 s. By increasing the time to 25 s, the line widths in the resist decreased by 2-3 µm.

The development was made in a solution of AZ400K and water (1:4). The development time varied depending on the conditions of the solution. For a fresh solution it was 60 s. The etching was made in KI/I_2 solution at temperature of 45 °C. The etching time was the most important parameter affecting the properties of conductor lines. It depended on the metal thickness and it was about 5 min for typical conductor thickness. The etching speed of Ag was 3.0-3.6 µm/min.

The narrowest etched lines were about 20 µm wide. The variation of the line width was within ±3 µm. The minimum gaps were 30 µm. The under-etching depended on the conductor thickness and etching time. Typically, the width of conductors decreased by 12-16 µm from nominal values.

The resistivity of the lines was 2.5×10^{-8} Ωm on average. As shown in Fig. 2 there were some voids in the conductors, which increased resistivity. Fig. 3 shows an overview of the etched Heraeus conductors of different widths on Du Pont 951 tape. The compatibility between the tapes and pastes from different manufacturers was good enough.

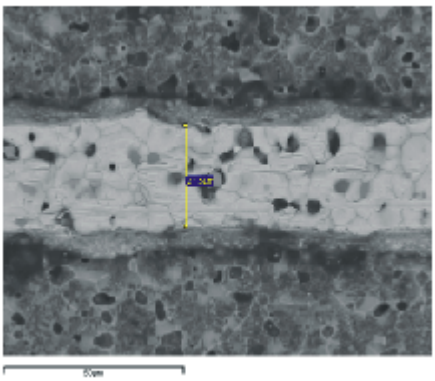

Figure 2. a) SEM photo of 30 µm wide Ag conductor.

Figure 3. The optical microscope photo of etched conductors on DP951 tape. The narrowest lines are 40 µm wide.

SUMMARY

The etching technique proved to be a useful tool for fabricating narrow and good-qualified conductors on LTCC tapes. The narrowest line widths were about 20 µm with the line accuracy of ±3 µm. The control of the etching time is an important parameter to define the amount of under-etching.

REFERENCES

1. P. Barnwell, "Ceramic Circuitry – A Technology for the Future", Proc. of IMAPS Nordic, Oslo, Norway, September 23-26, 2001.

Dimensional tolerances of LTCC substrates

J. Petäjä, K. Kautio

INTRODUCTION

Low temperature co-fired ceramic technology (LTCC) has been used in many different types of applications and has offered packaging solutions with high density, good high frequency characteristics, reliability and cost efficiency. One of the known drawbacks of LTCC is the firing shrinkage tolerance, which is normally in the order of 0.2% in x,y direction. This may cause problems in the component assembly process, especially with fine pitch components.

In this work, the dimensional tolerances and accuracy of LTCC substrates, fired in a free sintering process, was characterised. Furthermore, the constrained sintering of LTCC substrates was evaluated.

LTCC SUBSTRATE ACCURACY IN A FREE SINTERING PROCESS

DuPont 951-A2 (165 µm thick) and 951-AX (254 µm thick) tape systems were used in this test. The green sheets were cut to size 168x168 mm and stabilised in a heating step. The via test pattern for the dimensional measurements was punched into the top layer and filled with Ag paste. Test laminates of either four layers of 951AX or six layers of 951A2 were stacked, having the via pattern on the top layer, while all the other layers were blanks. Subsequently, the panels were laminated in an isostatic laminator at 3000 psi. Sintering of the laminates was carried out on alumina setter plates in a Sierratherm elevator batch furnace at 875 ^{o}C. The test panel layout is shown in Fig. 1.

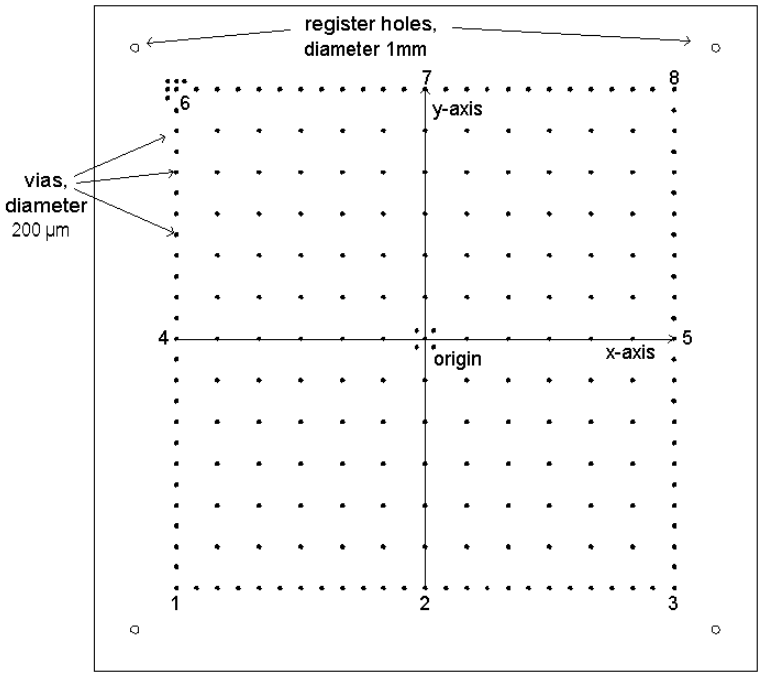

Figure 1. Test pattern for LTCC substrate dimensional measurement

The via test pattern was first measured with a video measuring microscope on the separate tape sheet, the result being the same as the nominal coordinate values within 10 µm. After the lamination step, the test pattern typically spreads in x and y direction 0.03%, which is negligible compared to the dimensional changes during the firing step. After lamination, no distortion of the test pattern was seen either.

In a free sintering process, the shrinkage for Du Pont 951 material in x,y direction is typically

13%. A two dimensional map of the measured via coordinates wasdrawn, as shown in Fig. 2. The designed via grid is shown and the measured one on top to see the substrate distortion clearly. The error of the measured via coordinates, compared to the nominal coordinates, is multiplied by 100 to exaggerate the substrate distortion.

As seen in Fig. 2, the shrinkage is uneven across the substrate and the biggest distortion is seen at the substrate corners. This is due to the firing temperature deviation of about +/- 2.5 degrees within the substrate area. Possibly, also the air-flow between the setter plates may not be quite uniform, which can affect the firing properties of the dielectric.

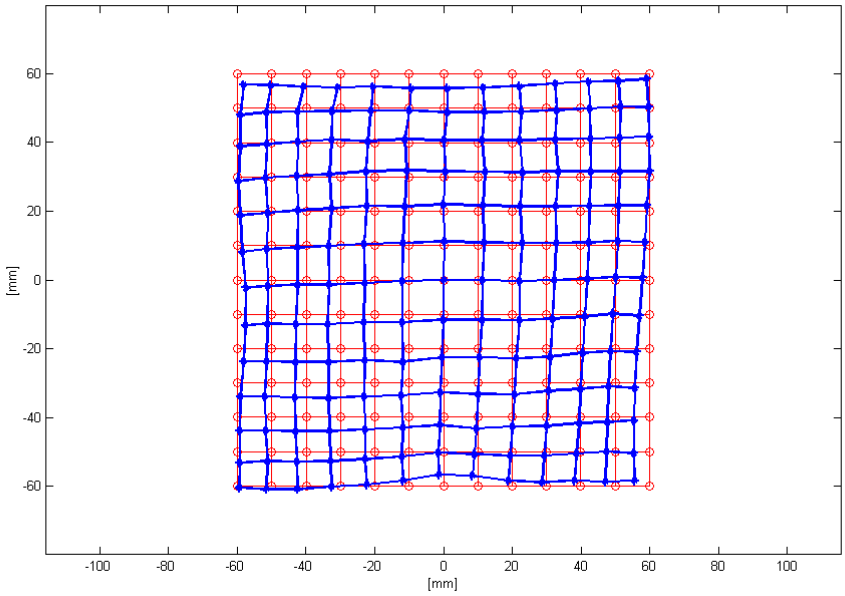

Figure 2. Example of a six layer 951-A2 substrate dimensional measurement

No big differences were noticed between DuPont 951-A2 and 951-AX tape systems. The average firing shrinkage for 951-AX laminates was 12,94 % ± 0,15 % and for 951-A2 laminates 12,98 % ± 0,08 %.

The biggest possible via mislocation was determined from a lot of 15 test substrates of each type. The average x,y- coordinate of the corner via (see point 3 in Fig. 1) was first determined. Compared to the average value, the maximum via mislocation within the manufacturing lot was 135 µm for the 951AX substrates and 116 µm for the 951-A2 substrates.

EVALUATION OF ”ZERO SHRINK” FIRING PROCESS

The firing shrinkage of an LTCC laminate can be prevented using constraining ceramic tape layers, which are laminated on both sides of the LTCC stack. The shrinkage in x and y directions is thus almost totally eliminated, while the shrinkage in z direction is increased. The constraining layers (release tape layers) are removed after firing mechanically, e.g. by brushing.

Test panels of Du Pont 951, manufactured by the constrained sintering method, gave an average firing shrinkage of 0.18 % with a tolerance of only 0.02 %. The distortion of the substrates was minimal, as can be seen in Fig. 3. The maximum misalignment of the corner vias was 12 µm, compared to over 100 µm in the free sintering method.

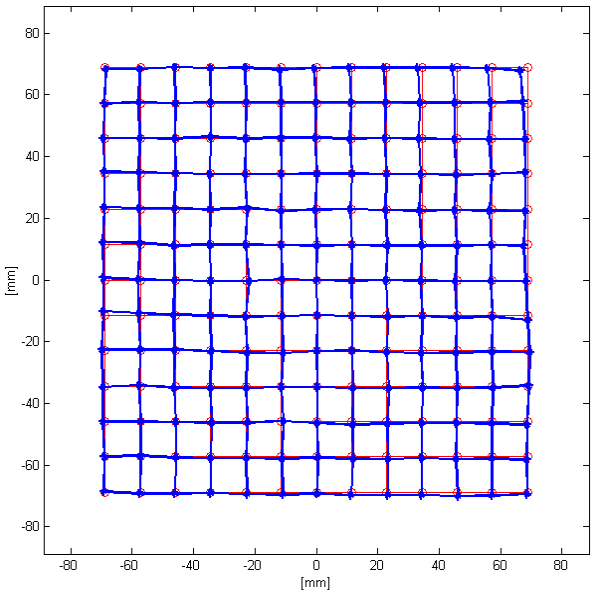

Figure 3. Example of 951-AX test substrate measurement in the constrained sintering process

CONCLUSION

The dimensional tolerances of LTCC substrates, fired in a free sintering patch process, were evaluated in this work. It was seen that the distortion of the x,y dimensions within the substrate area can be big enough to cause problems in the component assembly process. The statistical information, given by the tests, can be used to further optimize the firing process.

Constrained sintering of LTCC laminates gives very small firing shrinkage tolerances and is a potential method for future LTCC applications, where higher precision is demanded. The possibility of increasing the panel size with good accuracy can also improve the cost effectiveness of LTCC in the future.

Passively aligned fiber-optic transmitter integrated into LTCC module

Mikko Karppinen, Kari Kautio, Mikko Heikkinen, Jonna Häkkilä, Pentti Karioja,Tomi Jouhti*, Ari Tervonen*, Markku Oksanen*
(*Nokia Research Center, Finland)

INTRODUCTION

We studied the suitability of LTCC-based multi-chip-module technology for passively aligned fiber-optic applications. Low-cost and small in size optoelectronic transceivers are needed for short-distance applications, such as optical interconnects. The use of passive fiber alignment during the packaging process is required when aiming to the low-cost fiber pigtailing. This is typically realized using precision-machined parts and alignment structures [1]. LTCC (low temperature cofired ceramics) technology, however, can provide alignment structure on the module substrate. LTTC also enables high packaging density due to its multilayer structure and possibility for passive-component integration and bare-chip encapsulation. In addition, good high frequency and thermal properties as well as stability, reliability and cost efficiency are advantageous for high-speed optoelectronics. According to previous studies, mechanical tolerances (~10 µm) are, potentially, adequate for passive alignment of multimode fibers. This was studied by designing and demonstrating an arrayed transmitter structure with fiber pigtails and small printed-circuit-board (PCB) footprint.

MODULE DESIGN

The designed transmitter structure (Fig. 1) was targeted for standard multimode fibers and flip-chip-bondable vertical-emitting light sources, such as vertical-cavity surface emitting lasers (VCSEL). In order to be suitable for high-density arrayed interconnections, the vertical mounting of optical fibers to the LTCC substrate was chosen, and the integration of a laser-driver chip and discrete passives onto the substrate was realized. To minimize the PCB area required by the module, it was designed to be vertically mountable on a PCB using conductive adhesives. This kind of fiber pigtailed module has essentially one-dimensional footprint and can be used as a detachable electrical-optical interface.

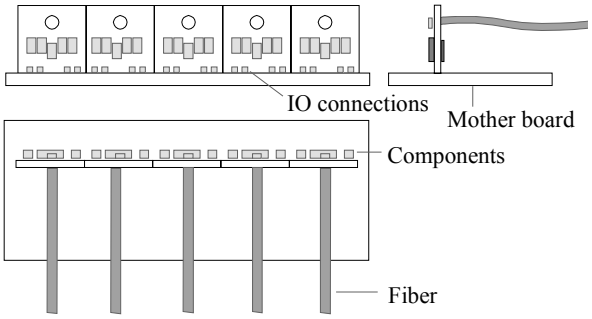

Figure 1. Mechanical structure of the pigtailed 5-channel transmitter mounted on a motherboard.

The fiber alignment structure was based on 4 tape layers (Fig. 2). The hole through the top three layers is used for the fiber alignment and support; thus it serves as a fiber ferrule. The slightly smaller hole through the bottom layer acts as a stopper for the fiber preventing the fiber to hit the light source. VCSEL is flip-chipped at the bottom of the substrate using stud bumps (and wire bonded if necessary). The fiber is assembled from the topside and can be fixed using adhesives and supported on the LTCC substrate by a plastic strain relief boot.

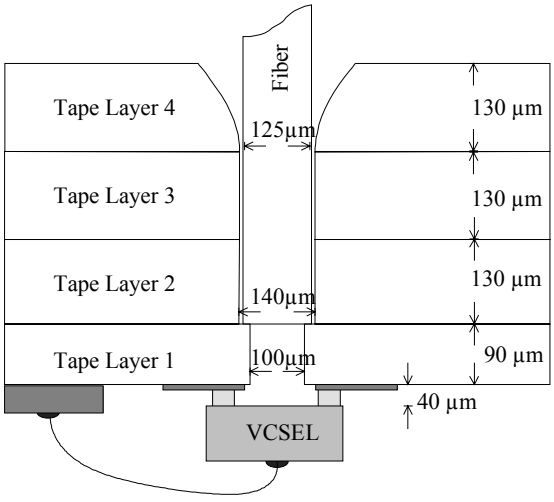

Figure 2. LTCC structure for the fiber alignment. Dimensions are of the 1st prototypes.

To demonstrate the required transversal alignment tolerances, the coupling of a VCSEL beam into a 62.5/125-µm GI multimode fiber was examined by measurements and simulations. The simulations

were made with measured VCSEL characteristics using ray-tracing software called ASAP. Two types of VCSELs emitting at around 840 nm were used: Mitel 1A444 (without lens) having FWHM beam divergence of 12° and Gigalase 8085-1100 (15-µm aperture) by Emcore. The latter had beam divergence of 16° and was also used in the realized transmitters. For Mitel's VCSEL at 140-µm separation and Emcore's VCSEL at 115-µm separation (Fig. 3), simulations showed at least 90 % coupling efficiency with less than ±15 µm transversal misalignment. For Emcore's VCSEL at 140-µm separation the corresponding tolerance was ±10 µm. However, smaller than 3dB loss was attained with ~±30 µm tolerances in all cases. Measurements with Mitel's VCSEL also verified the results with a good match.

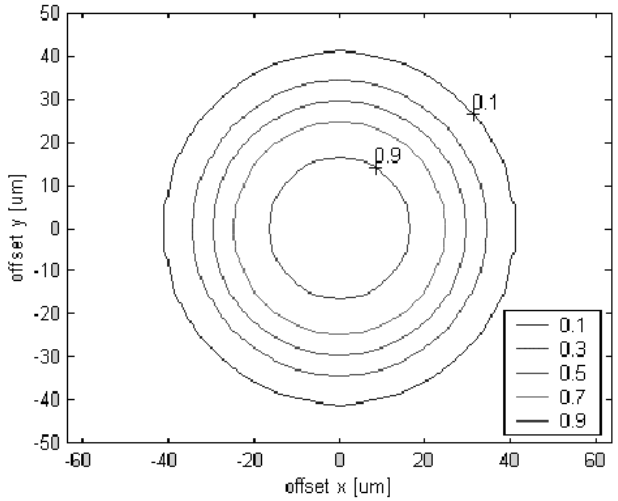

Figure 3. Simulated coupling efficiency as a function of the transversal misalignment of fiber and Emcore's VCSEL at 115-µm separation.

LTCC AND ALIGNMENT TOLERANCES

LTCC is not regarded as the manufacturing technology offering the highest dimensional accuracy. This is mainly due to the shrinkage of typically 10...13 % during the firing operation. In volume production, the dimensional tolerances are typically 0.2 %. However, in this application, the important issues are the shape and dimensional tolerances of the through holes used for the fiber alignment.

At first, some LTCC test substrates were prepared to characterize the through holes for the fiber assembly as well as to test fiber alignment methods. It was demonstrated that various hole diameters are possible by tool change and the holes are fine-tunable with process parameters, and that the tolerances in hole dimensions are small enough for the multimode fiber alignment. It was also possible to make a tapered hole by pressing with a needle to ease the fiber assembly, but the tapering was not needed in the realized modules thanks to the clearance of the holes.

To study the capability of the LTCC technology and the feasibility of the designed structures, 5-channel transmitter modules were realized. The lamination parameters for the LTCC parts were: 2400 psi, 70 °C, 10 min. A 50-µm steel foil was used on the topside during lamination to prevent the possible deformation of the fiber holes. The firing was made with the standard 875 °C profile, typically used for the DuPont 951 tape. In the 1st prototypes, severe difficulties were met with the bottom tape layer dimensional instability compared to the other layers during the conductor printing steps. This was because the bottom tape layer was thinner than the others were and caused alignment problems. Therefore, similar sheet thicknesses (130 µm) were used in the 2nd transmitter modules. A slight drawback was the increased VCSEL-to-fiber separation. In addition, a 10-µm smaller punch tool was used for the alignment holes to reduce the fiber misalignment due to the hole clearance.

Table 1. The used punch tools and resulted hole diameters in the transmitter module substrates.

Module	Layer	Punch tool	Hole diameter
1st & 2nd	1	150 µm	105 ± 6 µm
1st	2…4	200 µm	145 ± 6 µm
2nd	2…4	190 µm	135 ± 6 µm

MODULE REALIZATION

The prototype modules were made using Emcore's VCSEL chips and 62.5/125-µm fibers. Each transmitter, sized 5×5 mm^2, included discrete passives, differential PECL inputs and a laser-driver chip with 1.25 Gbps bandwidth. The driver, VCSEL and capacitors were on the bottom side of the substrate, whereas the resistors and I/O-pads were on the topside. VCSELs were assembled with a flip-chip bonder by visually adjusting the emitting area with the alignment hole. The estimated accuracy was ±10 µm though the maximum accuracy of the bonder is ±5 µm.

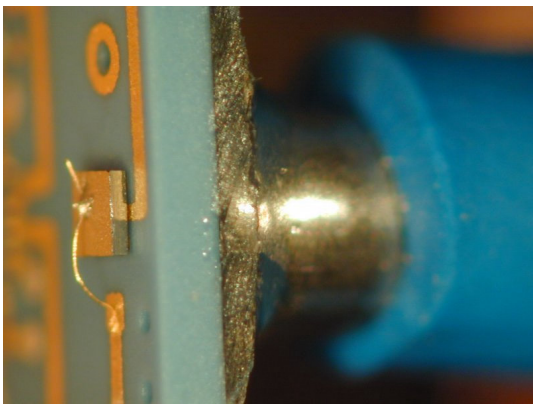

Figure 4. Attachment of the fiber and VCSEL.

The fibers were assembled manually by placing the LTCC substrate onto a moving xy-stage and the fiber onto a z-direction-moving mount. The fibers were stripped and cleaved but not polished because the quality of cleaved fiber facet is reasonably good. The fiber was visually aligned with the hole and then dropped to the hole and glued using an UV-curable adhesive. In large-volume production, however, automated fiber assembly is also possible. Metallic tubes (glued to the substrate and fiber) were used as strain relief boots. Additionally, a (blue) shrink-tube was used as a cable support. Finally, the substrate was mounted vertically onto a prepared test board and fixed with adhesives.

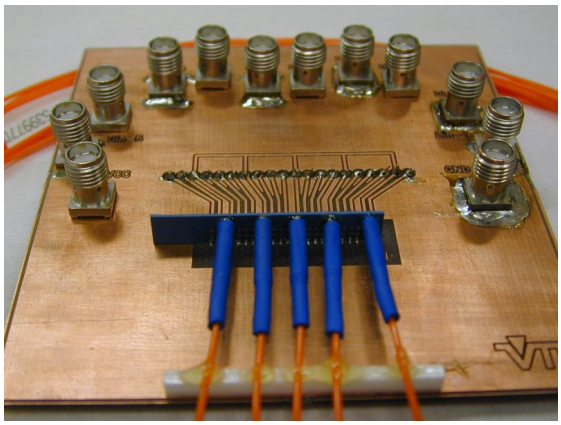

Figure 5. Pigtailed transmitter-array module on the test board.

In the first transmitter prototypes, the total alignment tolerance was estimated to be ±26 µm. According to the simulations this means better than 70 % optical coupling efficiency. However, with the smaller punch tool used in the 2nd prototypes and better control of the flip-chip bonding, ~10 µm smaller tolerances should be achievable. The worst case fiber misalignment was found out to be ±10 µm. The preliminary measurements also revealed reasonably good coupling efficiency for all emitters.

Table 2. Transversal misalignments of the VCSEL-to-fiber coupling in the prototypes.

Fiber hole clearance	± 5…10 µm
Fiber hole diameter	± 6 µm
VCSEL alignment	± (5…)10 µm
Total tolerance	± (16…)26 µm

CONCLUSIONS

It was demonstrated that, thanks to ~±20 µm total alignment tolerances, LTCC is a potential technology for low-cost, small-sized, high-bit-rate optoelectronic modules, featuring passive alignment of optical fibers to surface-emitting devices. The developed, new transmitter-array structure can be used as a small-footprint, detachable interface between the electrical and optical media. Nevertheless, stringent process control is necessary in order to obtain the required accuracy. There are also many unsolved issues considering the mass-production.

REFERENCES

1. Karioja, P. *et al.*, "Comparison of Active and Passive Fiber Alignment Techniques for Multimode Laser Pigtailing," Proceedings of 50th Electronic Components and Technology Conference, Las Vegas, USA, May 21–24 2000, pp. 244–249.
2. Karppinen, M. *et al.*, "Passively aligned fiber-optic transmitter integrated into LTCC module," Micro- and Nano-optics for Optical Interconnection and Information Processing, San Diego, USA, July 29–Aug 3 2001, Proc. SPIE, v. 4455, pp. 293-302.

LTCC Technology for MEMS Packaging

Harri Kopola, Jaakko Lenkkeri, Kari Kautio, Altti Torkkeli, Outi Rusanen* ,Tuomo Jaakola
(*Affiliation: Nokia Mobile Phones, Oulu)

INTRODUCTION

Packaging issues are very important and challenging for the applicability of micro electromechanical systems (MEMS). The successful packaging of MEMS components can seldom exploit the traditional IC packaging practices, due to the special requirements for packaging these components. The components are usually sensitive to mechanical or thermo-mechanical stresses and often there are restrictions or special demands for the connection with the ambient surroundings (pressure or gas sensors).

The actual packaging concept and the size of the construction depend on the selection of the components needed for the system. If the system includes several components, the most promising packaging concept is the SOP (system on package) concept which utilises modern high density circuit boards together with small size active components i.e. bare dies or CSP components.

A potential substrate technology for the SOP is LTCC (Low Temperature Cofired Ceramics), which has many benefits for packaging silicon based MEMS components [1,2]. Firstly, it is possible to make cavities in the substrate, in which the components can be bonded and hermetically sealed, if required. Secondly, the match between the linear coefficient of the thermal expansion (CTE) of ceramics and Si is fairly good (2.6 ppm/^{o}C vs. 5 to 7 ppm/^{o}C for LTCC), which is of great importance for sensitive MEMS pressure sensors. In Figure 1 the SOP packaging concept using multilayer LTCC substrate materials is illustrated.

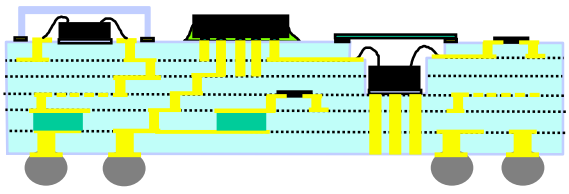

Figure 1. SOP packaging concept using multilayer LTCC substrate.

PACKAGING OF MEMS MICROPHONE

Silicon microphones have been under development since the early 1980s but they are not yet commercially available. VTT Electronics has manufactured a capacitive microphone with polysilicon membranes (Figure 2) [3].

For optimal operation of the microphone, the tensile stress and thickness of the bending membrane should be as small as possible. This places special demands on the package, because the microphone must operate at a wide temperature range and very small external stresses may lead to membrane buckling.

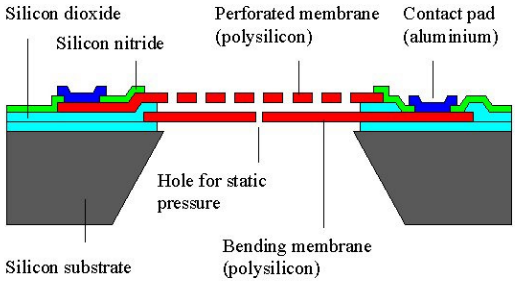

Figure 2. Cross section of the microphone chip [4].

The integration of the silicon microphone into the LTCC package together with an ASIC chip is currently under development at VTT. The component should be such that it can be soldered onto a printed circuit board in a standard reflow soldering process. The temperatures used in reflow are too high for the electrete microphones currently used in consumer products. However, silicon microphone easily withstands such temperatures, but the package must be carefully selected. LTCC is a good choice because of thermal expansion coefficient close to silicon.

LTCC process opens also possibilities for arranging cavities and holes that are essential in microphone operation. Another important feature of LTCC is the integration of readout electronics into the same package. This holds true for all capacitive micromechanical components. Capacitive readout suffers from instable stray capacitances, and in order to minimize their

contribution the readout electronics must be placed in the close vicinity of the sensor. Also the surrounding materials must be electrically low-loss and stable such as in LTCC substrates.

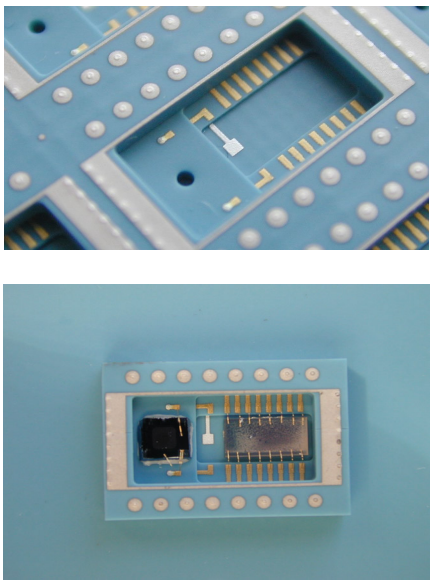

Figure 3. Prototypes of LTCC packaging of silicon microphone.

FUTURE POTENTIAL OF LTCC FOR MEMS PACKAGING

The combination of silicon based MEMS technology and LTCC multilayer ceramic technology has many potential benefits for smart sensor applications. LTCC substrate offers multilayer circuitry between components, high density pad layouts for flip chip and CSP components as well as I/O connections for the component itself. The possibility of integrating various passive components into the substrate can be of great importance.

There is also the possibility to fabricate various MEMS structures onto or into the LTCC substrate itself. Cavities, openings and tubes can be made for connecting liquid or gaseous substances. Heating elements made onto LTCC could be used for producing small dimensional changes in the structure. Cavities can also be used for sealing components. A lid can be joined onto the cavity e.g. using a brazing procedure with Au-Sn solder material. Kovar metal lids, as well as glass or sapphire windows with Au-metallization on the joint area have been used successfully for making hermetic sealing of cavities in LTCC substrate. The ability to use window structures makes it possible to utilize various optoelectronic components or sensor elements in the sensor modules.

LTCC substrates are also very potential substrates for optical waveguides. The high frequency properties of the LTCC substrates are also excellent because of the good dielectrical properties of the laminates and very high conductivity of the metallizations used. This means that LTCC technology has great potential in technology for wireless high frequency applications where MEMS components are used to increase system functionality . The possibility of applying wafer-level joining technologies such as anodic bonding for joining silicon wafers directly onto LTCC opens new possibilities for MEMS sensor manufacturing.

The technology offers the following possibilities:

- in MEMS applications part of the MEMS function could be maintained in the LTCC carrier
- for biological and chemical sensor chips the LTCC carrier can provide gas or liquid interface to the sensor chip
- full electrical connection to any point of the chip is possible
- the LTCC carrier gives full mechanical and electrical interposer capability to PCBs.

REFERENCES

1. Kopola, H, Lenkkeri, J., Kautio, K., Torkkeli, A., Rusanen, O., & Jaakola, T., MEMS Sensor Packaging using LTCC Technology, *Proc. of MICRO/MEMS 2001*, December 2001, Adelaide, Australia.
2. Kopola, H., Blomberg, M., Karioja, P., Kautio, K., Rantala, J. T.& Rusanen, O. “System Integration and Customized Packaging of MOEMS,” *Proc. of 3rd Int. Conf. on Micro Opto Electro Mechanical Systems*, Mainz, Germany, August 30 - September 1. Pp. 194 – 205, 1999.
3. Torkkeli, H. Sipola, H. Seppä, J. Saarilahti, O. Rusanen, & J. Hietanen, "Capacitive Microphone with Low-stress Polysilicon Membrane and High-stress Polysilicon Backplate", *Proc. of EUROSENSORS XIII (The 13th European Conf. on Solid-State)*, September 12-15, 1999, Hague, Netherlands.
4. Torkkeli, J. Saarilahti, H. Seppä, H. Sipola, O. Rusanen, & J. Hietanen, "Capacitive Silicon Microphone", *Physica Scripta, T79*, pp. 275-279, 1999.

Halogen free laminates in electronics manufacturing

Liisa Kivimäki

INTRODUCTION

The European Commission/ Parliament have drafted two proposals, WEEE and RoHS Directive, a directive on the limitation of waste from electrical and electronic equipment, and a directive on the limitation of hazardous substances in electrical and electronic equipment, respectively. The main objectives of the two proposed directives are to protect the environment and human health from pollution caused by waste from electrical and electronic equipment, to prevent disposal of this kind of waste by landfill and to reduce the harmfulness of such waste. By 1 January 2007 at the latest, Member States of EU shall ensure that new electrical and electronic equipment put on the market does not contain lead, mercury, cadmium, hexavalent chromium, polybrominated biphenyls (PBB) and/or polybrominated diphenyl ether (PBDE).

Printed circuit board laminates contain fire or flame retardants, which previously were for example PBB or PBDE as mentioned above. Polybrominated flame retardants can produce very poisonous dioxines if the burning is incomplete. Nowadays the main flame retardant used in electronics manufacturing is tetrabromobisphenol-A, which is not included in the compounds banned in the directive.

PURPOSE OF THE STUDY AND TEST ARRANGEMENTS

The purpose of the study was to test halogen free laminates, their compatibility with other printed circuit board/ component board materials in soldering and to compare results with brominated laminates.

The laminates used were single sided CEM-1 and CEM-3, double sided CEM-3 and FR-4, and multilayered FR-4. Altogether, ten series were evaluated including six laminate manufacturers. The manufacturers were Isola, Hitachi, Von Roll Isola, Matsushita, Nelco and AIK.

Test boards were reflow- and wave soldered with SnPb solder.

SOLDERING TEST RESULTS

Halogen containing and halogen free component boards were compared with each other by their mechanical behavior. The quality of soldering was evaluated by considering defects resulting from process conditions. That was done by visually examining soldered component boards and comparing solder defects in different series with each other. The wetting of organic preservative (OSP) plated through holes was observed by checking the filling of the holes. Bow and twist behavior of single sided boards was measured.

Test structures on halogen free as well as on halogenated laminates soldered well. The amount of solder bridges detected on halogen free laminates was less than on halogenated boards. Only minor flux residues were seen on all soldered boards.

Filling of the through holes plated with OSP was incomplete among all the tested series.

Bending of single sided boards during wave soldering was within the acceptable limits.

RELIABILITY TESTING

The adhesion of copper conductors on the laminates was defined by measuring the peel strength. Through hole reliability was determined with temperature cycling test and temperature shock test. The long- term reliability of the soldered boards was evaluated with a temperature cycling test and an accelerated life test.

The peel strength of conductors on multilayer boards was for some reason much higher than on other laminates. All conductors measured were attached to laminates strong enough after printed circuit fabrication but also after temperature shock test (288°C, 10s).

One halogen free laminate was superior over other tested laminates in withstanding sudden temperature rise among through holes (T=260°C, 4 seconds, cycling). All tested halogen free laminates were more heat-resistant than halogenated laminates. In general, the failure

occurred between the through hole and the collar as seen in Figure 1.

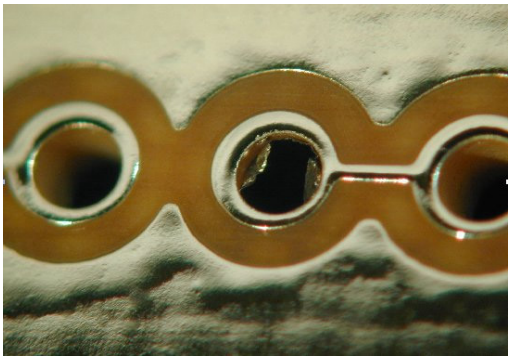

Figure 1. Copper detached from the hole during temperature shock test.

All through holes passed the temperature cycling test (800 cycles 0°C to 100°C). At the same time solder joints of through hole capacitors had no failure either, according to impedance measurements.

The accelerated life test (85°C/85%RH, +15 V, 500 hours) revealed that one CEM-3 laminate was not of uniform quality. All its test structures had lower surface resistances than that of other series during the whole 85/85-test. Those resistances also stayed low after the test; migration was not noticed between the conductors. All laminates except that one passed 100 Mohm surface resistance at 165 hours (IPC-SF-818). Very few migrations were detected from any test series after the test.

CONCLUSIONS

According the tests, the halogen free laminates evaluated, except one, are useful in electronics manufacturing and are suitable for reflow and wave soldering processes.

Distance measuring sensor using CMOS detector and LTCC technology

Veli Heikkinen, Mikko Heikkinen, Risto Mitikka, and Veli-Pekka Putila

INTRODUCTION

The development of optoelectronic modules and instruments is a multi-phased process that requires knowledge from many technical disciplines. Because it is difficult for one individual to master all these fields, usually a number of specialists participate in the design project. Every person should sufficiently understand other domains besides his own expertise area, so that the design process will be successful. Additionally, because almost all design is carried out using specialised software, its electronic compatibility has become very important, as this ensures fast and faultless data transfer.

The objective of our previous work was to develop a communication network that would enable us to exchange information between various commercial optical, electrical and mechanical design software.[1] The operation of this data network has now been tested by the design and realisation of the CMOS camera prototype that is equipped with the range finding feature.

MODULE DESIGN AND REALISATION

The laser range finder sensor has two modes of operation. In the passive mode, it monitors the environment using CMOS detector electronics and ambient light. When working in the active state and applying the light source it can also measure distance profiles of targets in one-dimension. Then the transmitter produces a thin light stripe onto the measurable object, and the receiver captures the image and calculates distances using triangulation principle, Figure 1.

A vertical cavity surface-emitting laser (VCSEL) is used as the near-infrared light source. Its output beam is first collimated by a single element aspheric lens, and then transformed into a stripe using a diffractive optics element (DOE). When the laser-to-detector axis is parallel with the horizontal plane, the illumination line has divergence angles of 0.3° in horizontal (H) and 20° in vertical (V) directions.

The transmitter electronics controls laser's drive current and pulse width. Adjusting the laser's optical power according to the distance and reflectivity of the object can extend the system's dynamic range. The drive current can be adjusted from 7 to 70 mA.

The receiver optics consists of a micro-video imaging lens that focuses light reflected from the object onto the detector surface. The receiver optics has a field-of-view of 60° (H) and 44° (V). The monochrome CMOS matrix sensor conforms to VGA resolution and contains 640 (H) · 480 (V) pixels, each having an active area of 7.9 · 7.9 μm^2.

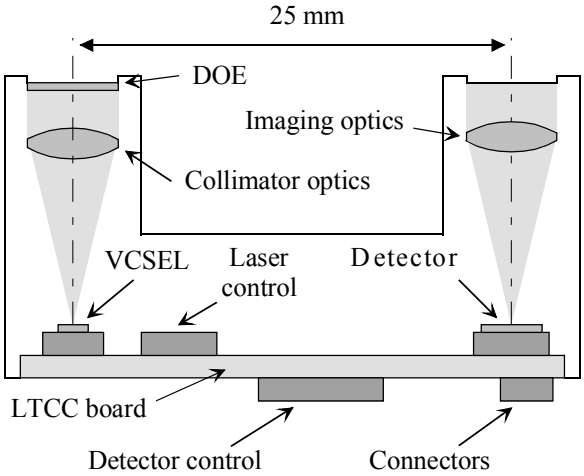

Figure 1. Schematic structure of the distance measuring sensor.

The receiver electronics is based on the evaluation board of the detector manufacturer, and it generates all control signals for the sensor. Moreover it controls the data transfer between the module and the computer, which are connected together via a serial I^2C bus for control signals and an 8 bit parallel bus for image data transfer. The power supply is 5 V/300 mA. Sensor electronics were realised using VTT Electronics' LTCC (Low

Temperature Co-fired Ceramics) process, Figure 2.

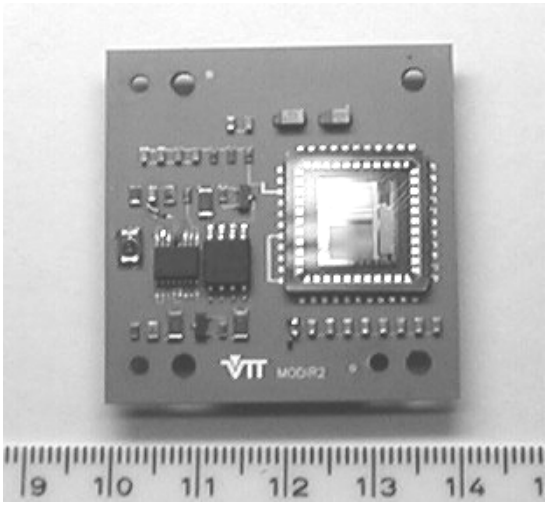

Figure 2. Upper side of the LTCC board.

The outlining of the module mechanics was started using the optics and electronics design data, which were transferred into the 3D design software (I-DEAS). The main challenge for the optomechanics design was to align the transmitter and receiver optics with the laser and detector that were soldered to the LTCC board.

Optical element data were exported from the optical design software (Zemax) to the mechanics design using IGES format (Initial Graphics Exchange Specification). Because these files contained only the lens surface characteristics, we had to model their mechanical mounts using manufacturers' catalogue data. The 3D model of the upper side of the LTCC board with optics is shown in Figure 3.

The module housing was manufactured from AlMgSi alloy, using electronic data transfer via the process planning software (MasterCAM) to the five-axis milling work station (Bridgeport VMC 800 with Heidenhain 410 control). This aluminium alloy has excellent free cutting properties and is lightweight. Anodization made the surfaces harder and enhanced their abrasion resistance, Figure 4.

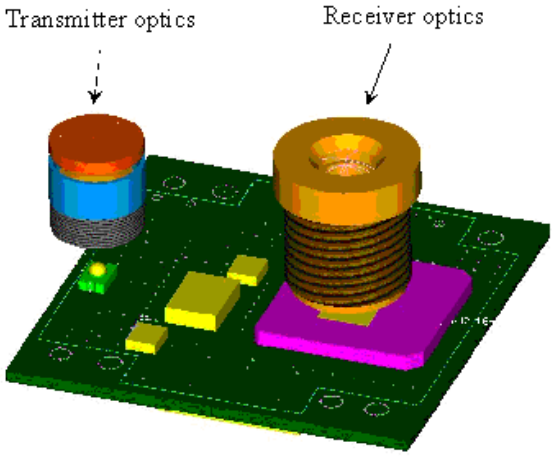

Figure 3. 3D model of the upper side of the LTCC board.

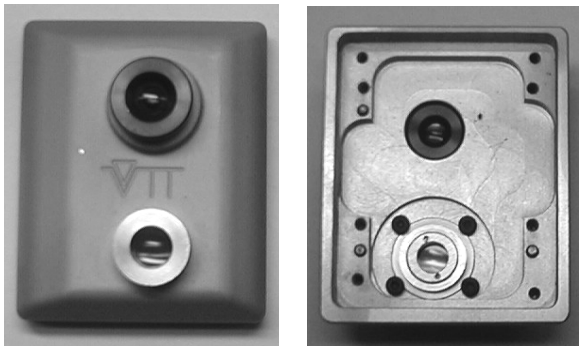

Figure 4. Top of the sensor housing.

CALIBRATION AND TESTING

The image quality and distance measurement accuracy of the sensor prototype was evaluated in laboratory conditions. Some triangulation sensors, especially those using one light spot, employ mathematical modelling for the distance calculations. However, the imaging lens of our sensor had quite severe barrel distortion. Therefore mathematical formulas for distance calculations were discarded and a lookup table calibration was applied instead.

Calculating a weighted centroid of the pixel values of each image row that were larger than the threshold, Figure 5, enhanced the distance measurement accuracy. This is essential for maintaining the measurement accuracy across a long range. For example, when the target changes from 80 cm to 200 cm, the image of the laser stripe moves only 10 pixels. The centroid method also improves the accuracy in short ranges where the stripe's image can be saturated and widened. The position of the stripe image in

one of the detector rows vs. the target distance is shown in Figure 6.

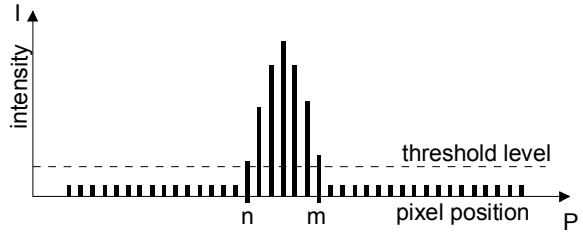

Figure 5. Pixel values in one detector row.

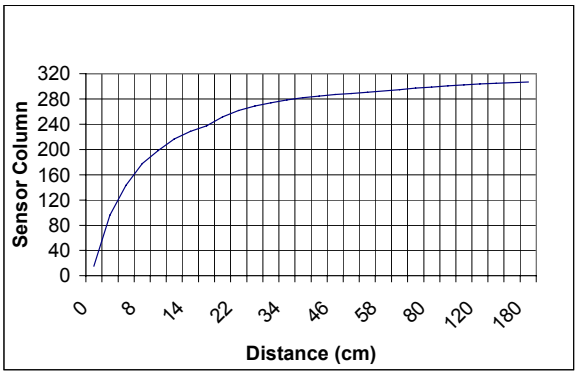

Figure 6. Laser stripe position vs. the distance.

An example of the distance profile measurement presented using the graphical overlay is shown in Figure 7. Here the corner of the cardboard box was used as the target. The centroid of the laser stripe is illustrated with red colour.

The test results showed that the image quality of the prototype enables us to distinguish features having dimensions in the order of 1 mm at 20-cm distance. The distance profiles of targets can simultaneously be obtained from 100 points with accuracy (standard deviation) varying from 0.1 mm at 5-cm distance to 2 cm at 1.5-m range.

REFERENCES

1 V. Heikkinen, K. Keränen, V-P. Putila, and K. Tukkiniemi, "Integrated system for module design and realisation", *Research Activities in Optoelectronics and Electronics Manufacturing 2000*, VTT Electronics, Oulu, p. 11 - 12, (2001).

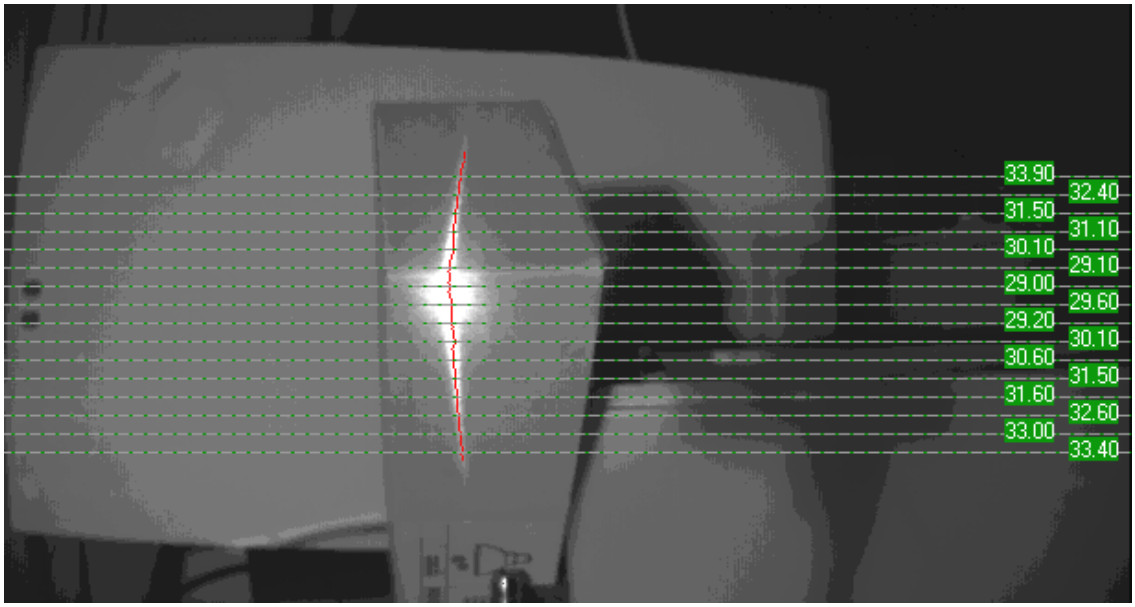

Figure 7. A distance measurement presented using the graphics overlay.

SPECTROSCOPIC INSTRUMENTATION

Design and manufacturing method for IR analyzers based on mirror optics

Mauri Aikio, Pekka Suopajärvi, Jussi Tenhunen, Ahti Haapalainen, Tomi Seppänen, Ilkka Alasaarela, Hannu Vasama*, Markku Mäntylä**
(*Suomen Optomekaniikka Oy, ** Metso Paper Automation Oy)

ADVANTAGES OF MIRROR OPTICS IN IR ANALYZERS

Near and middle infrared analyzers are used widely in many fields of industry, for example to measure water content of paper or lubricant film thickness on metal surface. Typically IR analyzers contain non-imaging optics.

Mirror optics have many advantages in IR analyzers. Because a mirror is free from chromatic aberration, it can be used over a wide wavelength range and thereby IR mirror optics can be adjusted using visible wavelengths. In non-imaging cases, mirrors with large numerical aperture can work better than lenses. Also mirror optics can be folded into a smaller volume than a comparable lens system. In addition mirrors are often cheaper than IR lenses.

PRINCIPLE OF OPTOMECHANICAL CONSTRUCTION FOR IR ANALYZERS

A mirror surface is manufactured into a mechanical part with an accurate 5-axis CNC machining center, without losing the work piece during the process, see Figure 1. The analyzer housing is manufactured in the same way. The positioning accuracy of a mirror is the same as the accuracy of the mechanical part. No adjustments to the optical components are needed.

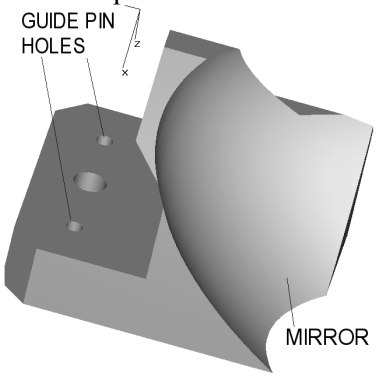

Figure 1. A mirror surface is manufactured into a mechanical part with guide pinholes and positioning surfaces. A 3D model of the part.

DESIGN AND MANUFACTURING METHOD

VTT Electronics has developed the 3D design and CAM manufacturing process for IR analyzers shown in Figure 2. At first the optics are designed. After mechanical design the 3D model of an analyzer can be simulated and checked again in the optical design software. Then 3D models of the parts are transferred into CAM manufacturing process in VTT Electronics. Mirror surfaces are polished and coated with reflective film and the analyzer can be assembled. This method is fast. From the design phase to the finished mirror can even take only several hours.

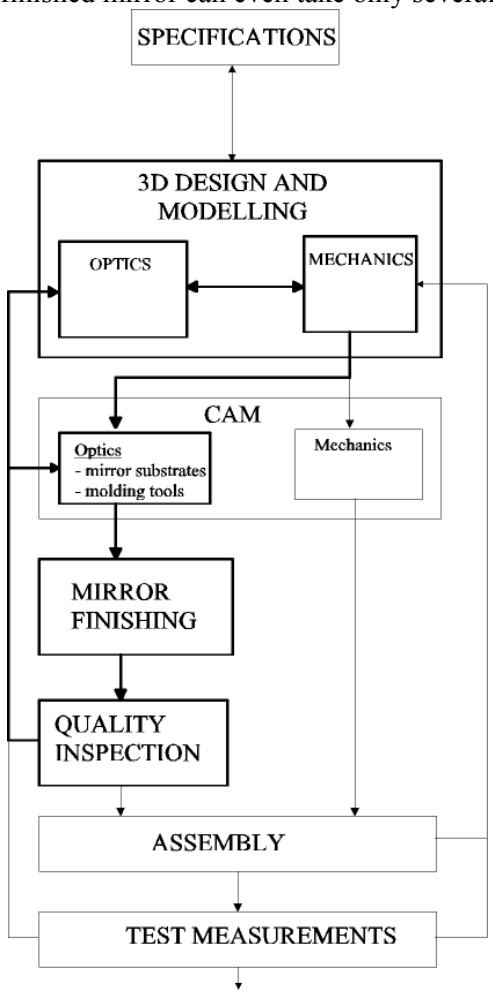

Figure 2. Design and manufacturing method for IR analyzers.

SIMPLE EXAMPLE

A measuring probe optics is taken here as an example to demonstrate the efficiency of the mirror optics. The principle of a conventional lens construction of the probe is shown in Figure 3. The illumination light is collimated by a spherical lens. The illuminated area is formed so as to be elliptical, by a cylindrical lens making the illumination large enough for the collection optics, when the measuring object is moving up and down. The collection optics consists of a cylindrical and spherical lens. Light with a wide wavelength range is transferred to a spectrograph through the collection fiber. The probe optics is sealed in a housing with pressure ventilation. The amount of mechanical parts and adjustment work for this construction are not estimated.

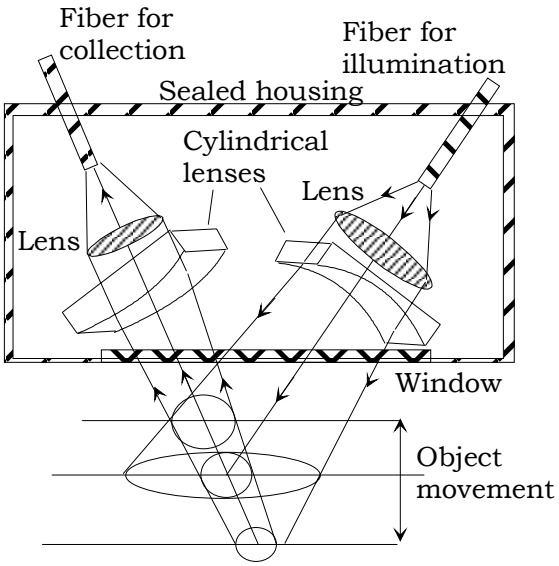

Figure 3. The principles of an IR probe optics with a conventional lens system.

A comparable, realized probe optics with two mirror surfaces is shown in Figures 4 and 5. The housing, mirror surfaces and fiber holders are made of a single piece of hard aluminum block. It is manufactured using the 5-axis CNC machining center in VTT Electronics. No adjustments to the optics are needed.

The first developed analyzer based on this mirror technology measuring coat weight of paper was introduced at the end of May 2001. It consisted of 13 mirrors and only the detectors needed to be adjusted, because of the positioning tolerances of the detector element in the can.

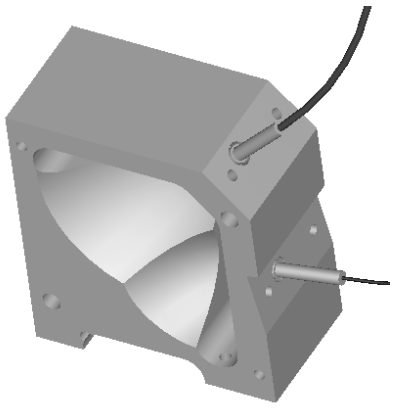

Figure 4. A comparable probe optics with two mirror surfaces and holders for the fibers, made of a single block of aluminum.

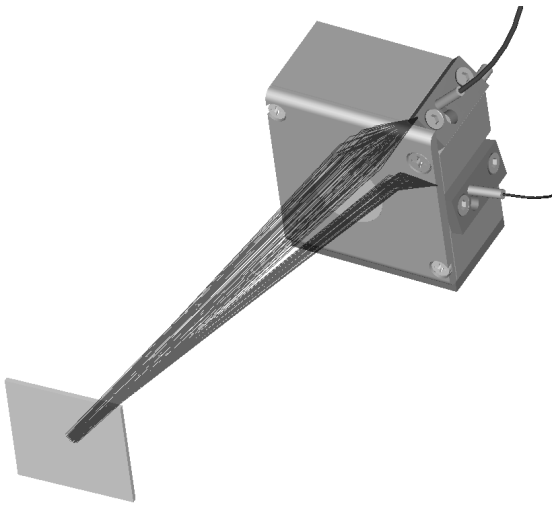

Figure 5. Raytracing the probe with window and sealing.

CONCLUSION

Mirror optics has many advantages in IR analyzers used widely in industry. VTT has developed design and manufacturing processes for IR analyzers based on mirrors. The mirror constructions tend to be compact, simple and no adjustments to the optical components are needed.

The first developed analyzer based on this mirror technology was launched on the market at the end of May 2001.

Optical instrument for online coat weight measurement

Jussi Tenhunen, Mauri Aikio, Ahti Haapalainen, Markku Mäntylä*, Antti Paavola*, Pauli Paukkunen**,
Tomi Seppänen, Pekka Suopajärvi, Hannu Vasama***
* Metso Paper Automation, Tampere, Finland,
** Finnelpro, Tampere, Finland
*** Suomen Optomekaniikka, Jyväskylä, Finland

In this article, we describe the design process of Metso Automation's "IQMultiCoat" optical coat weight measurement instrument and the results obtained with the instrument.

BACKGROUND

The online measurement instruments that are used to control the paper basis weight, moisture, caliper (thickness) and CW are located in the scanner, which moves in the measurement frame (Figure 1).

Figure 1. Measurement frame. The instruments are located in the moving scanner at the center of the frame. Paper moves through the frame between the upper and lower scanner heads. The arrows indicate the direction of the scanning (orthogonal with respect the movement of the produced paper). (Courtesy of Metso).

The coating thickness or coat weight (CW), measured in g/m^2, and ranging typically from few g/m^2 to few tens of g/m^2, is an important parameter in the production of coated paper and board in terms of the quality of the printed paper and in ensuring that the coating machine and the printing machine function properly. Thus, the applied CW profile is measured and in closed loop control over the cross direction (CD) of the paper web.

The main pigments of the coating are clay (Al_2O_3*2SiO_2*2H2O), and calcium carbonate $CaCO_3$). The most common binders are SB-, Acryl- or PVAC-latex.

The online CW measurement is traditionally based on oven dry weight (OD) method. With this method, four measurements are needed to calculate the CW: The total weight (by β-absorption method) and moisture (transmissive IR method), both before and after the coater.

There are few problems associated with the online OD method.

1. Especially in the case of heavy grades (basis weight can be up to 300 g/m^2.) even small relative error in calculated OD difference, rising from the errors in measured moisture, β-absorption measurements or in the synchronization of the four measurements, can result in noticeable error (or noise) in the calculated CW
2. The four measurements needed for OD demand expensive space in the paper machine.
3. Being a transmission measurement, the β-absorption can only be used in applications which allow instrumentation to be placed below and above the paper web and it cannot be used in applications where the paper is coated on both sides simultaneously.
4. As a radioactive method, β-absorption is not user friendly.

OPTICAL CW MEASUREMENT

Optical CW measurement, based on diffuse IR reflection, avoids the difficulties mentioned above. The principle of the measurement is given in Figure 2.

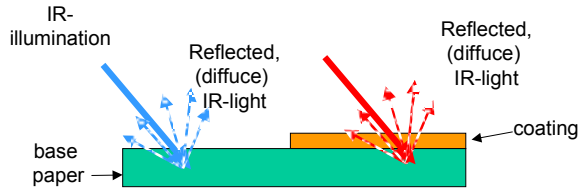

Figure 2. Principle of the CW measurement based on diffuse reflectance. (Courtesy of Metso)

The incident infrared radiation is mainly transmitted through the coating, diffusely reflected from the base paper and transmitted

back through the coating to the free space, where part of it is collected at the detector. Thus, the measured reflectance can be approximated as a diffuse reflection spectrum of the base paper, multiplied with the transmission spectrum of the coating. At the absorption wavelength of the coating pigments, and at the absorption wavelength λ of the coating pigments, the detected reflectivity obeys the Lambert-Beer law i.e. reflectivity R is proportional to exp (-α(λ)*CW*P/100) where α(λ) is the absorption coefficient of the coating pigment and P is the (weight) percentage of the measured coating pigment (marker) of the total coating. Thus CW can be calibrated for the measured reflectivity. In practice, other wavelengths are needed to compensate for the effects of varying moisture, measurement distance, etc. As an example, the diffuse reflectance spectra of the base paper and the coated paper are shown in Figure 3. The resolved absorption bands of the coating components are located between 2400 and 5500 1/cm or 1.8 - 4.2 um.

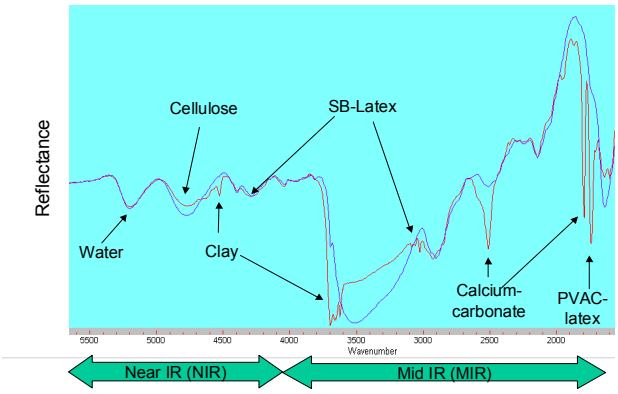

Figure 3. Reflectance spectra of the base paper (blue) and coated paper (red). The absorption bands of the main component are indicated by arrows.. (Courtesy of Metso)

REQUIREMENTS

The requirements for the measurement are given in Table 1.

Table 1. Measurement requirements

Simultaneous measurement of $CaCO_3$, clay weight binder weight [g/m^2] and moisture [%].
Excellent measurement accuracy and repeatability (0.2 and 0.15 g/m^2 respectively)
Profile resolution 10 mm (with typical scan speed this leads to 20 ms time constant)
Small physical size (approx. 240 x 300 x 125 mm) including mechanics, electronics, optics and thermal stabilization.
Immunity to : measurement distance variation [0-50 mm], dirt buildup tendency of environment, high air moisture (up to 95 % RH), changes of environment temperature (15- 85 C)
Long lifetime. Economical production cost. Easy service.

DESIGN

The design of the instrument based on the requirements listed in Table 1. At first, the most potential instrument types were evaluated. The conclusion was that the constraints given in Table 1 couldn't possibly be made to meet with traditional constructions. As an optimal solution, a novel filter wheel instrument was designed (Figure 4). This concept provides 8 NIR channels, 8 MIR channels, and highlight throughput. The electronics block diagram is also presented in Figure 4. Extensive use of digital electronics provides stable, fast and flexible signal processing, full control and on-line diagnosis. Ethernet and RS-485 buses are used for fast IO between the instrument and the process computer. The internal temperature is controlled from six positions for diagnostic purposes.

The optimal spectral bands for the filters with respect to the requirements of Table 1 were found with computer simulations using FTIR spectral data, measured from a representative sample set of coated papers and boards.

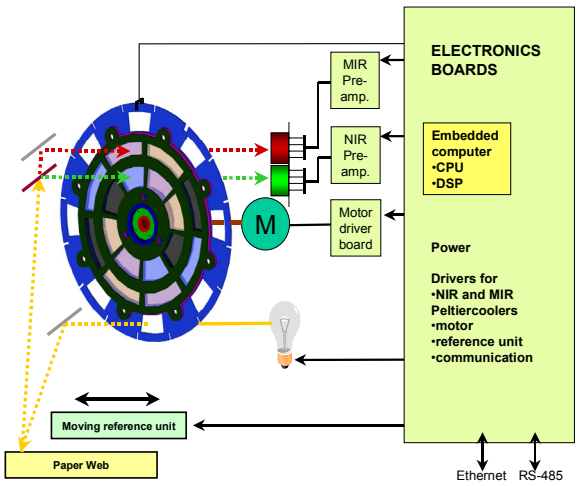

Figure 4. The principle of the optics and the electronics block diagram. The chopper, 8 NIR and 8 MIR filters are placed in the same rotating wheel. The chopper, located between the source and the paper web, eliminates the ambient light and IR emission from the hot web. The moving reference unit is used to compensate for dirt, the aging of the source and long term changes in detector responsiveness. (Courtesy of Metso).

Instead of lens optics, low F-number aspheric metal mirrors were used (Figure 5). This approach avoids the need for expensive AR coated lenses made from special IR materials (CaF_2, Sapphire, ZnSe etc.) and the chromatic aberration. Furthermore, this leads to a small physical size and a high optical throughput, which is needed to reach high signal to noise ratio (SNR). Optical and mechanical designs were included in the same 3D CAD design method, and sophisticated NC methods were used in the machining of the components. The body of the optics was machined from a single solid aluminum block, in which all the optical components are precisely positioned using pins. Because the design and manufacturing method leads to a high positioning accuracy, there is no opportunity nor any need to align the components. This approach ensured good thermal stability, similarity of the produced instruments, as well as providing good calibration transfer between the instruments and immunity to temperature changes and mechanical vibration. The resulting optomechanics is schematically presented in Figure 5.

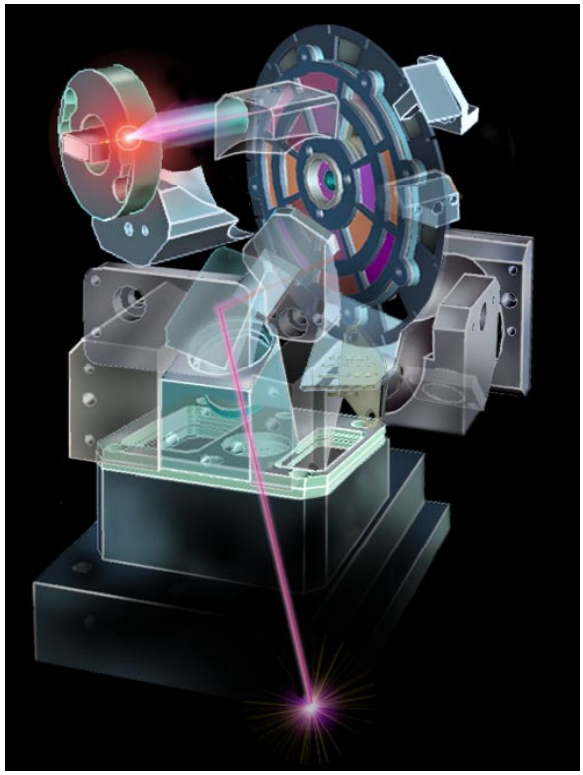

Figure 5. Schematic picture of the optomechanics. (Courtesy of Metso)

The realized instrument is schematically presented in Figure 6.

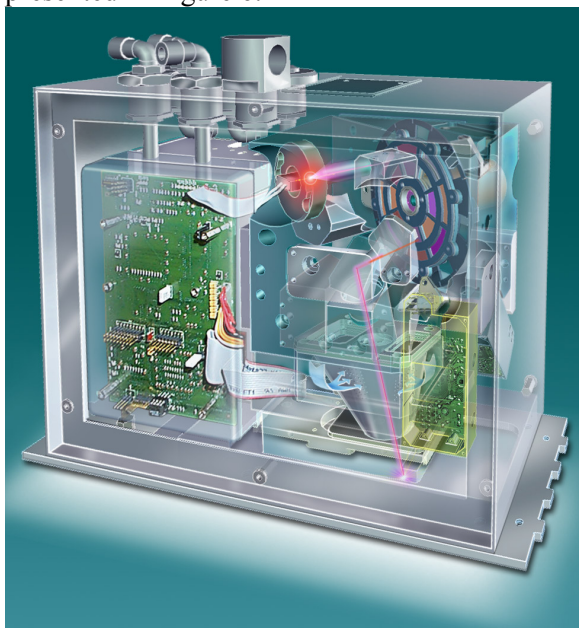

Figure 6. Schematic view of the instrument

PERFORMANCE

In Figure 7, the obtained detector signal is presented as an example of the combination of a short time constant and high SNR. Typically the SNRs are above 1500 and 300 for the NIR and MIR signals respectively, when measured from paper at 20 mm measurement distance and using 20 ms integration time.

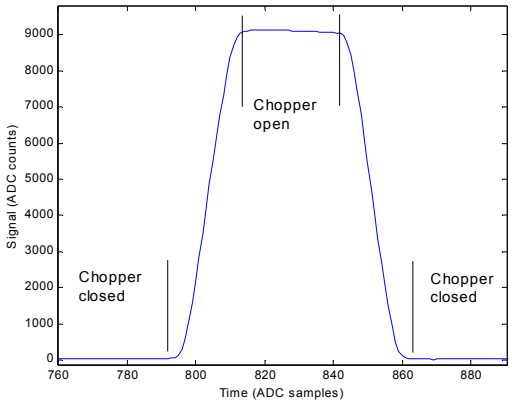

Figure 7. A non-averaged detector signal obtained from base paper at a 20 mm measurement distance. The time between the two "Chopper closed"-periods equals to 0.9 ms.

Furthermore, a good correlation with laboratory reference method for both pigment predictions is achieved as shown in Figures 8 and 9.

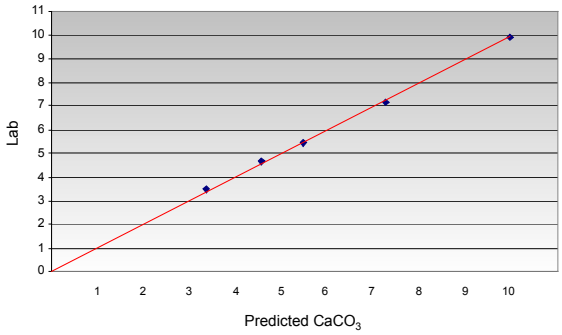

Figure 8. Laboratory reference as compared to the predicted $CaCO_3$.

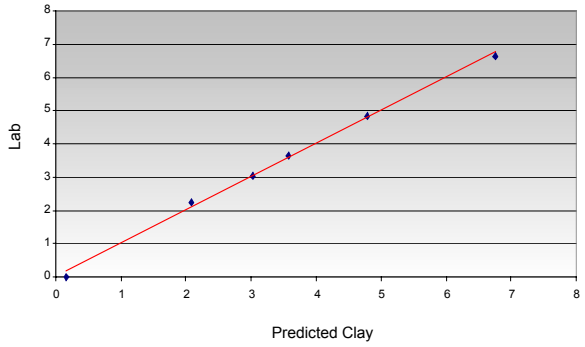

Figure 9. Laboratory reference versus predicted Clay.

The results from pilot coater test run are presented in Figure 10. CW predictions calculated from the $CaCO_3$ and clay predicions correlate well with each other, with OD method and with laboratory reference.

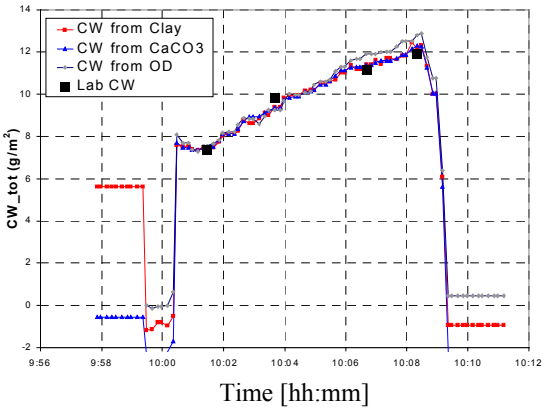

Figure 10. A pilot coater test run. The coat weight is varied over time. Y-axis = coat weight calculated with 4 methods: (1) predicted clay, (2) predicted $CaCO_3$, (3) OD (β-absorption difference) and (4) laboratory reference. The coating consists of 50 % $CaCO_3$ and 50 % clay. Test started at 10.00 and ended at 10.09 (Courtesy of Metso)

Metso Automation's "IQMultiCoat" optical coat weight measurement instruments have been installed on a board mill and are being routinely used in the production process. The results are good and all the requirements that were set at the beginning of the development project have been met.

Online paper moisture analysis by NIR

Antti Kemppainen, Jouko Malinen, Juha Sumen and Markku Känsäkoski

INTRODUCTION

NIR spectroscopy offers a chance to monitor the moisture content of paper web in paper manufacturing processes. A traversing NIR sensor can be inserted into the process as an on-line moisture measuring apparatus, which will offer an opportunity to measure and control the process automatically. Similar technology can also be used in other moisture sensing applications. The feedback from the process is even more valuable if it is received in the early stages of the process. This gives more detailed information on process flow than the measurement data from the end product. In paper making process NIR instruments are typically used to measure from the end product, which is low water content paper. VTT Electronics, Suomen Optomekaniikka and Metso Paper have developed an online analyser that measures the moisture of paper in the press section. The difficulty is the harsh environmental conditions inside the machine. Typically, relative humidity is more than 90% and the temperature is more than 60°C. There is also plenty of loose wood fiber in the air, which makes it difficult to keep the optics of the instrument clean. Furthermore, typical NIR analysers measure different wavelength channels sequentially, which causes errors in the case of a fast moving sample like paper. As a solution, the robust parallel measuring Pronir analyzer was developed.

INSTRUMENT

The instrument is based on a four-channel detector component developed at VTT[1]. Each wavelength channel consists of a PbS-detector and interference filter. All detectors and filters are situated in a single hermetically closed Peltier cooled package. This structure offers the benefit of true parallel measurement of all channels. The detector is thermoelectrically cooled to achieve a higher response and insensitivity to temperature variations. The optics was designed to be insensitive to the distance and temperature variation. The instrument is illustrated in figure 1.

Figure 1. Pronir measurement head. Photo: Metso Paper, Inc.

Temperature dependency was tested by inserting the instrument into a climate chamber with the temperature cycling between 20 and 55°C Celsius. The cycle duration was 3 hours. Figure 2 shows the variation of the normalised moisture signal during the temperature cycling. The test indicates less than 60 ppm/°C dependency on temperature and very low total drift even under high temperature fluctuation. Furthermore, the instrument is regularly referenced to the standard sample during measurement to compensate possible fluctuations.

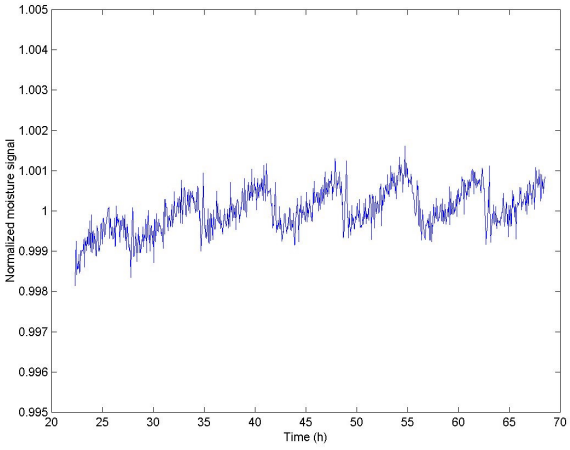

Figure 2. Normalised moisture signal as a function of time (in hours) during temperature cycling.

INSTALLATION

The instrument was installed in the paper machine just after the press section on a traverse scanner. Alongside the paper web there is an automatic cleaning and standardisation station for the analyser in order to compensate possible drift from the instrument output. Air purging is used to prevent the fiber from dirtying the window. Air cooling is also used to control the temperature of the detector and electronics inside the instrument. This causes overpressure on the instrument, which protects the optical components from moisture and dirt. Analyser installation is shown in figure 3.

Figure 3. Moisture analyser installed on a paper machine. Photo by Metso Paper Inc.

OTHER APPLICATIONS

In addition to the paper mill applications, Metso Paper and VTT Electronics intend to make the instrument available for other on-line monitoring needs, where customer needs are not being satisfied with standard NIR instrumentation. The instrument prototype shown in figure 4 was developed for smaller scale traversing applications. The instrument is controlled with a PC computer and can be programmed to monitor multiple locations sequentially within its 1 meter track. The filters for the four-wavelength detector can be chosen for moisture or other composition monitoring needs. The first prototype has been successfully tested for about one year on a textile industry production line.

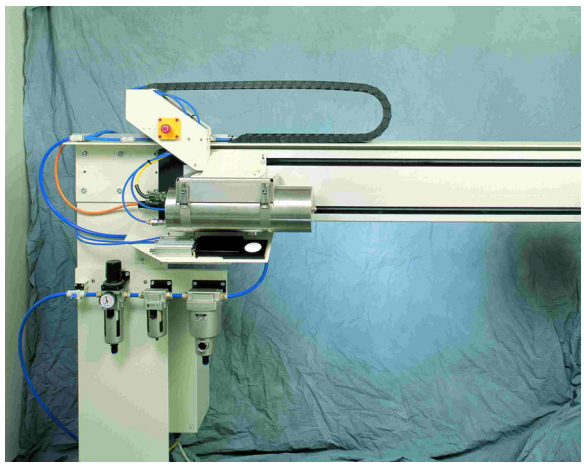

Figure 4. Prototype NIR analyser with about 1 meter traversing capability.

CONCLUSION

The four-channel detector based NIR moisture analyser can be used in many industrial, environmentally demanding applications. Parallel detection enables rapidly moving samples to be measured reliably. Using scanning structures also means that transverse profile information on a process can be achieved.

REFERENCES

1. Hyvärinen T., Niemelä P., Rugged multi-wavelength NIR and IR analyzers for industrial process measurements, In-Process Optical Measurements and Industrial Methods, SPIE Proceedings, 1990.

Monitoring moisture in moving veneer by NIR transmittance spectroscopy

Jouko Malinen, Eero Hietala, Matti Luukkonen* and Eero Hagrén*
* Exéns Development Oy

INTRODUCTION

Thin sheets of wood called veneers are peeled from water soaked, debarked logs onto a lathe in the plywood manufacturing process. The veneers are dried, cut into smaller sheets, graded into various quality categories, patched, jointed if necessary and finally glued together to form laminate boards. Before drying, the moisture of veneer typically ranges from more than 100% for sapwood down to about 30% for heartwood, relative to dry weight. The drying is typically regulated to reach less than 10% moisture content. This often leads to excess drying for most of the material, while leaving a number of palm-sized higher moisture patches in the veneer. Excess drying increases energy consumption whereas higher moisture patches often cause problems in bonding and structural defects in finished panels.

Diffuce reflectance near-infrared (NIR) methods are successfully applied in on-line monitoring of moisture for many applications such as paper and wheat flour production. The commonly used NIR methods are often unreliable, when natural materials of wide quality variation are measured or when surface moisture is no longer representative of the average water content in the material. Transmission spectroscopy in the short wave NIR wavelengths (800-1100 nm) has a penetration depth of millimeters to centimeters for many solid materials and has potential for true average moisture monitoring. Multivariate calibration methods applied to full spectrum 800-1100 nm data can often provide reliable calibrations even for widely variable natural materials. VTT Electronics has developed an LED spectrometer technique for short wave NIR measurements /2/ and applied the technique in the on-line monitoring of crisp bread moisture content /3/. The aim of this study was to examine whether short wave NIR methods can be used for monitoring true moisture content in moving veneer and to demonstrate principles for multi-point instrumentation of process control needs in plywood production.

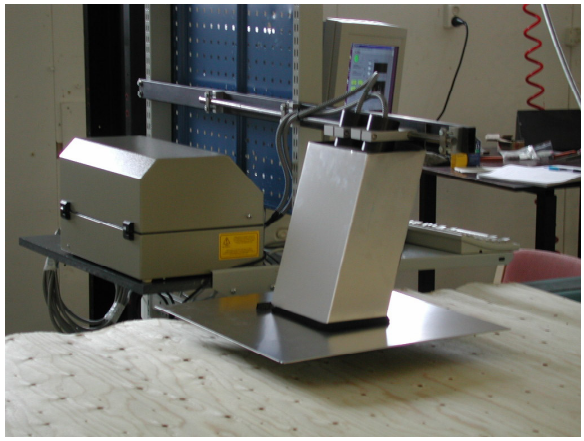

Figure 1. Instrument installation on the veneer track.

EXPERIMENTAL

An experimental instrument was assembled for the study by VTT Electronics and Exéns Development Oy. The LED spectrometer unit provides the light source and wavelength selection functions by electrically scanning 32 wavelengths from 832 to 1048 nm, with a scanning frequency of 71 spectra per second. The measurement beam is delivered with fiber optics to two illumination units, located 0.3 m above the veneer track and illuminating two areas spaced 10 cm center-to-center and sized 2 cm in the direction of the track and 7 cm across the track. Two detector units are located 5 cm under the track, the detector signals are transmitted to a 16-bit A/D board and further processed in a LabView application software running in a PC computer. The performance of the system was first examined in a laboratory with stationary veneer samples of varying wood species, veneer thickness and sample orientation. Moisture calibration and further tests continued with 2.6 mm thick spruce veneer material. A set of 20 calibration samples were collected and measured in 10 different moisture conditions using both the spectrometer and the reference method (oven drying). Finally, sheets of moving veneer were measured using a veneer track built for the purpose by Mecano Group Oy in Kajaani, as shown in Figure 1.

RESULTS

The measurements with stationary samples demonstrated a capability to measure a wide variety of veneers with a single instrument, as illustrated in figure 2. A calibration model for moisture in 2.6 mm thick spruce veneer was developed using MSC-pretreatment, PLS-method and 4 factors. The standard error of prediction (SEP) and the coefficient of correlation (R^2) were 0.96% and 0.954, respectively.

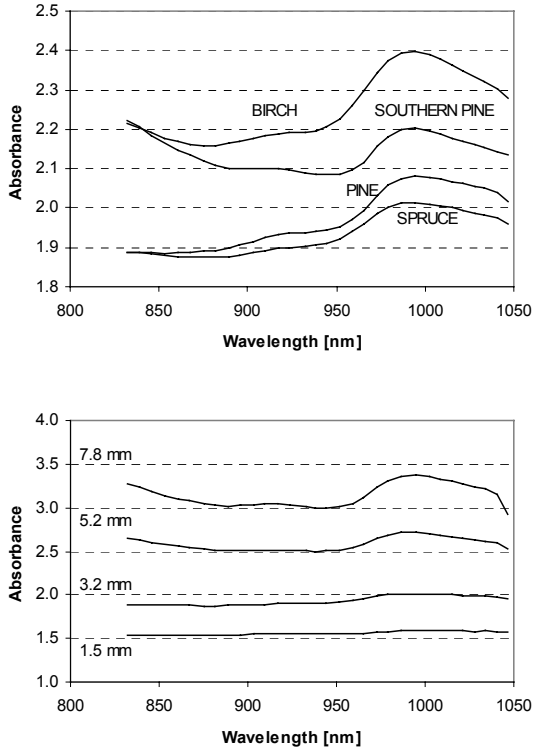

Figure 2. Measured veneer spectra: 3.2 mm thick samples of wood species (above) and a set of spruce samples with varying thickness (below).

Tests with moving veneer demonstrated the detection of about palm-sized patches of higher moisture in veneer moving at 20 meters per minute, see figure 3. The signal-to-noise ratio of measurement remained stable up to speeds of 50 meters per minute, which is a consequence of the scanning frequency of the instrument. In modern veneer production lines the velocity of material can reach 120 meters per minute, which can be achieved through modifications in control and data acquisition electronics.

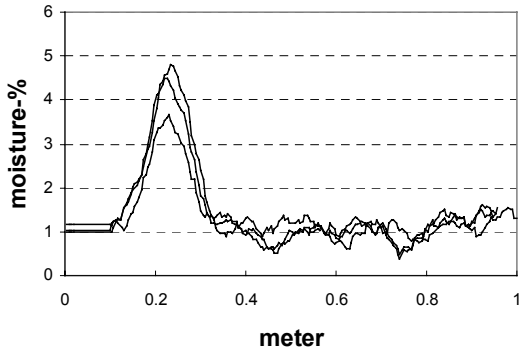

Figure 3. Three repeated measurements on 2.6 mm thick spruce veneer moving at 20 m/minute, with an area of added moisture.

CONCLUSIONS

The study has demonstrated the feasibility of recording spatial moisture variations in sheets of moving veneer by short wave transmittance NIR spectroscopy. The work and the results can be used as a basis for developing a multi-point instrument for the real-time monitoring and controlling of the drying process in plywood production line.

REFERENCES

3. J. Malinen, M. Känsäkoski, R. Rikola, C.G. Eddison, "LED-based NIR spectrometer module for hand-held and process analyser applications", Sensors and Actuators B Chemical, Vol.51/1-3 (1998), pp. 220-226.
4. A. Kemppainen, M. Känsäkoski, J. Malinen, "On-line monitoring of crispbread moisture content by short-wave near infrared spectroscopy", Proceedings of NIR-99 (2000), pp. 371-374.

ACKNOWLEDGEMENTS

The authors wish to thank Mecano Group Oy and Raute Oyj for financial support and their contribution to obtaining the veneer samples and arranging the experiments with moving veneer samples.

Binder profiles in paper coating layers by photoacoustic signal modeling

Janne Paaso, Mari Halttunen, Jussi Tenhunen and Jouni Tornberg

INTRODUCTION

Binder content and distribution in coating layer, together with coating structure, have significant influence on print quality and the printability of coated papers. The uneven ink absorption in print, called mottling, is often connected with the binder migration during the coating and drying process. Therefore, the determination of binder distribution through the coating layer plays an important role in the paper coating research. In this work, the applicability of photoacoustic measurements with signal modeling to resolve the binder depth profiles in coating layers was studied. The objective of photoacoustic modeling work has been to develop a theoretical, semi-empirical or empirical model that could determine the concentration depth profile of SB-latex in paper coating layers from the photoacoustic data. The main emphasis in the work has been on the theoretical and semi-empirical models to avoid the need of calibration samples that are difficult and laborious to produce.

PHOTOACOUSTIC SIGNAL MODELING

The controllable sampling depth feature of PAS is a result of the photoacoustic signal generation process. The signal generation process involves the absorption of light in the sample, which causes production of heat and propagation of heat-generated thermal waves to sample surface. Heat is then transferred into the adjanced gas, changing its pressure. The pressure changes in the closed photoacoustic cell are sensed by a microphone as the photoacoustic signal. When the thermal waves start to propagate from the light irradiated-area where the absorption occurs, and they decay with a decay coefficient that is proportional to the square root of the frequency at which the incoming light is modulated and the thermal diffusivity of the sample. Accordingly, the sampling depth is decreased, when the modulation frequency, f, is increased.

Photoacoustic signal generation has been modelled in several theories, in so-called *direct* models, since the discovery of PAS by Bell in1880 [1]. Based on these theories, the photoacoustic signal can be calculated if the properties of the sample (including the depth profiles of constituent materials) are known. Nevertheless, in our objective the situation is opposite, i.e. the photoacoustic signal of sample is known and the properties of the sample should be worked out. To solve the problem, we need to constitute the *inverse* model. Obviously, a good direct model had to be found first, before the development of the inverse model could be started.

The concentration profiles can also be solved out without any theoretical modeling of the photoacoustic signal, e.g. by experimental data with multivariate calibration. Then, however, a large number of calibration samples are needed to form a representative calibration model.

RESULTS

Simulation of photoacoustic spectra with direct model

The main difficulties in the photoacoustic simulation of coated papers in direct modeling arise from the difference between the thermal parameters of paper and the coating layers. Furthermore, the coating layer is supposed to have uneven concentration depth profiles. These facts together mean that models presented in literature do not apply. The developed model for paper coatings is based on the models of Afromowitz et al. [2] and Fernelius [3], and on the fact that the thermal diffusion equation is linear. The simulations and the measured photoacoustic spectra are in excellent agreement, as shown in the example in Figure 1, except the phase spectrum of the coating composition containing 100 ppw carbonate and

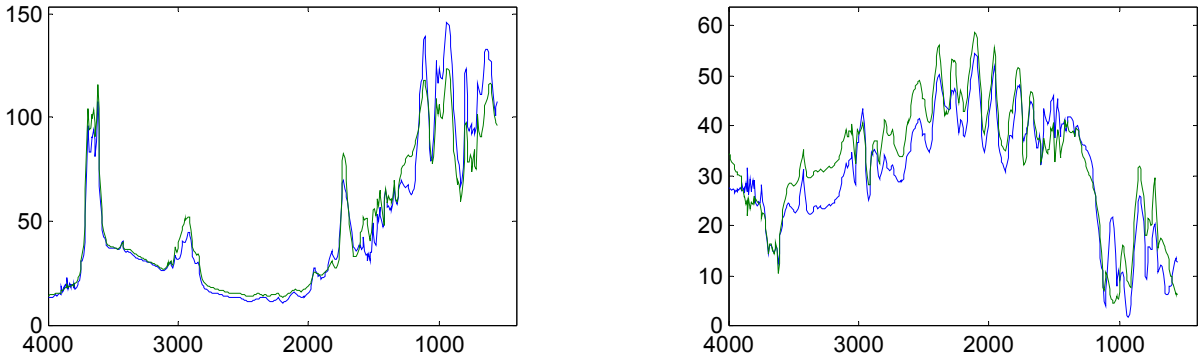

(a) (b)

Figure 1. (a) The simulated (blue) and measured (green) magnitude spectra of kaolin – SB latex coating color at 100 Hz modulation frequency. (b) The simulated (blue) and measured (green) phase spectra of kaolin – SB-latex coating color at 100 Hz modulation frequency.

SB-latex. The simulation results compared with experimental ones were presented in more detail at the proceedings of the 12th International Conference on Fourier Transform Infrared Spectroscopy (ICOFTS-12) [4].

Calculation of binder profiles with inverse models

From the mathematical structure of direct signal generation models, we can conclude that all inverse models intended for concentration depth profiling are so-called ill-posed problems. The ill-posing means that small deviations in the measured PAS signal can lead to large errors in the determined depth profile. This makes PAS depth profiling very demanding - inverse models are very prone to produce spurious depth profiles, because of the presence of noise in the PAS measurements. Even if noise levels are very low, other kinds of deviations from the ideal photoacoustic behaviour easily occur, and cause the inverse model to fail.

Several inverse models related to photoacoustic spectroscopy have been proposed [5]. In this work, we developed two inverse models for PAS depth profiling. The one *is an iterative inverse model*, and its application range is wider. The other is based on the multivariate calibration method. The calculation in *multivariate based inverse model* is faster than in the iterative model, but the multivariate inverse model has some restrictions.

The resolving power of the *iterative inverse model* was at first analysed theoretically. Virtual samples with reasonable amounts of latex, kaolin, and carbonate were created, and their PAS spectra simulated with the direct model. One percent of noise was added to the spectra, and they were given to the inverse model. The inverse model determined the total thickness of the coating colour layer, and the concentration profile of latex in the coating layer. The inverse model works rather well if the latex is enriched deep into the sample. In the opposite situation, there are some difficulties, because the uppermost layer has the greatest effect on the PAS signal, and if the signal from the lowermost layers is very weak, it also results low sensitivity there. Furthermore, the model has an upper limit for the number of layers the model can handle accurately. For example, uniform or discontinuous concentration profiles can be determined accurately by using four layers, but not with five layers.

Also, the *multivariate inverse model* was first tested theoretically. Then, the model was tested with experimental data. It was found that the model can determine the coating colour thickness and the average concentration of latex rather

Table 1. The predicted and measured thickness and concentration of one-layer coating samples*.

Sample	Thickness [μm]	Latex concentration [%]
SB-kaol-10	12.7 (17)	12.0 (10.6)
SB-kaol-20	12.9 (15)	12.8 (10.6)
SB-kaol-60	20.6 (27)	11.5 (10.6)
SB-kaol-90	32.8 (34)	11.2 (10.6)

Table 2. The predicted and measured thickness and concentrations of two-layer coating samples*.

Sample	Thickness [μm]	Layer 1 conc. [%]	Layer 2 conc. [%]
1	21.3 (26.0)	18.0 (13.0)	12.9 (5.7)
2	23.7 (25.0)	11.4 (5.7)	11.2 (13.0)
3	19.1 (20.5)	14.8 (8.3)	11.8 (10.7)
4	21.1 (23.1)	15.5 (10.7)	12.1 (8.3)

*The SB-latex – kaolin coating colour was applied on mylar, and the thickness of the coating layer was varied. The first number is the predicted value, whereas the value in parentheses is the measured one (reference).

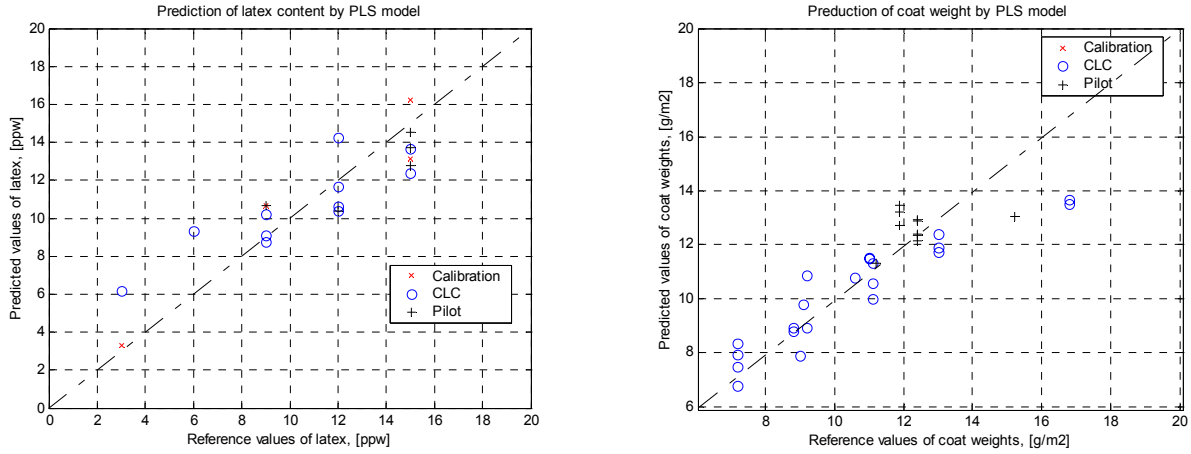

Figure 2. (a) Predicted SB contents (ppw) vs. their reference values (ppw), 3 factors used, (b) predicted coat weights (g/m^2) vs. their reference values (g/m^2), 2 factors used.

well for one layer structures. Typical results from kaolin-based coatings are presented in the following tables. The first number in each column is the model's prediction, and the number in parentheses is the reference value.

The remaining discrepancies between the predictions and measurements are primarily due to two reasons: (1) the model is not capable of handling all the effects occurring in the sample. These effects include scattering and the possible other effects arising from the inhomogeneity of the coating colour, (2) the inverse model needs the absorption coefficients of the constituent materials as input. However, they have to be determined with a very high accuracy, especially in the low-absorption regions of the spectrum. This is very hard to achieve.

The empirical model was done in this work by the multivariate PLS (Partial Least Squares) calibration. This model gave the most accurate estimates for the SB concentration and coating thickness, see Figure 2. It was not possible to test the depth profiling properties due to the lack of suitable samples. A great disadvantage of the multivariate PLS model is the need for the leaning sets, i.e. the coating samples with known chemical composition. Furthermore, the properties of learning sets (e.g. thermal and light scattering properties, porosity) should be similar to the properties of samples to be predicted. In practice, the manufacture of these types of samples is very laborious and sometimes even impossible.

CONCLUSIONS

We have shown that the estimation of latex contents and depth profiles by theoretical models (without experimental calibration samples) cannot give the required accuracy for the prediction. However, the FTIR/PAS technique itself is sensitive enough to give information on latex contents and coat weights, which can be seen from the results of PLS models. The great disadvantage of the prediction that is based on empirical calibration is the analysis of calibration samples prior to analysis of unknown sample sets like in other spectroscopic techniques.

The developed theoretical and empirical models as such cannot be utilized for the industrial purposes to determine the latex concentration profiles and coat weights. However, the project has yielded a good insight into the properties of photoacoustic spectroscopy and its capability in depth profiling work.

REFERENCES

1. Rosencwaig, A., *Photoacoustics and photoacoustic spectroscopy*, Wiley, New York, 1980.
2. Afromowitz, M.A., Yeh, P.S., Yee, S., *J. Appl. Phys*., **48** (1977), 209.
3. Fernelius, N.C., *J. Appl. Phys*., **51** (1980), 650.
4. Paaso, J., Halttunen, M., Tenhunen, J., Stenius, P., Depth profiles in paper coatings: Measured and simulated spectra, *Proceedings in 12th ICFTS conference*, Tokyo, Japan, 1999, p. 299-300.
5. Hodgson, R., *J. Appl. Phys*. **76**, 7524 (1994).

Useful new multivariate calibration technique and application to IR ATR paper coating measurement

Ralf Marbach

INTRODUCTION

Optical measurements are often based on so-called multivariate calibration. For this, an optical instrument measures a set of input signals first, e.g., light absorbance values at several different optical wavelengths, and then an algorithm is used to transform the multiple input numbers into one user-desired output number. Multivariate calibration a.k.a. chemometrics is the process of determining that algorithm. The cost associated with calibration and subsequent calibration maintenance is often much higher than the one-time cost of hardware, and this economic fact has slowed the growth of the optical analyzer industry in the past. The new calibration method recently published in [1] and shortly described here can largely remedy this fact. Future cost reductions are hard to quantify but a factor >3 is expected across the process control field.

THEORY

Whereas calibrations with one or two wavelengths per optical spectrum are perfectly simple, multivariate calibrations with more variables are complicated. The intuitive understanding of the underlying physics is lost because the closed-form solution of the "statistical" calibration model has not been available so far. It was recently derived in [1]. Here, we briefly apply the results to an example from the paper industry, viz., the infrared (IR) measurement of latex concentration at the surface of paper coatings using ATR spectroscopy. The thickness of a typical coating layer varies between 3 and 15 μm and the layer is composed of pigments (e.g. $CaCO_3$ and clay), latex used as glue (e.g. SB-latex), and some minor constituents like optical brightners and thickeners. Concentrations are measured in units of so-called parts-per-weight (ppw), which is relative to pigment weight; e.g., a typical coating composition is pigments 100 ppw (by definition), latex 10 ppw, and additives 1 - 2 ppw. Assume m calibration spectra with k wavelengths each are measured and a traditional calibration is to be performed. The "statistical" calibration model is

$$\mathbf{y}_R = \mathbf{X} \cdot \mathbf{b} + \mathbf{e} \qquad (1)$$

where $\mathbf{y}_{\mathbf{R}(mx1)}$ the vector of the latex reference concentrations measured in a laboratory (in units of [ppw]); $\mathbf{X}_{(mxk)}$ matrix of infrared calibration spectra (in absorbance units [AU]); $\mathbf{b}_{(kx1)}$ regression vector [ppw/AU]; and $\mathbf{e}_{(mx1)}$ error vector [ppw]. The index in parenthesis, e.g., in $\mathbf{X}_{(\mathrm{m\ x\ k})}$, means that the matrix has m rows and k columns. The task is to find a solution for $\mathbf{b}$ which minimizes the error $\mathbf{e}$ and performs well in future predictions. The usual procedure is to first mean-center the data $\widetilde{\mathbf{X}} \equiv \mathbf{X} - \mathbf{1}_{(mx1)} \cdot \bar{\mathbf{x}}^T$ and $\widetilde{\mathbf{y}}_R \equiv \mathbf{y}_R - \bar{y}_R$, where $\bar{\mathbf{x}}^T$ is the mean IR spectrum and $\bar{y}_R$ the mean latex reference concentration of the calibration data set. The "statistical" or "soft modeling" way of calibration is to estimate $\mathbf{b}$ from the least-squares solution,

$$\hat{\mathbf{b}} = (\widetilde{\mathbf{X}}^T \widetilde{\mathbf{X}})^{-1} \widetilde{\mathbf{X}}^T \widetilde{\mathbf{y}}_R \qquad (2)$$

In practice the full-rank inverse in Eq.(2) is often replaced with some rank-reduced inverse, e.g., PCR or PLS; the limited significance of these methods is also discussed in [1]. The soft-modeling way has the following disadvantages:

- specificity can not be proven and is often not achieved;
- calibrations are often affected by dangerous spurious correlations, which can render results useless and can be difficult to detect;
- collection of a statistically representative set of calibration samples is wrongly accepted as a *conditio sine qua non;* in other words, statistical calibration always starts from scratch in spite of the fact that *a priori* knowledge about the spectra is often available that could greatly ease the task;
- calibration time periods are often excessively long in order to collect enough calibration data to "model" all the spectral noises that the instrument is likely to see in future use;there is no good way to quantify the effect of hardware or measurement

process changes on the calibration;[§] there is also no good way to update an existing calibration to slight changes in the hardware or process, or to re-use a calibration for a new but similar application;

- there is no way to quantify the effect of inaccurate lab reference values; and
- there are severe marketing problems associated with "statistical" calibration.

Deriving the closed-form solution of Eq.(2) in terms of its physical building blocks can eliminate all of these disadvantages. The **first step** is to split the calibration spectra into the latex spectral signal and noise as follows:

$$\mathbf{X} = \mathbf{X}_n + \mathbf{y} \cdot \mathbf{g}^T \tag{3}$$

where $\mathbf{X}_n$ is the matrix of spectral noise [AU]; $\mathbf{g}_{(kx1)}$ the latex response spectrum [AU/ppw]; and $\mathbf{y}_{(mx1)}$ the actual latex concentrations [ppw]. After mean-centering we have

$$\widetilde{\mathbf{X}} = \widetilde{\mathbf{X}}_n + \widetilde{\mathbf{y}} \cdot \mathbf{g}^T \tag{4}$$

$$\begin{aligned} \widetilde{\mathbf{y}}_R &= \frac{\widetilde{\mathbf{y}} \cdot \widetilde{\mathbf{y}}^T}{\widetilde{\mathbf{y}}^T \widetilde{\mathbf{y}}} \widetilde{\mathbf{y}}_R + (\mathbf{I} - \frac{\widetilde{\mathbf{y}} \cdot \widetilde{\mathbf{y}}^T}{\widetilde{\mathbf{y}}^T \widetilde{\mathbf{y}}}) \widetilde{\mathbf{y}}_R \\ &\equiv S \cdot (\widetilde{\mathbf{y}} + \widetilde{\mathbf{y}}_n) \end{aligned} \tag{5}$$

where $\widetilde{\mathbf{y}}_n \equiv \left(\mathbf{I} - (\widetilde{\mathbf{y}} \cdot \widetilde{\mathbf{y}}^T)/(\widetilde{\mathbf{y}}^T \widetilde{\mathbf{y}})\right)(\widetilde{\mathbf{y}}_R / S)$ is the reference noise vector [ppw] and $S \equiv \widetilde{\mathbf{y}}^T \widetilde{\mathbf{y}}_R / \widetilde{\mathbf{y}}^T \widetilde{\mathbf{y}}$ the scaling factor between the sample and the lab reference concentrations. In the coating example, as in most other applications, S=1. The mathematically trivial Eq.(5) is the key to arriving at a closed-form solution and it makes intuitive sense. From the point of view of calibration, only the scatter of the reference method, i.e., the part of the vector $\widetilde{\mathbf{y}}_R$ that is *not* correlated with $\widetilde{\mathbf{y}}$, can be called noise. Bias and slope errors of the reference method with regard to the actual sample concentrations, on the other hand, are the mere responsibility of the reference method and have nothing to do with the optics. The **third step** is algebra. Inserting Eqs.(4) and (5) back into Eq.(2) yields:

$$\begin{aligned} \hat{\mathbf{b}} &= \left\{\left(\widetilde{\mathbf{X}}_n^T + \mathbf{g} \cdot \widetilde{\mathbf{y}}^T\right) \cdot \left(\widetilde{\mathbf{X}}_n + \widetilde{\mathbf{y}} \cdot \mathbf{g}^T\right)\right\}^{-1} \cdot \left(\widetilde{\mathbf{X}}_n^T + \mathbf{g} \cdot \widetilde{\mathbf{y}}^T\right) \cdot S \cdot (\widetilde{\mathbf{y}} + \widetilde{\mathbf{y}}_n) \\ &= \frac{S \cdot \left\{\widetilde{\mathbf{X}}_n^T (\mathbf{I} - \frac{\widetilde{\mathbf{y}} \cdot \widetilde{\mathbf{y}}^T}{\widetilde{\mathbf{y}}^T \widetilde{\mathbf{y}}}) \widetilde{\mathbf{X}}_n\right\}^{-1} \left(\mathbf{g} + \frac{\widetilde{\mathbf{X}}_n^T \widetilde{\mathbf{y}}}{\widetilde{\mathbf{y}}^T \widetilde{\mathbf{y}}}\right) \cdot (\widetilde{\mathbf{y}}^T \widetilde{\mathbf{y}})}{1 + (\widetilde{\mathbf{y}}^T \widetilde{\mathbf{y}}) \cdot \left(\mathbf{g} + \frac{\widetilde{\mathbf{X}}_n^T \widetilde{\mathbf{y}}}{\widetilde{\mathbf{y}}^T \widetilde{\mathbf{y}}}\right)^T \left\{\widetilde{\mathbf{X}}_n^T (\mathbf{I} - \frac{\widetilde{\mathbf{y}} \cdot \widetilde{\mathbf{y}}^T}{\widetilde{\mathbf{y}}^T \widetilde{\mathbf{y}}}) \widetilde{\mathbf{X}}_n\right\}^{-1} \left(\mathbf{g} + \frac{\widetilde{\mathbf{X}}_n^T \widetilde{\mathbf{y}}}{\widetilde{\mathbf{y}}^T \widetilde{\mathbf{y}}}\right)} + \ldots \\ \ldots S \cdot \left(\mathbf{I}_{(kxk)} - \frac{\left\{\widetilde{\mathbf{X}}_n^T (\mathbf{I} - \frac{\widetilde{\mathbf{y}} \cdot \widetilde{\mathbf{y}}^T}{\widetilde{\mathbf{y}}^T \widetilde{\mathbf{y}}}) \widetilde{\mathbf{X}}_n\right\}^{-1} (\widetilde{\mathbf{y}}^T \widetilde{\mathbf{y}}) \left(\mathbf{g} + \frac{\widetilde{\mathbf{X}}_n^T \widetilde{\mathbf{y}}}{\widetilde{\mathbf{y}}^T \widetilde{\mathbf{y}}}\right) \cdot \left(\mathbf{g} + \frac{\widetilde{\mathbf{X}}_n^T \widetilde{\mathbf{y}}}{\widetilde{\mathbf{y}}^T \widetilde{\mathbf{y}}}\right)^T}{1 + (\widetilde{\mathbf{y}}^T \widetilde{\mathbf{y}}) \cdot \left(\mathbf{g} + \frac{\widetilde{\mathbf{X}}_n^T \widetilde{\mathbf{y}}}{\widetilde{\mathbf{y}}^T \widetilde{\mathbf{y}}}\right)^T \left\{\widetilde{\mathbf{X}}_n^T (\mathbf{I} - \frac{\widetilde{\mathbf{y}} \cdot \widetilde{\mathbf{y}}^T}{\widetilde{\mathbf{y}}^T \widetilde{\mathbf{y}}}) \widetilde{\mathbf{X}}_n\right\}^{-1} \left(\mathbf{g} + \frac{\widetilde{\mathbf{X}}_n^T \widetilde{\mathbf{y}}}{\widetilde{\mathbf{y}}^T \widetilde{\mathbf{y}}}\right)} \right) \cdot \left\{\widetilde{\mathbf{X}}_n^T (\mathbf{I} - \frac{\widetilde{\mathbf{y}} \cdot \widetilde{\mathbf{y}}^T}{\widetilde{\mathbf{y}}^T \widetilde{\mathbf{y}}}) \widetilde{\mathbf{X}}_n\right\}^{-1} \widetilde{\mathbf{X}}_n^T \widetilde{\mathbf{y}}_n \end{aligned} \tag{6}$$

From the point of view of latex calibration, spectral noise is everything that is not latex; there is no fundamental difference between, say, detector shot noise and the interfering spectra from the other components in the coating. The **second step** is to split the lab references $\mathbf{y}_R$ into signal and noise as follows:

Eq.(6) is the closed-form solution and describes in detail the dependence of the ***b*** vector on the latex signal $\widetilde{\mathbf{y}} \cdot \mathbf{g}^T$; the spectral noise $\widetilde{\mathbf{X}}_n$; the references and their noise, $\widetilde{\mathbf{y}}_R = S \cdot (\widetilde{\mathbf{y}} + \widetilde{\mathbf{y}}_n)$; and the spurious "correlations" $\widetilde{\mathbf{X}}_n^T \widetilde{\mathbf{y}}$. The effect of the lab reference noise on the calibration, in the second summand via $\widetilde{\mathbf{X}}_n^T \widetilde{\mathbf{y}}_n$, is usually dominated by the effects of the spurious correlations $\widetilde{\mathbf{X}}_n^T \widetilde{\mathbf{y}}$. Electrical engineers may already recognize the similarities between Eq.(6) and the famous Wiener or "matched"

[§]One can model any effect and study its error propagation through an *existing* calibration, but that calibration would have been different if it had seen the effect before.

filter used in time-signal processing applications, e.g., in cellular phones.

Eq.(6) looks complicated because it contains all the adverse effects that the user is trying to get rid of in his calibration experiment. If we now assume that the user has succeeded in sampling a calibration data set in which, first, the effect of reference noise is zero, $\tilde{\mathbf{X}}_n^T \tilde{\mathbf{y}}_n = \mathbf{0}$, and second, the effect of spurious correlations is zero, $\tilde{\mathbf{X}}_n^T \tilde{\mathbf{y}} = \mathbf{0}$, then Eq.(6) shrinks to

$$\hat{\mathbf{b}} = S \cdot \frac{\left\{\tilde{\mathbf{X}}_n^T \tilde{\mathbf{X}}_n\right\}^{-1} \mathbf{g} \cdot (\tilde{\mathbf{y}}^T \tilde{\mathbf{y}})}{1 + (\tilde{\mathbf{y}}^T \tilde{\mathbf{y}}) \cdot \mathbf{g}^T \left\{\tilde{\mathbf{X}}_n^T \tilde{\mathbf{X}}_n\right\}^{-1} \mathbf{g}} \qquad (7)$$

which *is* the spectrometric incarnation of the celebrated **Wiener filter.** The solution Eq.(7) is specific *and* optimal in the mean-square error sense. If all of todays "statistical" calibrations were based on a large enough number of calibration samples and were free of unspecific correlations, all their solutions Eq.(2) would converge against Eq.(7). With Eqs.(6) and (7) now being available, one can use *a priori* knowledge of the physics of the measurement problem to speed up the convergence process and to reduce the need for expensive calibration samples.* **Ways to save money** are numerous and application specific, but the core statement is this: One can combine different pieces of *a-priori* physical knowledge about the spectra with any available measured data to estimate the pure-component spectral signal and the spectral noise in a first step, and then compute the Wiener filter "manually" in a second step by plugging the results into Eq.(7). Spurious and unspecific correlations as well as reference noise effects are eliminated. Tradeoffs concerning practically important issues like calibration transfer or long-term stability become possible by adjusting the estimate of spectral noise; e.g., a calibration can be made "universal" by including instrument-to-instrument noise. In the simple two-wavelengths case, people have always used the Wiener filter without calling it by that name. Now the same can be done in the multivariate case. **Benefits to industry** include:

- significantly reduced cost of calibration; in particular, lab reference values are no longer neccessary as soon as the shape of the response spectrum is known
- guaranteed specificity (important to the biomedical and other regulated industries)
- significantly improved R&D processes enabled by meaningful hardware specifications derived directly from their effect on the user-relevant noise (cmp. Eq.(8) below)

MULTIVARIATE SIGNAL-TO-NOISE

Correlation of a small spectral signal with amplitude 0.1 mAU rms is just as valuable as is correlation of a large signal with 100 mAU rms. In other words, signal-to-noise ratio (SNR) counts not signal amplitude. SNR and correlation coefficient measure the same thing and are related via $r^2 = SNR^2/(1+SNR^2)$. The S/N ratio of the multivariate optical measurement is

$$SNR_x = \frac{\sqrt{\frac{\tilde{\mathbf{y}}^T \tilde{\mathbf{y}}}{m-1}} \cdot \|\mathbf{g}\|}{\sqrt{\frac{1}{\frac{\mathbf{g}^T}{\|\mathbf{g}\|}\left\{\frac{\tilde{\mathbf{X}}_n^T \tilde{\mathbf{X}}_n}{m-1}\right\}^{-1}\frac{\mathbf{g}}{\|\mathbf{g}\|}}}} \quad \left[\frac{AU_{rms}}{AU_{rms}}\right]$$

$$= \frac{\sqrt{\frac{\tilde{\mathbf{y}}^T \tilde{\mathbf{y}}}{m-1}}}{\sqrt{\frac{1}{\mathbf{g}^T\left\{\frac{\tilde{\mathbf{X}}_n^T \tilde{\mathbf{X}}_n}{m-1}\right\}^{-1}\mathbf{g}}}} \quad \left[\frac{ppw_{rms}}{ppw_{rms}}\right] \qquad (8)$$

where the numerator is the rms signal and the denominator is the rms *effective* noise. The latter is the limit of detection of the multivariate measurement. The rms prediction error PRESS$^{1/2}$ in scatter plots approaches this value *if* spurious and unspecific correlations are zero and the slope is one and the reference noise is zero. The covariance matrix of the spectral noise transforms into the scalar effective noise in a peculiar way that is similar to a harmonic mean (1 over inverse). This is the mathematical explanation of the power of multivariate calibration over multiple univariate calibrations, and the reason why the effective noise is often

* A remark to readers with chemometrics background: The so-called "classical" model, which requires knowledge of *all* components in the sample, is different from and inferior to the Wiener filter Eq.(7). The classical model should generally not be used for quantitative analyses because it misuses the knowledge about the other response spectra to construct a very unrealistic estimate of the spectral noise [1].

much smaller than initially believed possible. Typical values achieved in successful IR applications range from about SNR_x=2 ... 20.

Two further definitions are needed. The univariate S/N ratio of the lab references is given by the familiar expression $SNR_y \equiv \sqrt{\tilde{\mathbf{y}}^T\tilde{\mathbf{y}}/\tilde{\mathbf{y}}_n^T\tilde{\mathbf{y}}_n}$ and the *total* SNR of the calibration data set is

$$SNR \equiv \sqrt{\frac{SNR_x^2 \cdot SNR_y^2}{1 + SNR_x^2 + SNR_y^2}} \qquad (9)$$

All measures of calibration quality, e.g., correlation coefficient, slope, PRESS[1/2], etc., are dependent on total SNR and *not* on the individual SNR_x and SNR_y [1]. Because the lab references serve as a secondary standard and are assumed "true" by definition, the infrared method usually gets blamed for the total SNR, which is lower than either SNR_x or SNR_y, when in fact it is responsible only for SNR_x. The optical method is better than the reference method whenever $SNR_x > SNR_y$, but in the past this fairly common situation could only be proven if a second, better reference method became available.

When the total SNR is lower than about five then the calibration becomes slope-deficient, i.e., the data points on the prediction scatter plot are dragged towards the average concentration (high values are predicted too low and *vice versa*) [1]. Because users are free to correct for slope deficiency at their own discretion, PRESS[½] is not a unique measure of calibration quality. On the other hand, correlation coefficient and SNR are unique measures of calibration quality because the user changing the slope does not affect them.

EXAMPLE

A multitude of different coated papers and so-called standard films were measured using ATR spectroscopy in the mid-IR wavelength range. Experimental details are given in [2]. The films were approx. 1 mm thick and were originally prepared to serve as calibration standards in a "statistical" calibration. However, since the response spectrum of latex was known, the new method was applied instead and the films were not used in the calibration at all. The response spectrum of latex is dependent on its composition and thus on its manufacturer. We defined the response spectrum as shown in Fig.1, which contains only those bands that are common between different brands of latex, i.e.,

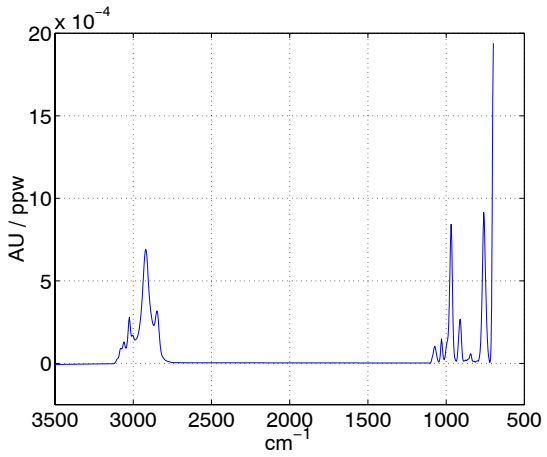

Fig.1 User-defined response spectrum of latex.

manufacturer-dependent bands were set to zero. In effect, we used only a subset of the available latex spectral signal, in exchange for generality. The covariance matrix of the spectral noise was determined from several thousand spectra of different paper coatings, some of which are shown in Fig.2. The (unknown) latex concentrations in the paper coatings varied, i.e., the

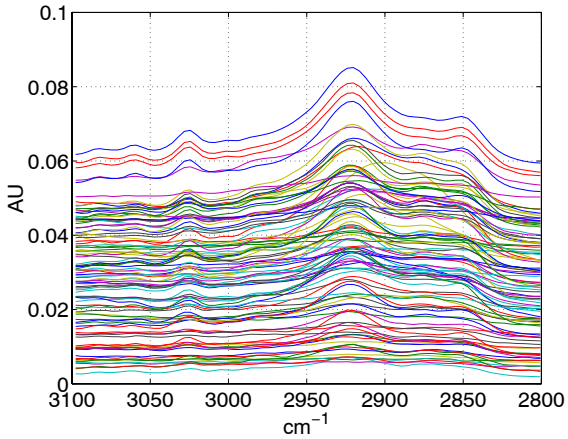

Fig.2 Spectral noise, 100 randomly selected spectra.

variance seen in Fig.2 comes from both spectral noise and an unknown amount of rms latex signal. This fact, however, does not change the *shape* of the ***b*** vector but only its magnitude, which is irrelevant here, since the slope will be adjusted to one anyway. A practical difficulty arising from the unknown amount of latex signal in the estimate of the spectral noise, is that one has to estimate the *average* latex concentration in the noise spectra for offset correction. One of the intentions of the study was to find out

whether the latex concentration on the surface of the coatings is different from the one in the bulk. In the λ range 3200 - 2800 cm^{-1} ATR penetration depth is <1 μm so very shallow surfaces can be studied [2]. Plugging the latex

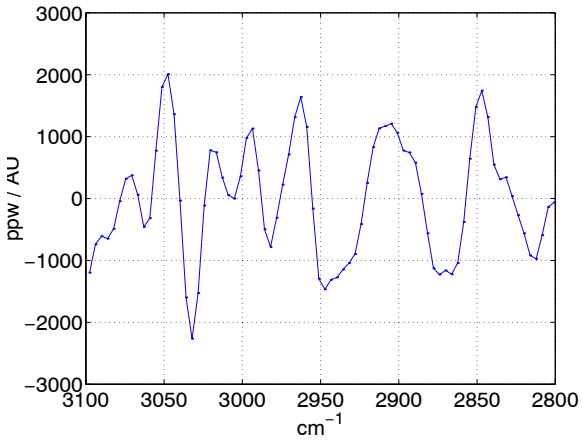

Fig.3 Latex ***b*** vector, slope=1.

response spectrum (Fig.1) and the paper coating spectral noise (Fig.2) into Eq.(7) and adjusting the slope to one, results in the Wiener filter shown in Fig.3. (This ***b*** vector was used to study the spatial uniformity of different paper coatings, to be published). Here, we just show

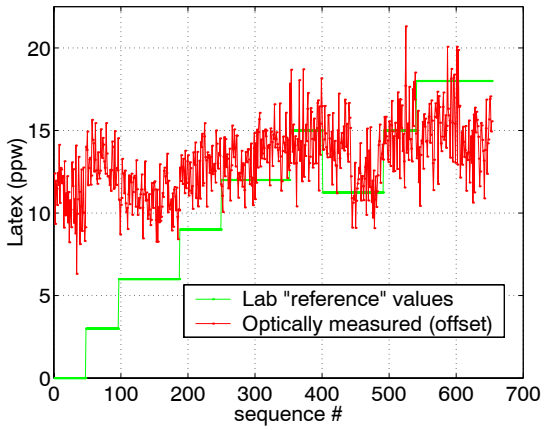

Fig.4 Validation of latex ***b*** vector.

results of the surface concentration of the standard films. Repeat optical measurements were performed on different spatial locations of each film and some exemplary results are shown in Fig.4. Whereas the latex concentration in the *bulk* of the films was made in the lab to vary in steps over a wide dynamic range from 0 to 18 ppw, the latex concentration in the optically probed surface of the films varied hardly at all.

SUMMARY

All calibration methods try to converge against the spectrometric Wiener filter. The usual practice of "statistical" calibration is inefficient whenever *a priori* physical knowledge about the spectral signal and/or noise is available. The closed-form solution opens multiple ways to utilize *a priori* knowledge effectively. Specifically, spurious correlations can be eliminated and conscious decisions about the use of unspecific correlations can be made. Lab reference values are no longer needed as soon as the shape of the pure-component response spectrum is known. Specificity can be proven and the signal-to-noise ratios of the optical method and the lab reference method can be determined individually.

The new method provides significant net present value to companies in various fields using multivariate calibration, in particular, companies developing spectrometric instruments and applications. The cost of multivariate calibration can be significantly reduced. The most important piece of physical information and the key to the most significant savings is knowledge of the shape of the pure component spectrum of the analyte of interest. In addition, there is opportunity for revenue increases due to increased customer acceptance of calibration-based products.

REFERENCES

1. R. Marbach, "On Wiener filtering and the physics behind statistical modeling," Journal of Biomedical Optics 7(1), 130-147 (2002)
2. E. Kenttä, K. Juvonen, M. Halttunen, and J. Vyörykkä, "Spectroscopic techniques for determination of latex content of coating layers," Nordic Pulp and Paper Research Journal, 15(5), 579-597 (2000)

Production Improvement by a New Optimised method in wood quality Control and Cutting with an HIgh-performance Online system

Jari Miettinen, Risto Mitikka and Heikki Ailisto

A multi-sensor system for real time inspection of wood especially suited for the online quality control was developed.

The main goals of PINOCCHIO were to
1) reduce the level of uncertainties with respect to human inspection
2) detect and localise internal wood defects
3) reduce waste at wood waste
4) drive the cutting machine and optimise its timing
5) reduce production costs
6) obtain customised systems, thanks to modular, flexible architecture

Multiple sensor data is processed by means of fusion techniques to obtain the optimum amount of significant information from the inspected samples. The system produces a fast decision for action to be performed in order to drive a cutting plant according to flexible production rules.
The multi-sensor system consists of an infrared radiation sensor and RGB sensor and an optical shape sensor. VTT Electronics designed and realised the RGB system.

The heart of the RGB system are two line scan cameras, frame grabber cards and an analysis program. As the board moves under the imaging system, software triggers the imaging. Two cameras grab lines both sides at constant intervals. The resulting image represents the whole board, in which surface defects (e.g. knots) are detected. The RGB camera system is shown in Figure 1. Feature calculation and defect detection is shown in Figure 2a) and 2b) respectively. The system has the following performance: imaging speed of 3 m/s with 0.8 mm resolution, and image analysis can detect defects and their location.

In the test material average error escape rate was under 30% and average false alarm rate was under 23%.

Figure 1. The RGB camera system.

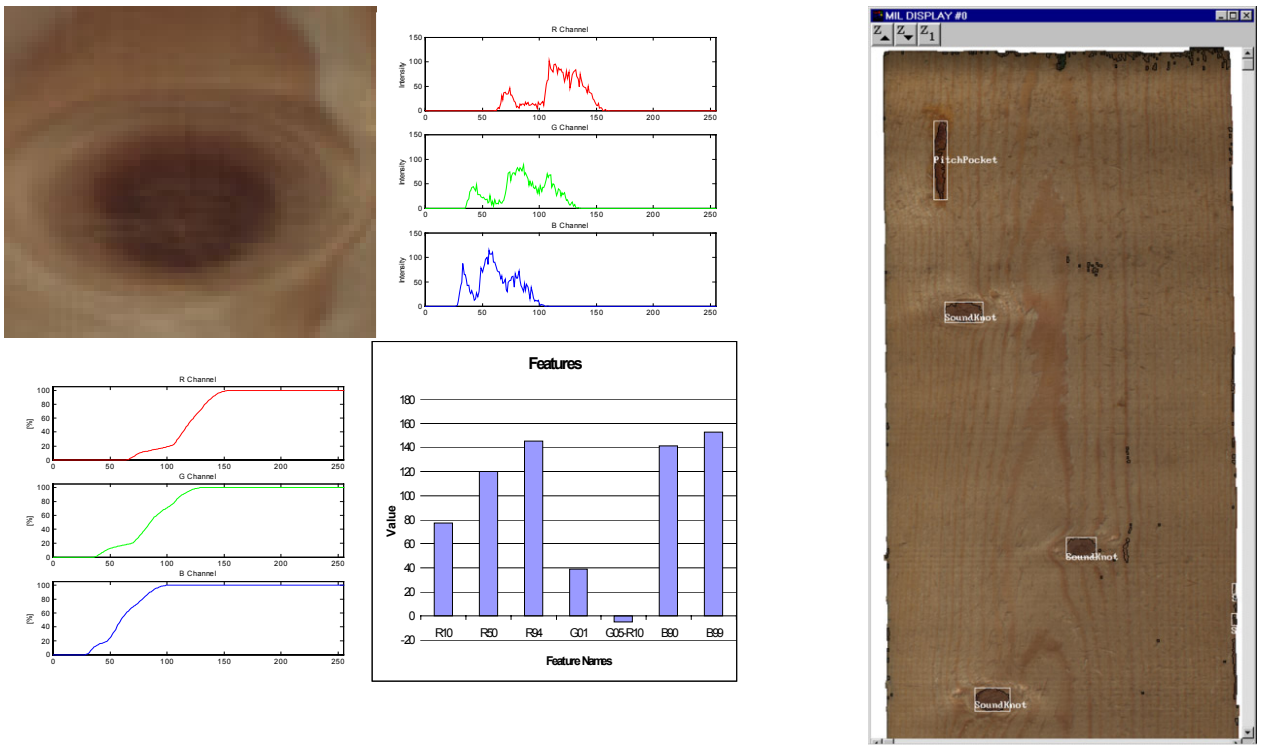

a) b)

Figure 2 a) Feature calculation and b) defect detection.

The PINOCCHIO project belongs to BRITE EURAM Program and it was carried out between 1998 and 2001. The Consortium consists of five main partners. The co-ordinator of this EU project is CEO (Centro di Eccellenza Optronica), which was set up in Florence to promote and develop scientific research and technological innovation in the field of optoelectronics.

Two VTT research institutes took part in the project, namely VTT Building Technology and VTT Electronics. VTT Building Technology works in the area of wood technology and VTT Electronics in computer vision.

OMGA is a medium-sized firm which began by building manual cross-cutting machines for timber. Koskinen Oy is customer-oriented woodworking company. The Company "Los Almerillos", shortened to LOSAL, is one of Spain's biggest solid wood timber producers, supplying furniture manufacturers.

ABSTRACTS OF EXAMINATION THESES

Abstract of Doctoral Thesis

Aikio, Mauri. Hyperspectral prism-grating-prism imaging spectrograph. Espoo 2001, Technical Research Centre of Finland, VTT Publications 435. 114 p.+ app. 7 p.

Keywords imaging spectroscopy, prism-grating-prism components, PGP, optical design, fiber optics, hyperspectral, airborne

Hyperspectral prism-grating-prism imaging spectrograph

A new type of a direct vision dispersing component, the prism-grating-prism (PGP), was invented by the author in 1991. This patented component allows small, low-cost hyperspectral imaging spectrographs suitable for industrial and research applications in the wavelength range from 320 nm to 2700 nm, limited by the transmission of the grating material.
The PGP spectrograph optics and the design procedure are described. The concept has been applied to many hyperspectral imaging spectrographs. The potential of the PGP construction is shown by introducing four designs in detail. 1) The prototype of a low-cost airborne hyperspectral imaging spectrograph, AISA, was the first application of the PGP concept. 2) A microscope imaging UV-VIS-NIR spectrometer system for spectral measurement of micrometer-sized objects such as wood fibers was developed. 3) A multiple-points PGP spectrograph connected to optical fibre probes was designed for industrial applications such as on-line colour and oil film thickness measurements. 4) The PGP spectrograph design for a high-speed interrogation system for large-scale fibre optic Bragg grating arrays is described.

The PGP concept and the results of the developement work were so promising, that a company was founded in 1995 to commercialize, further develope and manufacture PGP spectrograph technology. Today PGP spectrographs are used world-wide for industrial machine vision and spectral analysis, airborne remote sensing and scientific applications in the form of standard products and customized OEM components.

Abstract of Master's Thesis

Jussi Hiltunen (2001) Organic light-emitting devices as pulsed light sources. University of Oulu, Department of Electrical Engineering, 66 p.

Organic light-emitting devices as pulsed light sources

In this study, the transient and steady state performance of organic light-emitting devices (OLEDs) has been investigated with a view towards the suitability for pulsed light sources. Several OLED structures with different materials were manufactured and characterized. The tested devices cover single and multi-layer structures. Both molecular and polymeric materials were used. All these materials are commercially available. Both steady state and transient characterization were carried out. In steady state characterization current-voltage and light intensity properties were investigated. Optimization for an efficient device is outlined. Temperature effects on device performance were also investigated. In transient characterization OLEDs were pulsed with different driving voltage levels. The effect of the driving and bias voltage on the response time was under investigation. Current density variations in transients due to capacitive effects are also discussed.

Keywords: OLED, organic electroluminescene, organic electronics

Abstract of Master's Thesis

Tuomikoski, Markus, Performance and stability of organic light emitting devices, Master Thesis, University of Oulu, Department of Chemistry, 2001, 76p.

Performance and stability of organic light emitting devices

There has been continuous interest in developing organic light emitting devices (OLEDs). Their low operating voltage and power consumption, simplicity of fabrication, thin structure, flexibility, light weight, wide viewing angle, low cost and full-color range in the visible spectrum offer OLEDs potential use in emissive display technology.

The importance of designing the device has been shown. The performance of the OLED was significantly enhanced by optimizing the device structure, organic and cathode materials and their thicknesses. The best results were achieved with the multilayer structure consisted of ITO (an anode), PEDOT:PSS (a hole injection layer), alpha-NBD (a hole transport layer), Alq3 (an emitting/transport layer) and Mg (a hole injection layer). The turn-on voltage, the luminance of 100 cd/m2 and the maximum external quantum efficiency of 1.2% were achieved at 2.5V, 3.5V and 5.5V, respectively. Therefore, the device performance is suitable for many applications, such as backlight in portable displays, mobile phones and wrist watches or even OLED displays.

The most critical performance characteristic for OLEDs is the device lifetime, both storage and operational. Developing reliable organic devices remains a challenge. During operating at room and elevated temperatures the devices based on TPD material degraded resulting in the formation of black spots. The alpha-NBD device was stable at these temperatures. Both devices showed degradation at high brightness due to the local Joule heating.

Device under operation often shows deterioration through formation of black spots, which are commonly introduced by cathode delamination, interdiffusion between organic layers and impurities. At 20 cd/m^2 the lifetime was extrapolated to 18300 hours, which is close the requirement of display applications. In conclusion, the main problem associated with OLEDs is a short lifetime at the high brightness.

More effort has to be used with regard to the purity conditions at the laboratory. In addition, a better barrier effect against moisture and oxygen could be achieved with advanced packaging. Follow-up research should be done with the dopant molecules and the thin insulating LiF layer, which enhanced the performance and the lifetime of the OLEDs.

PUBLICATIONS

Refereed scientific journal papers

1. Ahola, Heikki; Heikkinen, Veli; Keränen, Kimmo; Suomela, J., Modified ITER in-vessel viewing system, Fusion Engineering and Design, vol. 58-59 (2001), 513 - 516.

2. Halttunen, Mari; Vyörykkä, Jouko; Hortling, Bo; Tamminen, Tarja; Batchelder, David; Zimmermann, Anette; Vuorinen, Tapani, Study of residual lignin in pulp by UV resonance raman spectroscopy, Holzforschung. Vol. 55 (2001) No: 6, 639 - 644.

3. Keränen, Kimmo; Karioja, Pentti; Blomberg, Martti; Tenhunen, Jussi; Rusanen, Outi; Kopola, Harri, Miniaturization and module integration of an IR-spectrometer , Optical Engineering, Vol. 40 (2001) No: 10, 2308 - 2314.

4. Kololuoma, Terho; Oksanen, J.; Raerinne, P.; Rantala, Juha, Dye-doped sol-gel coatings for near-infrared laser protection, Journal of Materials Research (2001) No: 16, 2186 - 2188.

5. Lahti, Markku; Lantto, Vilho, Passive RF band-pass filters in an LTCC module made by fine-line thick-film pastes, Journal of the European Ceramic Society (2001) No: 21, 1997 - 2000.

6. Laitinen, Jyrki; Saviaro, Jani; Ailisto, Heikki, Evaluation of solid-state camera systems in varying illumination conditions, Optical Engineering . Vol. 40 (2001) No: 6, 896 - 901.

7. Lenkkeri, Jaakko; Jaakola, Tuomo, Rapid power cycling of flip-chip components on ceramic substrates, Mikroelectronics Reliability . Vol. 41/5 (2001), 661 - 668.

8. Luukkonen, Pirjo; Rantanen, Jukka; Mäkelä, Krista; Räsänen, Eetu; Tenhunen, Jussi; Yliruusi, Jouko, Characterization of wet massing behavior of silicified microcrystalline cellulose and alfa-Lactose Monohydrate using near-infrared spectroscopy, Pharmaceutical Development and Technology. Marcel Dekker. Vol. 6 (2001) No: 1, 1 - 9.

9. Niemelä, Pentti; Suhonen, Janne, Rugged fiber-optic raman probe for process monitoring applications, Applied Spectroscopy. Vol. 55 (2001) No: Oct., 1337 - 1340.

10. Rantala, Juha; Kärkkäinen, Ari; Hiltunen, Jussi; Keränen, M.; Kololuoma, Terho; Descour, Michael, UV light induced surface expansion phenomenon of hybrid glass thin films, Optics Express (2001) No: 8, 682 - 687.

11. Rautioaho, Risto; Nousiainen, Olli; Leppävuori, Seppo; Lenkkeri, Jaakko; Jaakola, Tuomo, Thermal fatigue in solder joints of Ag-Pd and Ag-Pt metallized LTCC modules, Microelectronics Reliability. Vol. 41 (2001), 1643 - 1648.

12. Silvennoinen, Raimo; Peiponen, Kai-Erik; Sorjonen, Mika; Tornberg, Jouni; Sumén, Juha, Diffractive optical sensing of the surface quality of coated paper, Paperi ja puu. Vol. 83 (2001) No: 5, 395 - 399.

Monographs

1. Aikio, Mauri, Hyperspectral prism-grating-prism imaging spectrograph, VTT Electronics, Espoo. 114 p. + app. 7 p., VTT Publications : 435, ISBN 951-38-5850-2; 951-38-5851-0

International conference papers

1. Aikio, Janne; Howe, Dennis, Extremely short external cavity laser: profilometry via wavelength tuning, CLEO 2001 Technical Digest. Baltimore, US, 6 - 11 May 2001. Baltimore (2001), 484 - 485.

2. Aikio, Janne; Kataja, Kari; Howe, Dennis, Extremely short external cavity lasers: direct semiconductor laser readout modeling by using finite difference time domain calculations, Proc. SPIE 4595. Singapore, 27 - 30 Nov. 2001. SPIE (2001), 163 - 173.

3. Ailisto, Heikki; Heikkinen, Veli; Mitikka, Risto; Myllylä, Risto; Kostamovaara, Juha; Mäntyniemi, Antti; Koskinen, Markku; Ulbrich, Gerd; Pereira do Carmo, Joao, 3-D imaging with scannerless LIDAR, Proceedings of ODIMAP III, 3nd Topical Meeting on Optoelectronic Distance/Displacement Measurements and Applications. Pavia, IT, 20 - 22 Sept. 2001. University of Pavia, AEI. Pavia (2001), 202 - 207.

4. Crookell, Andrew; Känsäkoski, Markku; Brook, Richard, Remote sensing of motor vechicle exhaust emissions: the road ahead , Advanced Environmental and Chemical Sensing Technology, Eds., Vo-Dinh, Tuan., Buettgenbach, Stephanus., SPIE proceedings vol. 4205. SPIE (2001), 35 - 42.

5. Descour, Michael, Liang, C., Rogers, JD, Kärkkäinen, Ari, Micro-optical imaging systems: an overview of current state-of-the-art, SPIE ISPA, Singapore, 26-30 Nov., 2001, pp. (Invited)

6. Guillaume, Nadine; Lahti, Markku; Cresswell, Michael; Allen, Richard; Zaghloul, Mona; Linholm, Loren, A novel non-contact electrical CD metrology sensor for chrome photomasks, 21st Annual BACUS Symposium on Photomask Technology. Monterey, CA, US, 2 - 5 Oct. 2001 Proceedings of SPIE. Vol 4562 (to be published) (2001).

7. Halttunen, Mari, Determination of latex distributions in paper coating layers with IR/ATR and confocal-Raman spectroscopic techniques, The 1st International Conference on Advanced Vibrational Spectroscopy. Turku, FI, 18 - 25 Aug 2001. Turku (2001), E1

8. Halttunen, Mari; Jääskeläinen, Anna-Stiina; Löijä, Mia; Perander, Anna-Maija; Vyörykkä, Jouko; Vuorinen, Tapani, Evaluation of pulping and bleaching processes with novel spectroscopic techniques, 7th Brazilian Symposium on the Chemistry of Lignins and Other Wood Components. Brazil, 2 - 5 Sep 2001 (2001), 91 - 98.

9. Halttunen, Mari; Löija, Mia; Tenhunen, Jussi; Kenttä, Eija; Vuorinen, Tapani; Stenius, Per, Determination of sb-latex distribution at paper coating surfaces with FTIR/ATR spectroscopy, Tappi Coating and Graphics Arts Conference and Trade Fair. Hyatt Regency, San Diago, CA, US, 6 - 9 May 2001. Tappi (2001), 203 - 211.

10. Jaakola, Juha; Väänänen, Juha; Lenkkeri, Jaakko; Ollila, Jyrki, Reliability assessment for thin profile ceramic bandpass filters, Proceedings of the 38th IMAPS Nordic Annual Conference. Oslo, NO, 23 - 26 Sept. 2001 (2001), 128 - 133.

11. Juuso, Sanna; Liang, Chen; Mäkinen, Jukka-Tapani; Rantala, Juha; Descour, Michael, Modeling of micro-optical systems by using non-sequential ray tracing, Proc. SPIE, Functional Integration of Opto-Electro-Mechanical Devices and Systems. Vol. 4284 (2001) , 115 - 121.

12. Karppinen, Mikko; Charbonneau, Robert; Berini, Pierre, Attenuated total reflection modulator based on surface plasmon excitation, Photonic Systems and Applications. Singapore, 27 - 30 Nov. 2001. Sidorin, Y. & Tang, D. (eds.). SPIE. Bellingham, Washington, US (2001), 259 - 267.

13. Karppinen, Mikko; Kautio, Kari; Heikkinen, Mikko; Häkkilä, Jonna; Karioja, Pentti; Jouhti, Tomi; Tervonen, Ari; Oksanen, Markku, Passively aligned fiber-optic transmitter integrated into LTCC module, Micro- and Nano-optics for Optical Interconnection and Information Processing. US, 29 - 31, Jul 2001. Taghizadeh, M., Thienpont, H., Jabbour & G., San Diego (eds.). SPIE. Bellligham, Washington, US. Vol. 4455 (2001), 293 - 302.

14. Karppinen, Mikko; Kautio, Kari; Heikkinen, Mikko; Häkkilä, Jonna; Karioja, Pentti; Jouhti, Tomi; Tervonen, Ari; Oksanen, Markku, Passively aligned fiber-optic transmitter integrated into LTCC

module, Proceedings of 51st Electronic Components and Technology Conference. Florida, 29 May - 1 June 2001. Florida (2001), 20 - 25.

15. Karppinen, Mikko; Mäkinen, Jukka-Tapani; Kemppainen, Antti; Borenius, Marianne; Karioja, Pentti, Free-space optical backplanes based on beacon-like links or on a ring bus, Micro- and Nano-optics for Optical Interconnection and Information Processing. US, 29 - 31 Jul 2001. Taghizadeh, M., Thienpont, H., Jabbour & G., San Diego (eds.). SPIE. Bellingham, Washington, US. Vol. 4455 (2001), 88 - 99.

16. Kololuoma, Terho; Kärkkäinen, Ari; Tolonen, Ari; Haatainen, Tomi; Rantala, Juha, Fabrication of Photoimageable tin dioxide coatings from methacrylic and benzoylacetone modified tin alkoxides SPIE Conference, Opto South-West. Tuscon, US, 17 - 18 Sept. 2001. SPIE. US (2001).

17. Kololuoma, Terho; Oksanen, Jari; Raerinne, Paavo; Rantala. Juha, Novel material technique approaches for laser protection, Finnish Defence Forces Technical Research Centre Publications 4/2001. Nordic Symposium on Military Electro-Optics. Helsinki, FI, 17 - 18 Oct 2001. Kaurila, T. (ed.). Helsinki (2001), 7 p.

18. Kopola, Harri, Advanced technologies for optoelectronic module integration, OIE'01. Technical Digest of Fourth Japan-Finland Joint Symposium on Optics in Engineering.Osaka, JP, 2001 (2001), 7 - 8. (Invited)

19. Kopola, Harri, Advanced technologies for photonic module integration, Photonic Systems and Applications. Singapore, 27 - 30 Nov 2001. Sidorin, Y. & Tang, D. (eds.). SPIE. Bellingham, Washington, US. Vol. 4595 (2001), 332 - 333. (Invited)

20. Kopola, Harri; Lenkkeri, Jaakko; Kautio, Kari; Torkkeli, Altti; Rusanen, Outi; Jaakola, Tuomo, MEMS sensor packaging using LTCC substrate technology, Proc. SPIE. Device and Process Technologies for MEMS and Microelectronics II. Adeleine, AU, 17 - 19 Dec 2001. SPIE (2001), 148 - 158. (Invited)

21. Känsäkoski, Markku; Niemelä, Pentti, Requirements analysis for remote measurement of vechile emissions at low cost (REVEAL), 3rd International Conference on Urban Air Quality and 5th Saturn Workshop. Loutraki, GR, 19 - 23 March 2001 (2001), 4 p.

22. Kärkkäinen, Ari; Rogers, Jeremy; Jabbour, Ghassan; Rantala, Juha; Descour, M.R, Recent progress in hybrid glass materials for micro-optical component fabrication, Micro- and Nano-optics for Optical Interconnection and Information Processing. San Diego, US, 29 - 31 Jul 2001. Taghizadeh, M., Thienpont, H. & Jabbour, G. (eds.). SPIE. Bellingham,Washington,US. Vol. 4455 (2001), 15 - 22. (Invited)

23. Kärkkäinen, Ari, Rantala, Juha, Jabbour, Maurice, Liang, Chen, Bedford, Robert, Peyghambarian, Nasser, Descour, Michael, Jabbour, Ghassan, Miniaturezed organic light emitting diode (OLED) light source for micro-optical systems, SPIE Proceedings, San Jose 20-26 Jan., 2001, pp. 100 - 107.

24. Kärkkäinen, Ari, Rantala, Juha, Descour, Michael, Photolithographic processing of hybrid glasses for micro-optics applications, Optical MEMS, IEEE/LEOS, Okinawa, Japan, 25-28 Sept., 2001, pp.

25. Malinen, Jouko; Tenhunen, Jussi; Blomberg, Martti; Saari, Heikki, New instruments for NIR and IR wavelengths based on micromachined Fabry-Perot interferometer, http://www-umea.slu.se/kontakt/nirnord/seminarier/3rdnir.htm, 3rd NIR Nord Process-NIR Conference: NIR in Food, Feed and Food Packaging. Umeå, SE, 17 - 19 Sept. 2001. NIR Nord. Umeå (2001).

26. Marbach, Ralf, On wiener filtering and the physics behind statistical modeling, http://www-umea.slu.se/kontakt/nirnord/seminarier/3rdnir.htm#abs, 3rd NIR Nord Process-NIR Conference. NIR in Food, Feed and Food Packaging. Umeå, SE, 17 - 19 Sept. 2001 (2001).

27. Miettinen, Jari; Ailisto, Heikki, The effect of different thresholding methods in RGB Imaging, Proceedings of the SPIE, Intelligent Robots and Computer Vision XX: Algorithms, Techniques, and Active Vision. Casasent, David & Hall, Ernest (eds.). SPIE. Vol. 4572 (2001), 459 - 465.

28. Mäkelä, Jakke; Aikio, Janne; Venkatesh, Vadde; Kolehmainen, Timo; Karioja, Pentti, Optical information storage in cellular mobile terminals, Proc. SPIE 4534. Denver, US, 22 - 24 Aug. 2001. SPIE (2001), 174 - 183.

29. Mäkelä, Jakke; Juhola, Mikko; Aikio, Janne; Karioja, Pentti, Technical considerations for optical disks in cellular mobile terminals, Optical Data Storage Topical Meeting 2001 Technical Digest. 22 - 25 April Santa Fe, US, 2001 (2001), 13 - 15.

30. Perander, Anna-Maija; Halttunen, Mari; Jääskeläinen, Annastiina; Vyörykkä, Jouko; Vuorinen, Tapani, Determination of residual lignin from pulp samples with UV resonance raman spectroscopy, 11th International Symposium on Wood and Pulping Chemistry. Nice, FR, 11 - 14 Jun 2001 (2001), 331 - 334.

31. Rantala, Juha; Kärkkäinen, Ari; Hiltunen, Jussi; Kololuoma, Terho; Descour, Michael, New method to fabricate 3D optical structures into glass ceramic films, SPIE Photonics West. San Jose, US, 20 - 26 Jan. 2001. SPIE. US (2001), 74 - 79.

32. Rautioaho, Risto; Nousiainen, Olli; Leppävuori, Seppo; Dewei, Tian; Lenkkeri, Jaakko, Acoustic microimaging of fatigue cracking in solder joints of LTCC modules, Proc. of 13th European Microelectronics and Packaging Conference. Strasbourg, FR, 30 May - 1 June 2001 (2001), 172 - 177.

33. Vyörykkä, Jouko; Halttunen, Mari; Iitti, H.; Kenttä, Eija; Paaso, Janne; Tenhunen, Jussi; Vuorinen, T.; Stenius, Per, Confocal-raman analysis method to study binder depth profiles in coating layers Tappi Coating and Graphics Arts Conference and Trade Fair. Hyatt Regency, San Diego, CA, 6 - 9 Marc 2001. Tappi (2001), 193 - 201.

34. Vyörykkä, Jouko; Halttunen, Mari; Iitti, Hanna; Tenhunen, Jussi; Vuorinen, Tapani; Stenius, Per, Enhancement of depth resolution in confocal Raman microscopy using immersion optics ESOPS 14. 14th European Symposium on Polymer Spectroscopy. Dresden, DE, 2 - 5 Sept. 2001 (2001).

Other publications

1. Aikio, Janne; Howe, Dennis G., Direct semiconductor laser readout, Proc. Finnish Optics Days 2001. Tampere, FI, 20 - 21 Apr 2001. Tampere (2001), 45.

2. Aikio, Janne; Kataja, Kari; Tukkiniemi, Kari; Karppinen, Mikko; Mäkinen, Jukka-Tapani; Putila, Veli-Pekka; Keränen, Kimmo; Ojala, Kai; Karioja, Pentti; Kolehmainen, Timo, IPSE - image processing simulation environment, Proc. Finnish Optics Days. Tampere, FI, 20 - 21 Apr 2001. Tampere (2001), 41.

3. Ailisto, Heikki; Lindholm, Mikko, Sormenjälki hallitsee tunnistusta, Prosessori (2001) No: 6-7, 40 - 44.

4. Heikkinen, Veli; Keränen, Kimmo; Putila, Veli-Pekka; Tukkiniemi, Kari, Design of an active CMOS camera, Proceedings of Optics Days. Tampere, FI, 20 - 21 April 2001. Tampere (2001), P39.

5. Heikkinen, Veli; Keränen, Kimmo; Putila, Veli-Pekka; Tukkiniemi, Kari, Design system for optoelectronic modules, Proceedings of Optics Days. Tampere, FI, 20 - 21 April 2001. Tampere (2001), P40.

6. Hiltunen, Jussi; Tuomikoski, Markus; Rantala, Juha, Steady state and transient characteristics of organic light emitting devices (OLEDs), Optic Days 2001.Finnish Optical Society Conference. Tampere, FI, 20 - 21 Apr., 2001 (2001), P20. (Best poster award)

7. Juuso, Sanna; Liang, Chen; Mäkinen, Jukka-Tapani; Rantala, Juha; Descour, Michael, Non-sequential ray tracing as a simulation tool in modeling of micro-optical systems, Proceedings of Finnish Optics Days. Tampere, FI, 20 - 21 April 2001. Finnish Optical Society, Tampere University of Technology (2001), P37.

8. Kautio, Kari, Photoimageable fine line thick film conductors on LTCC, Elektroniikan tuotanto- ja pakkaustekniikan 2. Konferenssi. Pori, 17 - 18.5.2001. Pori (2001), 1 s.

9. Kemppainen, Antti, Infrapunatekniikka kosteusmittauksissa, AEL INSKO seminaarit. Prosessimittaukset 4: Kosteudenmittaus. I5368/01. Riihimäki, FI, 30 - 31.1.2001. INSKO. FI (2001), 9 p.

10. Kemppainen, Antti; Känsäkoski, Markku; Malinen, Jouko, Monitoring moisture and fat content of food products by short-wave near infrared spectroscopy, Optics Days. Tampere, FI, 20 - 21 April 2001. Tampere (2001), P27.

11. Kololuoma, Terho; Oksanen, J.; Raerinne, P.; Rantala, Juha, Dye-doped sol-gel coatings for near-infrared laser protection, Optic Days 2001, Finnish Optical Society Conference. Tampere, FI, 20 - 21, 2001. Finnish Optical Society. Tampere (2001).

12. Känsäkoski, Markku; Niemelä, Pentti; Crookell, A., Remote measurement of vehicle emissions at low cost (REVEAL, Optics Days. Tampere, FI, 20 - 21 Apr 2001. Tampere (2001), O6.

13. Lenkkeri, Jaakko, Elektroniikan pakkaus- ja liitosteknologioiden kehitystrendit. Elektroniikan perusteknologiat ja sotilaselektroniikan erityisvaatimukset. MATINE Elektroniikkajaosto. Espoo, FI, 5.6.2001. MATINE. Espoo (2001).

14. Marbach, Ralf, Multivariate calibration used in biomedical applications, http://www.infotech.oulu.fi/GraduateSchool/ICourses/Op_dev_instr.html, Infotech Oulu Workshop 2001. Optoelectronic Devices and Instrumentation. Oulu, FI, 28 - 31 May 2001. Oulu (2001).

15. Marbach, Ralf, Status of commercial noninvasive optical measurements, http://www.infotech.oulu.fi/GraduateSchool/ICourses/Op_dev_instr.html, Infotech Oulu Workshop 2001. Optoelectronic Devices and Instrumentation. Oulu, FI, 28 - 31 May 2001. Oulu (2001).

16. Rantala, Juha, Kärkkäinen, Ari, Light induced defprmations in hybrid glasses: characteristics and applications, Optic Days 2001, Finnish Optical Society Conference. Tampere, FI, 20 - 21, 2001. Finnish Optical Society. Tampere (2001). (Invited)

Patents

1. Karioja, Pentti; Sidorin, Yakov, Wavelength-tunable laser configuration. Pat. US 6,192,059 B1, publication date 20 Feb. 2001 (application number 09/293,054, application date 16 April 1999) (2001), 9 p.

Examination theses

1. Hiltunen, Jussi, Organic light emitting devices as pulsed light sources, Diploma Thesis, University of Oulu, Department of Electrical Engineering, 2001, 66p.

2. Tuomikoski, Markus, Performance and stability of organic light emitting devices, Master Thesis, University of Oulu, Department of Chemistry, 2001, 76 p.

CONTACT INFORMATION

VTT Electronics
P.O.Box 1100, (Kaitoväylä 1), FIN-90571 OULU, FINLAND
Tel. +358 8 551 2111, fax +358 8 551 2320
e-mail: ele.info@vtt.fi
www.vtt.fi/ele